2014-12-01

Evaluation of Current Empirical Methods for Predicting Lateral Spread-Induced Ground Deformations for Large Magnitude Earthquakes Using Maule Chile 2010 Case Histories

Ginger Emily Tryon
Brigham Young University - Provo

Evaluation of Current Empirical Methods for Predicting Lateral Spread-Induced Ground Deformations for Large Magnitude Earthquakes Using Maule Chile 2010 Case Histories

Ginger Emily Tryon

A thesis submitted to the faculty of
Brigham Young University
in partial fulfillment of the requirements for the degree of

Master of Science

Kyle M. Rollins, Chair
Kevin W. Franke
Norman L. Jones

Department of Civil and Environmental Engineering

Brigham Young University

December 2014

ABSTRACT

Evaluation of Current Empirical Methods for Predicting Lateral Spread-Induced Ground Deformations for Large Magnitude Earthquakes Using Maule Chile 2010 Case Histories

Ginger Emily Tryon
Department of Civil and Environmental Engineering, BYU
Master of Science

Improving seismic hazard analysis is an important part of building safer structures and protecting lives. Since large magnitude earthquakes are rarer than other earthquakes, it is harder to model seismic hazards such as lateral spread displacements for these events. Engineers are often required to extrapolate current lateral spreading models when designing utilities, bridges, and piers to withstand the ground displacements caused by earthquakes with magnitudes larger than 8.0. This study uses three case histories from the Maule Chile 2010 earthquake (M_w =8.8) to develop recommendations on which models are most accurate for large earthquake events and how to improve the accuracy of the models.

Six empirical models commonly used in engineering practice are compared. The model that best matches the Maule Chile case histories uses local attenuation relationships to make it easier to apply the model to any seismic region. Models that use lab data from cyclic shear tests over predict displacements but using a strain-reduction factor with depth significantly improved the accuracy of the results. Site-to-source distances can vary greatly between geographic seismic and faulting mechanisms. For this reason, models that depend on an internal source-to-site distance show less promise with large subduction zone earthquakes throughout the world. Models with site-to-source distances are most accurate in the western United States and Japan because the case histories for these models came from those countries.

Keywords: lateral spread, liquefaction, Chile, Maule earthquake

ACKNOWLEDGEMENTS

Funding for this study was provided by the National Science Foundation, Division of Civil, Mechanical, and manufacturing Innovation (CMMI) under Grant No. CMMI-1235526. This support is gratefully acknowledged. Nevertheless, the opinions, conclusions, and recommendations expressed in this study are those of the authors and do not necessarily reflect the views of NSF.

Many generous people in Chile made this work possible. We are very grateful to the Port of Coronel and Claudio Vega for allowing us to perform several soil tests in the port and being willing to work around us during the tests. Thank you Anne Lemnitzer and Ricardo Moffat owners of Lemnitzer and Moffat Geotechnica Ltd. for providing CPT services below the market rate for this study. I would also like to thank the many professors at the University of Chile that worked with us on this project.

I would like to thank my advisor and committee for their continued support and feedback. Dr. Kyle M. Rollins, your feedback and encouragement improved the presentation of the case histories and helped me better share our lessons learned. Dr. Kevin W. Franke, your knowledge of lateral spreading from your research and work experience helped me understand the models and how they worked.

I would like to thank the many researchers who have developed lateral spreading models. Dr. T. Leslie Youd, you provided valuable insight into the Alaska 1964 case histories. Dr. Peter Robertson, thank you for providing me with a free copy of the CPT analysis program Cliq (Geologismiki, Gregg Drilling, Robertson 2006) to use in my research.

Nicole Williams, thank you for your help with translation and research.

TABLE OF CONTENTS

LIST OF TABLES

LIST OF FIGURES

1 INTRODUCTION

Lateral spreading is the liquefaction and gravity driven deformation of soil that occurs in alluvial plains on gentle slopes or near free faces such as river embankments. Research continues on lateral spreading because its unique characteristics make it difficult to predict, its presence during earthquakes significantly impacts public safety and local economies, and current prediction models do not accurately represent all cases of lateral spreading. Lateral spreading is not as well understood and documented for large subduction zone earthquakes where wide-spread damage is common. Increased understanding of lateral spreading has the potential to increase safety and decrease economic loss in seismic regions.

Lateral spreading is a type of liquefaction-induced soil deformation with unique characteristics. Multiple factors affect the lateral spread displacements so two sites with similar topography and liquefiable soils may experience completely different displacements. The magnitude of lateral spread displacements changes with the strength, thickness, and continuity of the liquefied soil layers. Unlike other types of slope failure, the surface soil does not lose strength during lateral spreading. Instead, the soil moves as mostly intact blocks across the surface of the liquefied soil layer (see Figure 1-1). The liquefied soil does not completely fail, but is weakened sufficiently for the soil to move under the driving force of earthquake loading. Earthquake loading is so vital for ground movement that displacements will vary greatly based

on the duration and number of cycles. Lateral spreading is common on gentle slopes (less than 6%) where ground deformations are less likely to be anticipated. Since lateral spreading can occur in unintuitive areas and susceptible sites may initially appear similar to unsusceptible sites, engineers rely heavily on research in practice. Continued research is vital to engineers' ability to predict and design for all types of lateral spreading.

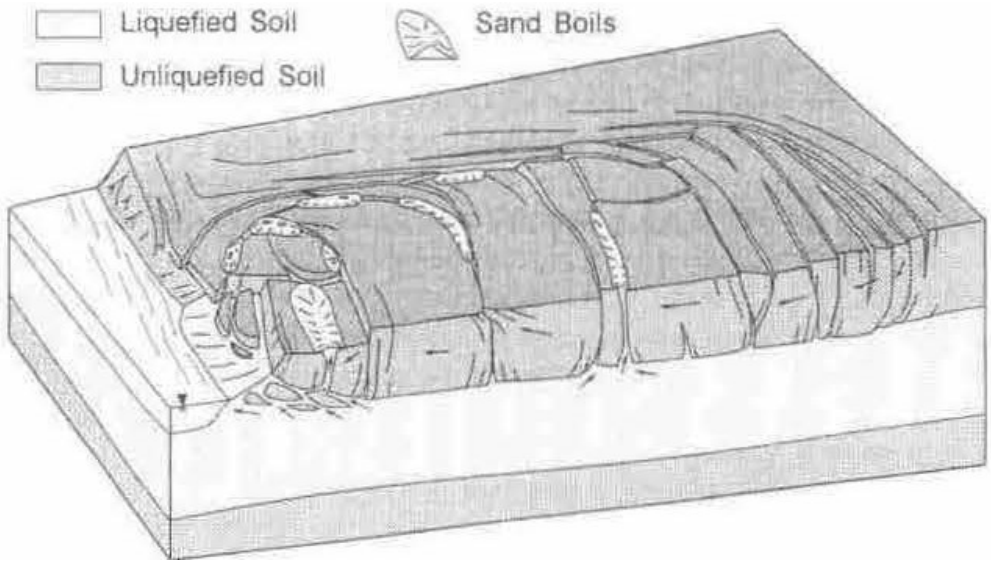

Figure 1-1: Depiction of Lateral Spreading from Rauch and Martin II 2000

Lateral spreads damage a wide variety of structures, making it an important economic and safety concern for seismic regions throughout the world. During the Maule Chile 2010 earthquake, several piers in the Concepción and Talcahuano region were damaged by lateral spreading and liquefaction. The estimated repair cost for these piers is 285 million dollars (Brunet, et al. 2012). In addition to direct repair costs, damaged piers negatively impacted Chile's fishing and shipping industries. Economics are not the only concern; damaged waterlines, lifelines, bridges, roads, and piers are major hazards because they prevent supplies and assistance from reaching people in need following an earthquake. During the 1906 San Francisco earthquake, several people died because lateral spreading damaged waterlines near

downtown San Francisco, slowing firefighting efforts (Bartlett and Youd 1995). Figure 1-2 shows a road that was badly damaged by lateral spreading during the 1959 M7.3 Hebgen Lake earthquake. These concerns have led researchers to investigate the mechanics and prediction of lateral spreading.

Figure 1-2: Road Damaged by Lateral Spreading, Photo by R. B. Colton (Idaho Geological Survey n.d.)

Past research led to the development of several models to predict lateral spread displacements. Empirical models are commonly used for predicting lateral spreading in engineering practice because they are easy to use and require less costly soil investigation. These models use case histories to correlate site characteristics and displacements using multi-linear regression. Since empirical methods use case histories, they are dependent upon and limited by past experiences. This has led empirical models to come with recommended input ranges to warn users against extrapolation that may invalidate the model. A variable commonly extrapolated in

lateral spreading models is earthquake magnitude. Earthquakes with $M_w > 8.0$, classified in this paper as large magnitude earthquakes, are less common than $M_w = 6.0$-8.0 earthquakes. Current empirical models for lateral spreading were created using case histories from only one large magnitude earthquake, the 1964 Alaska earthquake with a $M_w = 9.2$. Although some of these models permit the use of earthquake magnitudes up to 9.2, verification of their validity at large magnitudes is needed because of the lack of data in the 8.0-9.2 magnitude range. Further research on lateral spreading during large earthquakes has the potential to save lives, particularly in regions like Chile, Japan, and Indonesia where large magnitude earthquakes occur more frequently.

This research uses case histories from the Maule Chile 2010 earthquake to examine the integrity of empirical lateral spreading models when used for large magnitude earthquakes. Lateral spreading case histories from two piers in Coronel, Chile are used to measure the accuracy of six different empirical models commonly used in practice. Comparisons between the measured and predicted displacements will be used to answer several questions: Can these models be extrapolated for $M_w > 8.0$? Does the error associated with these models increase? Is there a particular model that predicts displacements at large magnitudes better than others? Are there trends in the way the models predict? Can we suggest methods for improving the predictive capacity of future models? The goal of this research is to make it easier for engineers to predict and design for the lateral spread displacements caused by large magnitude earthquakes. It is hoped that this will reduce the economic and societal losses caused by lateral spreading in future earthquakes.

2 LITERATURE REVIEW LIQUEFACTION

Liquefaction is one of the most common ground failures caused by earthquakes. Loose cohesionless saturated sand layers are the most susceptible to liquefaction because sands rely on friction between particles for shear strength and stability. During an earthquake, cyclic stresses cause loose sand particles to rearrange into a denser configuration. However, when the loading of earthquake waves is faster than the drainage of the water in the soil, the trapped water starts to counteract this rearrangement. In this temporary undrained condition, the pore water pressures increase while the friction forces between soil particles decrease. When the pore water pressures approach the vertical effective stress acting on the soil the shear strength decreases to zero, the soil acts similar to a liquid, leading to the aptly named condition called liquefaction. After the earthquake, the water has time to drain from the soil and the soil regains its strength. Liquefaction is an integral and connected process to lateral spreading because this decrease in shear strength is required for the soil to be able to move on relatively flat slopes.

Compared to our knowledge of liquefaction, the techniques to predict liquefaction are fairly new. When the Seed and Idriss 1971 simplified procedure for predicting liquefaction was published, it quickly gained popularity. This procedure has been discussed and redeveloped over the last thirty years to match advances in our understanding of liquefaction. The 1996 NCEER and 1998 NCEER and NSF workshops on the evaluation of liquefaction resistance of soils

brought together twenty experts to reach a consensus on a procedure and recommendations for engineers to follow in practice. This conference was a great step forward in understanding and predicting the liquefaction susceptibility of soil. The three liquefaction procedures described in this chapter build on this body of knowledge to provide simple yet effective ways to evaluate liquefaction.

2.1 Youd, et al. 2001

This model was published shortly after the NCEER workshops and discusses the procedure for predicting liquefaction agreed upon and developed there. Built on the Seed and Idriss 1971 simplified procedure, cyclic shear stresses describe the demands of earthquake loading in both models. The Youd, et al. 2001 model uses the same equation as the simplified procedure to find the cyclic shear stress ratio, CSR, with minor changes to the calculation of r_d. CSR describes earthquake loading by finding the average stress per cycle, approximated as sixty-five percent of the stress corresponding to the largest cycle as shown in equation 1.

$$CSR := 0.65 \cdot \left(\frac{\sigma_{vo}}{\sigma'_{vo}} \right) \cdot \left(\frac{a_{max}}{g} \right) \cdot r_d \quad (1)$$

Where σ_{vo} = the total vertical stress, σ'_{vo} = the effective vertical stress, a_{max} = the maximum horizontal ground acceleration, and r_d = the stress reduction factor. The stress reduction factor varies greatly with depth, magnitude, and the stratigraphy of the soil. Seed and Idriss 1971 had a range of r_d values that could be used at different depths. For non-critical projects, the following equations calculate the average r_d values from the Seed and Idriss 1971 procedure at depth z.

$$r_d = 1.0 - 0.00765 \text{ for } z \leq 9.15m \quad (2)$$

$$r_d = 1.174 - 0.0267 \text{ for } 9.15m < z \leq 23m \quad (3)$$

Undisturbed samples are difficult to obtain for liquefiable soils so the soil strength is determined from field tests. Correlations from field measurements to the cyclic shear resistance of soil were developed for several field tests. One of the most common tests is the standard penetration test (SPT), which measures the strength of soil by the number of blows from a hammer required to penetrate a foot of soil. For consistency in measurements, the Youd et al 2001 model recommends that the blow counts be corrected for overburden pressure, hammer energy, borehole diameter, rod length, sampler lining, and fines content. These corrected blow counts are used to determine the ability of the soil to resist liquefaction, CRR, with equation 4.

$$CRR_{7.5} := \frac{1}{34 \cdot N1_{60}} + \frac{N1_{60}}{135} + \frac{50}{\left(10 \cdot N1_{60} + 45\right)^2} - \frac{1}{200} \tag{4}$$

Since the CRR curves are based on a magnitude 7.5 earthquake, a magnitude scaling factor is included to extend the use of this equation to other magnitudes. Several magnitude scaling factors have been proposed and consensus on the best one was not reached at the workshops, so multiple scaling factors were recommended for use when computing the factor of safety. In addition to the magnitude scaling factor, the factor of safety, FS, is also corrected for high overburden stresses and deposit age using K_σ and K_α as shown in equation 5.

$$FS := \left(\frac{CRR_{7.5}}{CSR}\right) \cdot MSF \cdot K_\sigma \cdot K_\alpha \tag{5}$$

This factor of safety is used to determine how likely a soil layer is to liquefy during a particular earthquake. In addition to the factor of safety, two rules of thumb are used to determine susceptibility to liquefaction: soils with SPT blow counts greater than thirty are too dense to liquefy and soils with plastic fines will not liquefy.

2.2 Idriss and Boulanger 2004

This approach also uses cyclic shear stress ratios to find the factor of safety against liquefaction. CSR is found using equation 1 with different recommendations for the stress reduction factor, r_d. For depths less than or equal to 34 meters, r_d is determined using the equations below.

$$\ln(r_d) = \alpha(z) + \beta(z) \cdot M \tag{6}$$

$$\alpha(z) := -1.012 - 1.126 \sin\left(\frac{z}{11.73} + 5.13\right) \tag{7}$$

$$\beta(z) := 0.106 + 0.118 \sin\left(\frac{z}{11.28} + 5.142\right) \tag{8}$$

These stress reduction factors are designed to be compatible with the magnitude scaling factor proposed by Idriss and Boulanger 2004 for CSR. Instead of adjusting CRR for magnitude, CSR is adjusted to account for the difference in number of stress cycles with different earthquake magnitudes. The cyclic shear stress ratio is normalized to the equivalent number of stress cycles for a $M_w = 7.5$ earthquake using equations 9 and 10.

$$CSR_{M7.5} := \frac{CSR}{MSF} \tag{9}$$

$$MSF := 6.9e^{\left(\frac{-M}{4}\right)} - 0.058 \tag{10}$$

Idriss and Boulanger 2004 proposed slightly different values for the cyclic resistance ratio, CRR. Case histories were used to create a curve that shows the cutoff between liquefiable soils and non-liquefiable soils at different SPT corrected blow counts as shown Figure 2-1. This curve is used to determine CRR based on corrected SPT blow counts. The Idriss and Boulanger 2004 method requires corrections for overburden pressure, hammer energy, and fines content to

obtain an $N1_{60cs}$ value. The blow counts are not corrected for rod length, borehole diameter, and sampler type as recommended during the NCEER workshop. The equation for the curve purposed by Idriss and Boulanger 2004, shown in Figure 2-1, is:

$$CRR := e^{\left[N1_{60cs} + \left(\frac{N1_{60cs}}{126}\right)^2 - \left(\frac{N1_{60cs}}{23.6}\right)^3 + \left(\frac{N1_{60cs}}{25.4}\right)^4 - 2.8\right]} \tag{11}$$

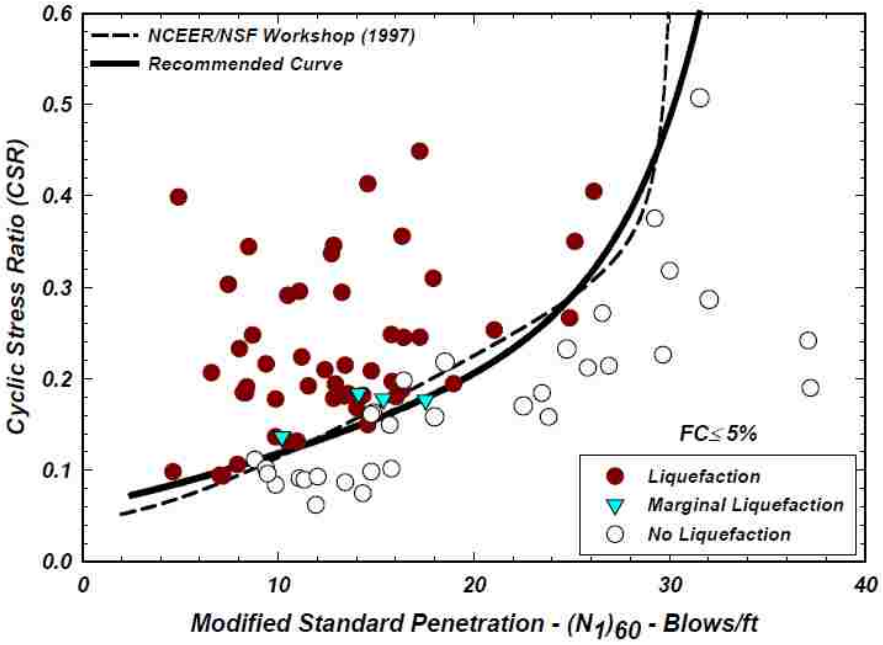

Figure 2-1: Recommended Curve for M=7.5 (Idriss and Boulanger 2004)

Even though the SPT blow counts are corrected for fines, the fines content and plasticity of the fines in the cohesionless sands still affect the liquefaction resistance of the soil. Liquefaction and lateral spreading have not been observed in layers containing plastic fines. Other soil failure modes such as cyclic mobility are observed in cohesive soils and are determined using other methods. In addition to the recommendations of the Chinese Criteria, Idriss and Boulanger 2004 developed their own rule of thumb for determining liquefaction susceptibility of fine-grained soil. These equations are considered valid for fine-grained soils or soils containing a large

portion of fines when the plasticity index is less than or equal to five, the water content is greater than eighty percent of the liquid limit, and the liquid limit is less than thirty-seven. Soils with a plasticity index greater than five are considered unsusceptible to liquefaction because of the way the fines increase the liquefaction resistance of the soil. It is important to be aware of fines and their effects on soil liquefaction when analyzing liquefaction and lateral spreading potential.

2.3 Cetin, et al. 2004

Cetin, et al. 2004 provided recommendations for changes to the liquefaction procedure from the 1996 and 1998 NCEER workshops based on new research. Recommendations include changes to the equations for the stress reduction factor, r_d, and the allowable plasticity index for fines. Additional case histories of liquefaction were also added to the model to take advantage of lessons learned from recent events. All the case histories were graded based on the quality of available data to account for uncertainty more directly in the statistical analysis of the model. The overall procedure is still similar to the one used by Youd, et al. 2001 and Idriss and Boulanger 2004.

The stress reduction factor accounts for the difference between the way the soil behaves and how a rigid block would behave. Previous methods to develop r_d had used fairly uniform stratigraphies which were considered unrepresentative of the complex layering of various soils found in the field. The stratigraphies used to develop r_d for the Cetin, et al. 2004 method came from fifty liquefaction case histories to capture the site variability found in the field. A total of 2,153 site response analyses were performed to develop the stress reduction factor given by

$$r_d = \frac{\left[1 + \frac{-23.013 - 2.949a_{max} + 0.999M_w + 0.0525V^*_{s,12m}}{16.258 + 0.201e^{0.341\left(-20+0.0785V^*_{s,12m}+7.586\right)}}\right]}{\left[1 + \frac{-23.013 - 2.949a_{max} + 0.999M_w + 0.0525V^*_{s,12m}}{16.258 + 0.201e^{0.341\left(0.0785V^*_{s,12m}+7.586\right)}}\right]} - 0.0046(d - 20) \pm \sigma_{\varepsilon rd}. \quad (12)$$

This is the stress reduction factor equation Cetin, et al. 2004 recommends using in equation 1 when calculating CSR. CSR is then corrected by the magnitude and overburden pressure to obtain CSR^*_{eq}. When determining the liquefaction resistance of the soil, CRR, Cetin, et al 2004 used the same corrections to SPT blow count that are recommended by Youd, et al. 2001. However, the Cetin, et al. 2004 equation for determining the rod length correction is slightly different from the Youd, et al. 2001. These corrected SPT values are used to obtain CRR using Figure 2-2. Figure 2-2a is used in the Cetin, et al. 2004 probabilistic approach and includes a probability of liquefaction with the CRR value. Figure 2-2b is used for a deterministic approach and is used to find a factor of safety against liquefaction. New case histories were added to the model to develop the curves shown in Figure 2-2. These new case histories included liquefied sites containing fines with a higher plasticity index than observed in previous case histories. This led Cetin, et al. 2004 to recommend increasing the allowable plasticity index to 12 while keeping the water content and liquid limit recommendations of Idriss and Boulanger 2004.

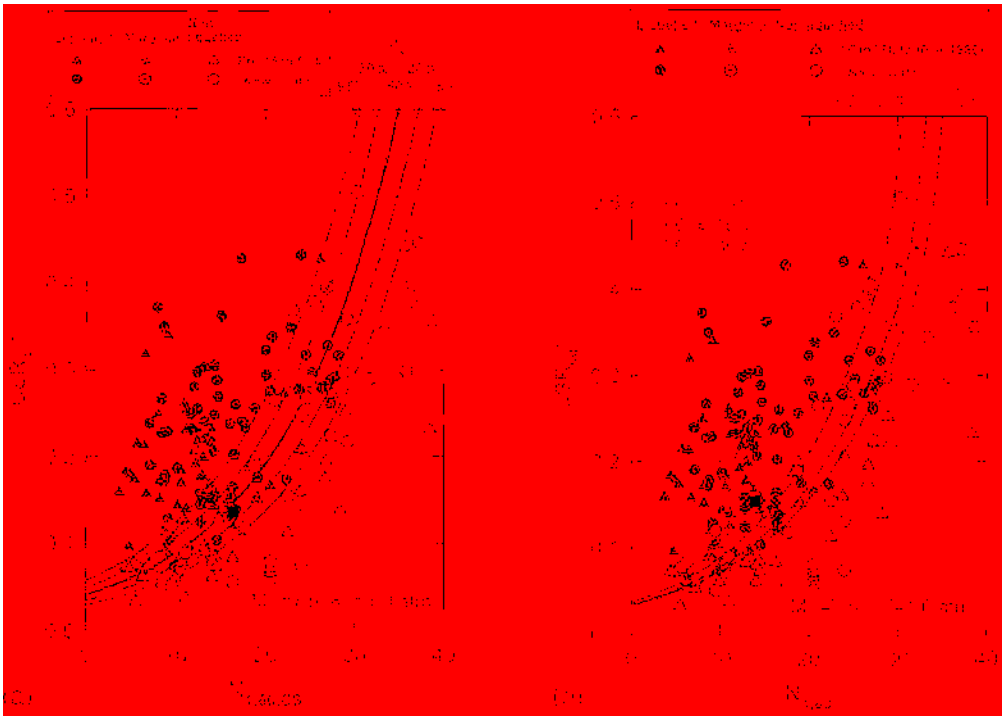

Figure 2-2: Curves for the Probabilistic (a) and Deterministic (b) Approach

2.4 Conclusions

Current procedures for evaluating liquefaction are similar with small differences based on author preferences. Different equations for finding the stress reduction factor, r_d, are used and recommended by different authors. The procedures for correcting SPT blow counts also vary with authors, with different recommendations for the corrections to include and slightly different corrections for fines content. While the cut-offs for plasticity of fines vary between authors, there is consensus that cohesive soils do not liquefy and that layers containing silts and clays will generally not liquefy unless the fines have a low plasticity index. These three methods were used for all the lateral spreading sites to gain a consensus on what layers were liquefiable, which layers to include in the T_{15} layer, and which soil layers would be susceptible to cyclic mobility instead of liquefaction.

3 LITERATURE REVIEW LATERAL SPREAD

Several empirical methods predict the distance that soil will move due to the mechanisms of lateral spreading. Multi-linear regressions are used on a collection of lateral spread case histories to create equations that correlate input variables to measured displacements. Empirical models use a variety of variables such as moment magnitude, M_w; source-to-site distance, R or R_{rup}; fines content, F; slope, S; and the thickness of liquefiable soil layers with SPT blow counts less than 15, T_{15}. These variables correlate seismic sources and soil conditions with the amount of soil deformation that is likely to occur. Some of the empirical methods commonly used in practice are Bardet, et al. 2002, Faris, et al. 2006, Rauch and Martin II 2000, Youd, Hansen and Bartlett 2002, Zhang, Robertson and Brachman 2004 and Zhang, et al. 2012.

3.1 Youd and Bartlett 1995 and Youd, Hansen and Bartlett 2002

One of the most well-known and widely used empirical equations for predicting lateral spread was originally published in Youd and Bartlett 1995 and updated in Youd, Hansen and Bartlett 2002. The original database included case histories from eight earthquakes and fifteen different sites for a total of 467 measured horizontal displacement vectors from lateral spreads in Japan and the western United States. This database was the basis for their empirical model and has been updated over the past decade to include two more earthquakes and additional sites from the Borah Peak, Idaho earthquake. They made the database public allowing other researchers to

build on their work to create new empirical models. Several widely used empirical equations were developed using data from the case histories collected by Youd, Hansen and Bartlett.

3.1.1 Bartlett and Youd 1995

Bartlett and Youd presented their first empirical equation for predicting lateral spread displacements in 1995. They collected data from several earthquakes between the years of 1906 and 1987 to represent lateral spreading that had occurred in Japan and the western United States during the twentieth century. Bartlett and Youd 1995 chose different independent variables for their model that described the seismic, topographic, or geotechnical conditions known to be connected with the phenomena of lateral spreading. These variables were added in one at a time until no significant reduction in error was shown through the addition of a new variable.

As the equation was created, a major difference was discovered between displacements vectors near a free-face such as a riverbank and ones located solely on gentle sloping ground. This led to the equation being split into two equations with one for free face conditions and the other for ground slope conditions. Figure 3-1 shows an example of a free-face and a gently-sloping case. For free-face cases, the height of the free-face from crest to toe, H, is divided by the length or distance from the start of displacement to the toe of the free-face, L, to create the free-face ratio, W(%) used in the equations. The gently sloping case is simply represented by the slope of ground where the soil displaced.

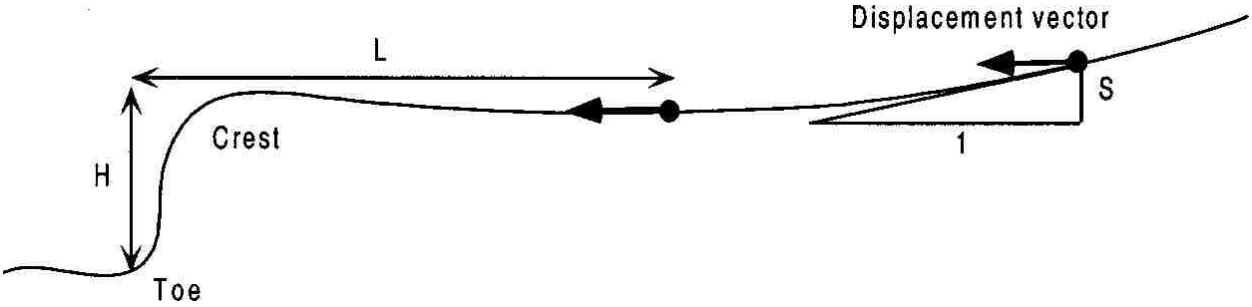

Figure 3-1: Geometry of Free-Faces and Gentle Slopes (Bardet, et al. 2002)

Free-face case:

$$\log(D_H + 0.01) = 16.366 + 1.178M + 0.927\log(R) + 0.013R$$
$$+0.657\log(\mathrm{W}) + 0.348\log(T_{15}) + 4.527\log(100 - F_{15}) + 0.922D50_{15} \quad (13)$$

Gently sloping case:

$$\log(D_H + 0.01) = 15.787 + 1.178M + 0.927\log(R) + 0.013R$$
$$+0.429\log(\mathrm{S}) + 0.348\log(T_{15}) + 4.527\log(100 - F_{15}) + 0.922D50_{15} \quad (14)$$

The variables in the equations are M = moment magnitude, R = horizontal distance to nearest fault rupture (km), W = the free face ratio (%), S = ground slope (%), T_{15} = thickness of liquefied layer with $N1_{60}$< =15 within the top 20 meters (m), F_{15} = fines content of the liquefied layer with $N1_{60}$< =15, and $D50_{15}$ = the mean-grain size for the same layer as described above for T_{15} and F_{15}.

3.1.2 Youd, Hansen and Bartlett 2002 Updates

In 2002, Youd, Hansen and Bartlett published an updated version of the 1995 equation with five changes to the original. Three of these updates include:

1. Corrections to the overestimated ground displacements for the 1983 Nihonkai-Chubu Japan earthquake

2. Elimination of any displacement vectors where movement could have been inhibited by boundary conditions or other obstructions
3. Addition of case histories from the 1983 Bora Peak, Idaho; 1989 Loma Prieta, California; and 1995 Kobe, Japan earthquakes

These changes improved the quality of the database. The addition of new case histories allowed the equation to be expanded from sand and fine grained soils to gravelly sites that were now better represented in the new case histories. The addition of gravelly sites from the Bora Peak Idaho earthquake caused the equation to become more sensitive to the mean-grain size. To correct this sensitivity the term $D50_{15}$ was replaced with log ($D50_{15}$+0.01).

The last change was to eliminate the minimum source distance required in the 1995 version of the equation. Changes were made to the log(R) term to account for near source effects. In the new equation log(R) is replaced with log(R*), where R* is:

$$R^* = R + R_o, \text{ and} \tag{15}$$

$$R_o = 10^{(0.89M-5.64)} \tag{16}$$

With these changes the lateral spread equations for free-face and gentle slope conditions are now

$$\begin{aligned} \log(D_H) = {} & -16.71 + 1.532M - 1.406\log(R^*) - 0.012R \\ & + 0.592\log(W) + 0.54\log(T_{15}) + 3.413\log(100 - F_{15}) \\ & - 0.795\log(D50_{15} + 0.01) \end{aligned} \tag{17}$$

and

$$\begin{aligned} \log(D_H) = {} & -16.21 + 1.532M - 1.406\log(R^*) - 0.012R + \\ & 0.592\log(S) + 0.54\log(T_{15}) + 3.413\log(100 - F_{15}) - \\ & 0.795\log(D50_{15} + 0.01). \end{aligned} \tag{18}$$

3.2 Bardet, et al. 2002

After considering several options for variable combinations, a subset of Bartlett and Youd 1995 equation was chosen for the Bardet, et al. 2002 model. Bardet, et al. 2002 simplified the equation down to five variables M, R, W, S, and T_{15}. In Bardet's equation R is the epicentral distance instead of the fault rupture or seismic energy distance used in the Bartlett and Youd 1995 equation. The simplified model was proposed to make the equation more user-friendly and allow it to be used where F_{15} and $D50_{15}$ are unknown. Utility companies that are interested in ground deformations over a large area receive the most benefit from this change, allowing them to protect pipelines with less soil investigation. However, this change decreased the overall accuracy of the model. The R^2 term dropped from 0.826 for the Bartlett and Youd 1995 equation to 0.643 for the Bardet, et al. 2002 equation.

Another change made by Bardet, et al. 2002 was to split the case histories into two datasets named A and B. All of the case history displacements were included in dataset A and only displacements less than 2 meters were included in dataset B. This change was made to improve the prediction of displacements less than two meters. The equation for Case A with free-face conditions is:

$$\log(D + 0.01) = 6.815 + 0.465 + 1.017M - 0.278\log(R) + 0.26R + 0.497\log(W) + 0.558\log(T15). \quad (19)$$

3.3 Faris, et al. 2006

The Faris, et al. 2006 model is a semi-empirical model for predicting lateral spread displacements. A semi-empirical model is developed using a combination of laboratory data and

case histories. By combining data from several sources the modeler attempts to merge past experiences with sound theory. The Faris, et al. 2006 model uses laboratory data from cyclic simple shear tests to model the effect of earthquake loads and soil strength on ground deformations. Cyclic loads from the simple shear tests can be correlated with the cyclic loading of an earthquake using cyclic shear stress ratio, CSR. In the field, Standard Penetration Tests (SPTs) are commonly used to determine the strength of soil so the soil strengths in the tests were correlated with N160cs corrected SPT values. The relationships in the Faris, et al. 2006 model are based on the work of Wu 2002 to correlate CSR and in-situ SPT blow counts to shear strain potential index. Shear strain potential index, which is called limiting shear strain by other authors, is "the maximum amplitude shear strain at the fifteenth uniform cycle, representing the "typical" representative number of equivalent uniform cycles common to earthquakes of moment magnitude 7.5 earthquakes" (Faris, Probabilistic Models for Engineering Assesment of Liquefaction-Induced Lateral Spreading Displacements 2004). The Wu 2002 model based on cyclic simple shear tests is shown in Figure 3-2. Notice that there are fewer points for corrected SPT blow counts less than 15 especially at higher cyclic stress ratio.

The Faris, et al. 2006 model uses the strain potential of each liquefiable soil layer to determine the potential of a soil to displace. Each combination of SPT blow count and CSR is associated with a different potential for the soil to deform. The strain potential index, SPI, is correlated with a displacement potential index, DPI, by multiply the SPI for each layer by the thickness of the layer. Soil layers that were found to be non-liquefiable using the Cetin, et al. 2004 method for liquefaction analysis are not included in the equation.

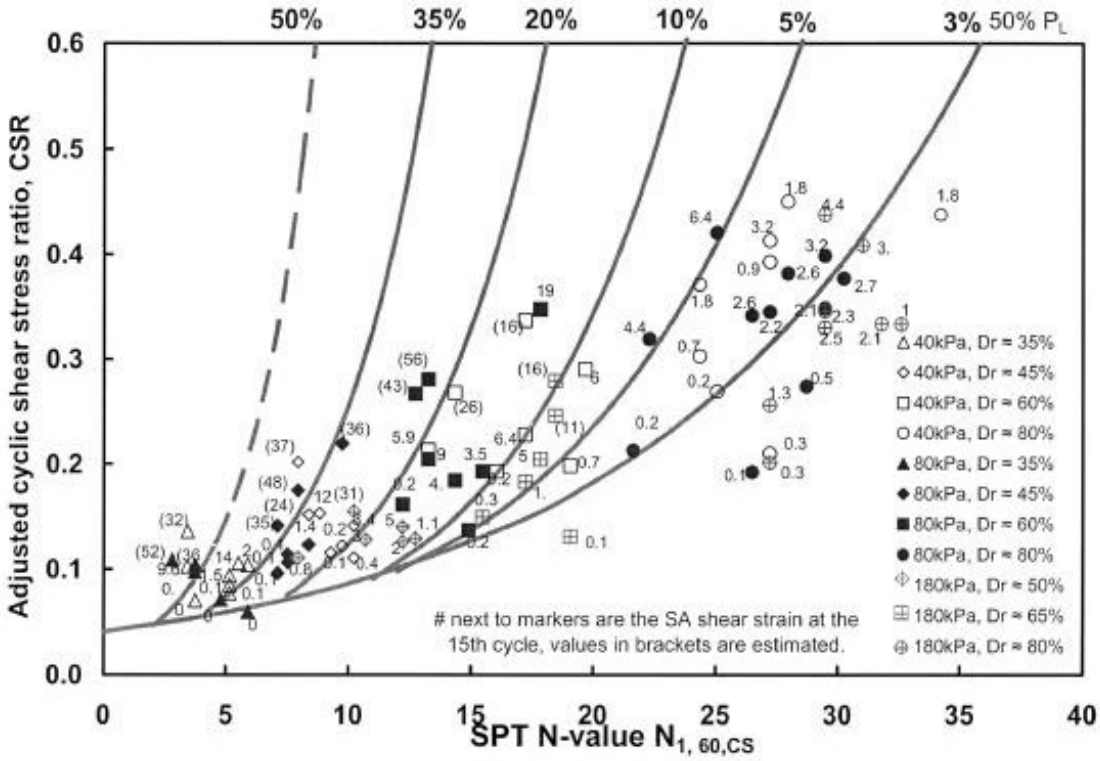

Figure 3-2: Strain Potential Curves from Wu 2002

Faris, et al. 2006 believed this would be an improvement over the T_{15} variable in other models, which gives the thickness of lateral spreading susceptible soil layer(s) the same weight in the model regardless of the actual values. While true that the displacements will vary with SPT blow count, adding this variability into the lateral spreading model requires extrapolation of current models for strain. As shown in the Wu 2002 model, as blow counts decrease there are less data points from cyclic simple shear tests because of the challenges of loading lose soils. Faris had to extrapolate an additional curve for 75% strain to calculate strain potential for soils with lower blow counts when developing her model as shown in Figure 3-3. In addition, the lack of test data for large CSR values, especially on loose soils, puts the Faris, et al. 2006 model at risk for erroneous results when used for large magnitude earthquakes. There is no cap on the

maximum shear strain potential index so it is possible to get a hundred percent strain, a value two times larger than those measured in laboratory tests. The Faris, et al. 2006 semi-empirical model was developed with laboratory but it is still at risk for erroneous extrapolation when used for large magnitude earthquakes. Strain potential indexes are assigned to layers with corrected blow counts above the cutoff of fifteen that Youd, Hansen and Bartlett 2002 recommends for use with lateral spreading. This allows the Faris, et al. 2006 model to predict displacements for liquefiable layers considered too dense to support liquefaction by other authors.

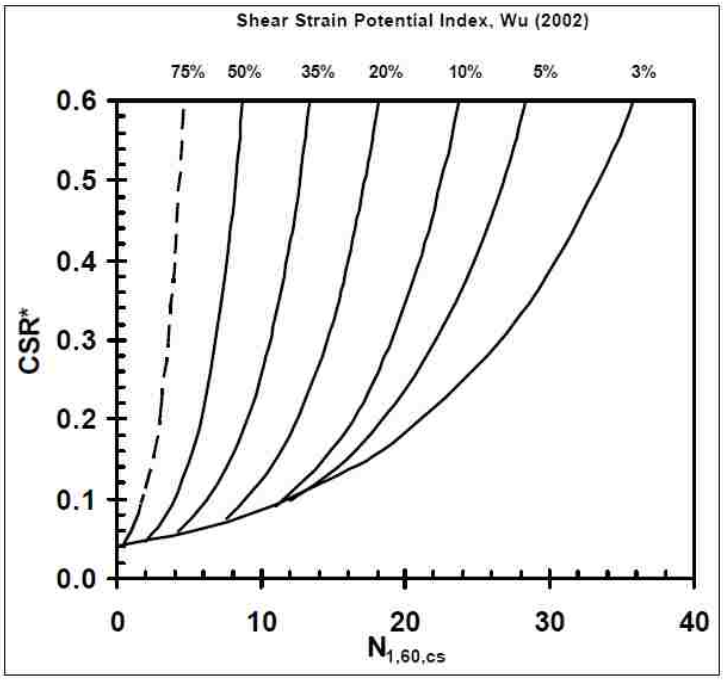

Figure 3-3: Wu 2002 Strain Curves with 75% Curve from Faris, et al. 2006

In addition to laboratory tests, statistical theory was used to improve the accuracy of the Faris, et al. 2006 semi-empirical model. Two assumptions of simple linear regression are that all observations are independent of each other and every point has the same standard deviation (Ramsey and Schafer 2002). Displacements close to each other are part of a lateral spread feature

and have some dependence on one another. To preserve independence, displacement vectors close together were grouped into lateral spread features instead of being treated separately. In the Faris, et al. 2006 maximum displacement model, the maximum displacement measured on each feature was used to develop the model while preserving independence. Displacements and site characteristics were known with varying accuracies for each case history leading to different standard deviations for each point. Instead of using a linear regression that would assume the same standard deviation for every point, the case histories were graded and weighted according to the data quality. An A grade was assigned to case histories that had six or more measured displacements from surveys or photos, accurate measurements of topography, six or more borings with lab data, and a strong motion recording at the site (Faris, Probabilistic Models for Engineering Assesment of Liquefaction-Induced Lateral Spreading Displacements 2004). Bayesian updating methods were used to correlate the values while taking into account uncertainty. Sites with more uncertainty had less weight so that the most accurate measurements would influence the regression line the most. These changes improved the regression to create a more statistically accurate model.

After developing a model using displacement potential index, DPI, other variables were chosen. The final model includes the static driving shear stress, α (%), and the moment magnitude, Mw, as given by equation 20:

$$H_{max} = e^{1.0443\, ln(DPImax)} + 0.0046\, ln(\alpha) + 0.0028 M_w. \quad (20)$$

The static driving shear stress is approximated using the slope of the ground surface, the height of the free face divided by one quarter of the length from the free face, or the sum of both values for sites with both a ground slope and a free face. Although the earthquake magnitude was used earlier in the Cetin, et al. 2004 liquefaction assessment, the Faris, et al. 2006 model includes

moment magnitude again to capture the effect of earthquake duration on displacements because the "magnitude-correlated duration adjustment of CSReq is based on a field case history data set for liquefaction initiation and not for lateral spreading" (Faris, et al. 2006). This model is one of the most popular semi-empirical models for lateral spreading.

3.4 Rauch and Martin II 2000

The Rauch and Martin II 2000 model is also called the Empirical Prediction Of Liquefaction-induced Lateral Spreading or EPOLLS. The model was split into three sections to be used depending on the amount of information available about the seismic region, topography, and soil properties at a particular site. The three sections of the model are called the Regional EPOLLS-which includes information about the seismic source, Site-EPOLLS which includes topography and seismic source information, and Geotechnical-EPOLLS which adds soil properties to the site model. Each section increases the accuracy of the prediction as additional information is introduced into the model. The Rauch and Martin II 2000 model recognizes that engineers sometimes need to make important decisions when little information is available but a model with more variables would provide greater accuracy. To reach the needs of different users these three sub-models were created so that people could use the model that best fit their needs. The empirical equation for the most accurate of the models with R^2 =0.752, the Geotechnical-EPOLLS model, is:

$$Avg_{Horz} = \begin{pmatrix} 0.613M_w - 0.0139R_f - 2.42A_{max} - 0.0114T_d \\ +0.000523L_{slide} + 0.0423S_{top} \\ +0.0313H_{face} + 0.0506Z_{FSmin} - 0.0861Z_{liq} - 2.49 \end{pmatrix}^2 + 0.124 \quad (21)$$

where, R_f is "shortest horizontal distance from site to surface projection of fault rupture or zone of seismic energy release," A_{max} is the peak ground acceleration, T_d is the "duration of strong

earthquake motions at site, defined as time between first and last occurrence of surface acceleration $\geq 0.05g$," L_{slide} is the maximum length of the slide, S_{top} is the slope of the ground for the slope case or the slope leading up to the free face for the free face case, H_{face} is the height of the free face, Z_{FSmin} is the depth to the soil layer with the smallest factor of safety against liquefaction, and Z_{liq} is the depth to the top of the liquefied soil layers (Rauch and Martin II 2000).

An interesting characteristic of the Rauch and Martin II 2000 model is that it finds the average horizontal displacement instead of the maximum observed horizontal displacement. Similarly to Faris, et al. 2006 model, lateral spread features were used as points instead of separate displacement vectors. When the model was created all of the displacements on a particular feature were averaged. Average displacements at each site were used to decrease the overall error in measurements that came from eye-witness accounts allowing more case histories to be used. This model includes a moderately larger database with case histories from fifteen different earthquakes because of the inclusion of case histories where the displacements were not as well documented.

3.5 Zhang, Robertson, and Brachman 2004

This model is the basis for the lateral spread displacements calculated by the software program Cliq (Geologismiki, Gregg Drilling, and Robertson). This method was developed to compute lateral displacements from both SPT and CPT tests. Similarly to Faris, et al. 2006 model, strains are used to correlate in-situ test values to lateral displacements. The strains curves for this method are based on the work of Ishihara and Yoshimine with a cap on the maximum shear strain to account for the dilative behavior of loose sands based on recommendations from

Seed. Ishihara and Yoshimine used cyclic shear tests on saturated sand to correlate the factor of safety against liquefaction and relative density with maximum shear strain as shown in Figure 3-1. Zhang, Robertson, and Brachman 2004 recommend using the Youd, et al. 2001 model to calculate the factor safety against liquefaction.

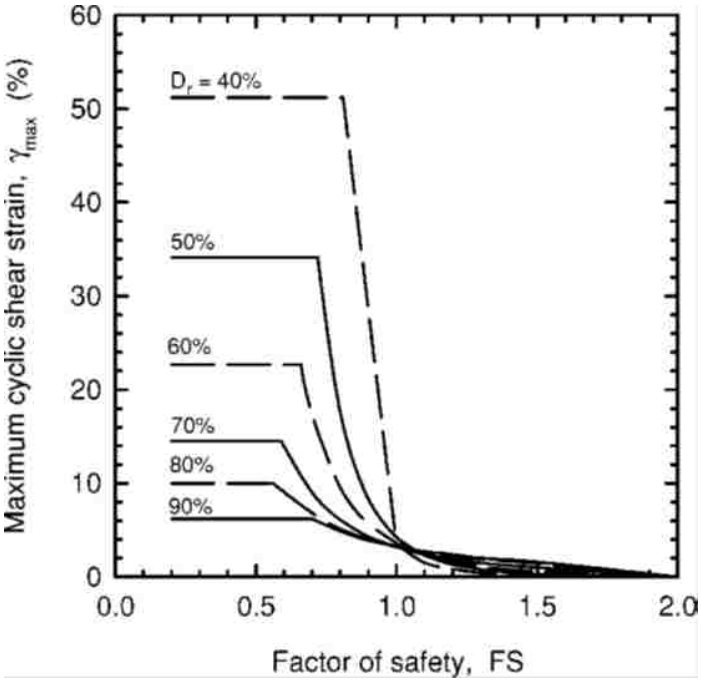

Figure 3-4: Maximum Shear Strains for Zhang, Robertson and Brachman 2004

CPT or SPT values are corrected to $(N1)_{60}$ or q_{C1N} according to the recommendations from the NCEER conference on liquefaction as published in Youd, et al. 2001. These values are then converted to relative density, Dr, using the following equations:

$$Dr = 14 * \sqrt{(N1)_{60}}, \text{ for } (N1)_{60} < 42 \quad (22)$$

$$Dr = -85 + 76\log(q_{C1N}), \text{ for } q_{C1N} \leq 200. \quad (23)$$

The relative density is used with a factor of safety to find maximum shear strain values, γ_{max}, as shown in Figure 3-4. The lateral displacement index, LDI, is calculated by

integrating maximum cyclic shear stress over the thickness of liquefiable layers to a depth of twenty-three meters as shown.

$$LDI = \int_0^{z_{max}} \gamma_{max} d_z \tag{24}$$

Instead of using a regression analysis, the relationship between LDI and lateral displacements was determined by the line that best fit the case histories graphically. Lateral displacements, LD, can be calculated for free-face and gentle slopes case using equations (25 and (26 respectively. The L and H used for the free-face case is the same as used in the previous models (see Figure 3-1). The Zhang, Robertson, and Brachman 2004 model does not include M_w, considering the liquefaction analysis adequate to describe the seismic factors that affect lateral spread displacements.

$$LD = 6\left({}^{L}/_{H}\right)^{-0.8} LDI, \text{ for } 4 < {}^{L}/_{H} < 40 \tag{25}$$

$$LD = (S + 0.2) * LDI, \text{ for } 0.2\% < S < 3.5\% \tag{26}$$

3.6 Zhang, et al. 2012

The main goal of the Zhang, et al. 2012 empirical model was to find a way to expand the reach of empirical models to countries other than the western United States and Japan. Moment magnitude and fault rupture distance are related to the local seismicity of an area. Fault rupture distances and moment magnitudes can vary widely with similar effects on soil deformations if the measurements come from different types of faults. Therefore, these parameters were replaced with a parameter which could conveniently be determined for different seismic regions, pseudo spectral displacement. The pseudo spectral displacement, SD, is calculated using a local strong-

motion attenuation to find the spectral acceleration at a period of 0.5 seconds and converting it to a pseudo spectral displacement by dividing by $(4\pi)^2$. The use of local attenuation relationships allows the model to be tailored to the seismic source parameters of every country without needing to develop a separate model for each country. The equations for the Zhang, et al. 2012 model are shown below.

Free-face case:

$$\log(D_H) = 1.8619\log(SD) + 0.608\log(W) + 0.0342T_{15} + 2.4643\log(100 - F_{15}) - 0.8382\log(D50_{15} + 0.1) - 3.4443 \quad (27)$$

Gentle slope case:

$$\log(D_H) = 1.8619\log(SD) + 0.4591\log(S) + 0.0197T_{15} + 2.4643\log(100 - F_{15}) - 0.8382\log(D50_{15} + 0.1) - 2.7096 \quad (28)$$

This equation uses the Youd, Hansen and Bartlett 2002 database of lateral spread case histories. However, the 1964 Alaska earthquake was not included because it is a magnitude 9.2 earthquake and unrepresentative of the magnitudes commonly found in the available case histories. After deriving the equation from the database, the equation was tested using lateral spread case histories from the 1999 Kocaeli, Turkey and the 1987 Edgecumbe, New Zealand earthquakes. Other models were also used as a comparison to see if the changes made by the Zhang, et al. 2012 model improved the accuracy of lateral spread predictions for countries outside the United States. The model predicted well the lateral spread displacements for these two earthquakes and this empirical model is recommended for use when working in countries outside of the United States and Japan.

3.7 Summary of Models

Earthquakes with moment magnitudes greater than 8.0 are underrepresented in current empirical models designed to predict lateral spreading displacements. The only case histories for an earthquake with magnitude greater than 8.0 came from the M=9.2 Alaska 1964 earthquake. As the models are tested to verify their integrity when extrapolated to larger magnitudes, differences between the models became more apparent as described in subsequent chapters. Each model has its individual strengths and weaknesses. Some weaknesses are common among several of the models.

Table 3-1: Earthquake Magnitudes in Lateral Spreading Case Histories

Earthquake	Mw	Bardet, et al. 2002	Faris, et al. 2006	Rauch and Martin II 2000	Youd, Hansen and Bartlett 2002	Zhang, Robertson, Brachman 2004	Zhang, et al. 2012
1971 San Fernando, CA	6.4	X	X	X	X	X	X
1979 Imperial Valley, CA	6.5	X	X	X	X	X	X
1987 Superstition Hills, CA	6.6	X	X	X	X	X	X
1994 Northridge, CA	6.7		X	X			
1983 Borah Peak, ID	6.9		X	X	X	X	X
1989 Loma Prieta, CA	6.9		X	X	X	X	X
1995 Hyogo-Ken Nanbu, Japan	6.9				X	X	X
1948 Fukui, Japan	7.3			X			
1964 Niigata, Japan	7.5	X	X	X	X	X	X
1991 Tehre-Limon, Costa Rica	7.6			X			
1999 Chi-Chi, Taiwan	7.6		X				
1999 Kocaeli, Turkey	7.6		X				
1983 Nihonkai-Chubu, Japan	7.7	X	X	X	X	X	X
1990 Luzon, Philippines	7.7		X	X			
1993 Hokkaido Nansei-oki, Japan	7.7		X	X			
1906 San Francisco, CA	7.9	X	X	X	X	X	X
1923 Kanto, Japan	7.9			X			
1964 Prince William Sound, AK	9.2	X	X	X	X	X	
Number of earthquakes		7	14	15	10	10	9

The Youd, Hansen, and Bartlett 2002 model is fully empirical and has a higher R^2 value for the linear regression used to create the model than the Bardet, et al. 2002 and the Rauch and Martin II 2000 model. However, the Youd, Hansen, and Bartlett 2002 model has been criticized for having a large penalty for fines content as liquefaction case histories become more common in sands with a large portion of fines. The Bardet, et al. 2002 model is slightly less accurate because less soil information is used in the model to make it simpler to use than the Bartlett and Youd 1995 model. Bardet, et al. 2002 hoped that this would make prediction easier for utility companies that needed to protect large areas from lateral spreading and have limited funds for soil investigation. Rauch and Martin II 2000 used an average displacement in the creation of the model to increase the number of case histories that can be used in his model. A lack of information on how the average displacement is calculated and how this value compares to the displacements measured at the site increases the uncertainty in the calculated displacements even though the predicted average displacement falls in the same 50 to 200% of the measured value range. These are the three lateral spreading models that also use a site-to-source distance as one of the variables in the model.

A major weakness of these three models for this study is the site-to-source distance ties the model to a particular region. The Chile case histories are outside the seismic region of the western United States and Japan that the models were created to predict in. In addition, the Alaska 1964 case histories represent the only site-to-source distances for subduction zones in the model. The differences between the site-to-source distances needed to attenuate a Chilean subduction zone and a strike-slip fault in California could cause erroneous values. Sensitivity to seismic region is challenging when trying to extend a model to a type of earthquake that is rare in lateral spreading case histories.

The Faris, et al. 2006 and the Zhang, Robertson and Brachman 2004 models both used lab data from cyclic shear tests in the prediction model to combine theoretical experience with empirical experience. While it is good to include sound theory with experience, not every lab test fully represents the mechanics of the field. By not including a variable in these models to account for the effects of depth and overburden pressure, the lab tests may not represent the soil mechanics in the field well enough to model lateral spreading more accurately than a fully empirical model. The model also compounds conservatism by including all liquefiable layers without regards to the effect of dilative behavior and only using the maximum displacements.

A major strength of the Zhang, et al. 2012 model is the use of local attenuation relationships to increase the applicability of the model to seismic regions outside of the western United States and Japan. Several case histories from Turkey and New Zealand were used to show how the Zhang, et al. 2012 model was able to better predict displacements in other seismic regions than models with a site-to-source parameter that tie the predictions to the characteristics of the seismic regions used to develop the model. A weakness of the model is that sites with a T_{15} layer greater than 10 meters frequently fall outside the prediction range for the model and T_{15} variable has a different coefficient for the free-face and gentle sloping cases. Another weakness of the model for this study is that the Alaska 1964 earthquake with a magnitude of 9.2 was not used in the development of the model.

4 SEISMIC PROPERTIES OF RECENT SUBDUCTION ZONE EARTHQUAKES

The seismic parameters reported for large magnitude earthquakes can vary greatly between authors because the combination of new technologies and the rare occurrence of large magnitude earthquakes makes it difficult to standardize one method for the calculation of seismic parameters. When the Maule Chile 2010 earthquake ruptured, it was the fifth largest earthquake to ever be recorded. Recent advances in technology, such as continuous GPS recordings, provide new information to interpret and an increased understanding of the way energy is released. New technologies have made it easier to find asperities or areas where large slip initiated that is separate from the epicenter. GPS and teleseismic data are better at capturing low frequencies while near-source strong motion data are better at capturing motions at high frequencies (Goda and Atkinson 2014). These technologies capture different but important characteristics of the same earthquake. This chapter highlights the variability of seismic parameters for the same megathrust subduction earthquake found in published scientific literature and then reviews the seismic parameters reported for the Maule Chile 2010 earthquake.

4.1 Site-to-Source Distances in Subduction Zones

Goda and Atkinson 2014 described the effects of site-to-source distances on the development of attenuation relationships for three megathrust subduction earthquakes: 2011 M9.0 Tohoku, 2003 M8.3 Tokachi-oki, and 2005 M7.2 Miyagi-oki. Some of the site-to-source

distances discussed include: Joyner-Boore distance (distance to the surface projection of the fault plane or seismogenic zone), epicentral distance, hypocentral distance, and rupture distance (shortest distance to fault rupture plane). Figure 4-1 shows the site-to-source distances as calculated for a subduction zone. These distances are separated into two categories depending on whether the source is defined by a point or an extended source such as a line or plane. Since larger fault rupture areas are difficult to define accurately with just one point, it has become standard practice to use extended source measurements to develop ground motion prediction equations for large magnitude earthquakes (Goda and Atkinson 2014). In addition, for megathrust subduction earthquakes it is very common to have more than one reported epicenter and asperities increasing the difficulty of defining the distance to the epicenter. For example the Japanese Meteorological Agency, U.S. Geological Survey, and Harvard Global calculated different epicenters for all three earthquakes included in this study.

The majority of the research focused on how different fault rupture models for the same earthquake effected the development of attenuation relationships. Attenuation relationships were created for each earthquake using the fault rupture distance to define the site-to-source distances for each fault rupture model. The fault rupture models came from published articles in peer-reviewed scientific journals. Fault rupture models vary for the same earthquake because of differences in the shape (rectangle, circle, ellipse, etc.), boundary conditions (80%, 90%, or 100% of slip), and the data source (teleseismic, strong motion, tsunami generation, or GPS) inverted to create the model (Goda and Atkinson 2014). The fault rupture model changed the slope of the relationship between the fault rupture distance and peak ground accelerations predicted by the attenuations for all three earthquakes. Differences between fault rupture models were the most pronounced in the attenuation relationships for the 2011 M9.0 Tohoku because of

the larger rupture area for the models to define. Another finding of the study was that the variance was larger for peak ground acceleration than for spectral accelerations at longer periods. Atkinson and Goda hypothesize that this difference occurs "because the short-period content of the ground shaking is most strongly affected by local features/asperities, whereas the long-period content is influenced by more macroscopic features of the fault rupture (Goda and Atkinson 2014). Using spectral accelerations at longer periods and an extended source measurement can help limit variability for megathrust subduction earthquakes.

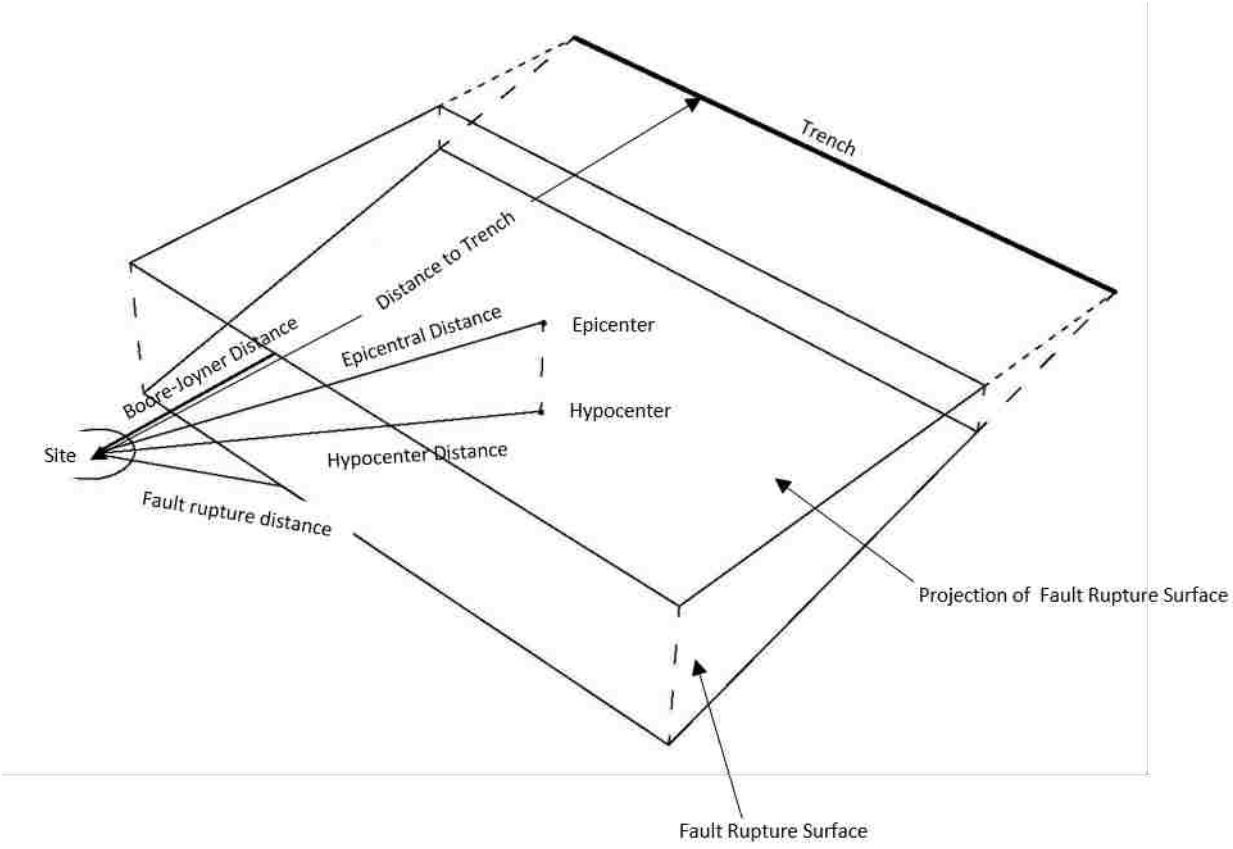

Figure 4-1: Definitions of Several Site-to-Source Distances

4.2 Epicenter and Asperity Locations

Multiple epicenter locations were reported for the Maule Chile 2010 earthquake. The epicenters most often referenced in scientific literature were reported by the National Seismological Service of the University of Chile, the U.S. Geological Survey, and by Vigny et al. 2011. The National Seismological Service of the University of Chile (SSN) and the U.S. Geological Survey (USGS) both reported an initial estimate for the epicenter of the Maule Chile 2010 earthquake, which was corrected several months later when near source data finally became available (Ruiz, et al. 2012). The location of the epicenter was calculated using far-field stations (USGS), short-period seismological stations (SSN), and the arrival times from high-rate GPS sites (Vigny et al 2011). Ruiz et al. 2012 noticed two distinct pulses in the ground velocities derived from continuous GPS records that, based on duration, indicated they originated from localized asperities during the earthquake. Using displacement records from six strong motion stations and the updated SSN hypocenter, they were able to identify the locations of two asperities that originated at 24 and 62 seconds into the earthquake respectively. The locations of these original epicenters, updated epicenters, and asperities are presented in Table 4-1. Original epicenter locations are included because these epicenters had been referenced in several journal publications prior to the updated values being released. There is a slight discrepancy between the epicenter locations reported by the USGS in several published articles so the location may have been updated several times before the release of the official updated location.

Table 4-1: Epicenters Reported for Maule Chile 2010 Earthquake

Source	References	Latitude	Longitude	Depth
USGS-Original Epicenter	(U.S. Geological Survey 2013) (Lay, et al. 2010)	35.909 S	72.733 W	35.0 km
	(Sladen n.d.)	35.846 S	72.719 W	35.0 km
	(Ruiz, et al. 2012)	35.83 S	72.66 W	35.0 km
USGS-Updated Epicenter	(U.S. Geological Survey 2014), (Ruiz, et al. 2012)	36.122 S	72.898 W	22.9 km
SSN-Original Epicenter	(Ruiz, et al. 2012)	36.25 S	72.96 W	47.4 km
	(Delouis, Nocquet and Vallée 2010)	36.208 S	72.96 W	32 km
SSN-Updated Epicenter	(Conteras and Boroschek 2012), (Ruiz, et al. 2012)	36.29 S	73.24 W	30.1 km
Vigny et al. 2011 Epicenter	(Ruiz, et al. 2012)	36.41 S	73.18 W	26.0 km
Ruiz et al. 2012 Asperity 1	(Ruiz, et al. 2012)	35.80 S	72.90 W	25.0 km
Ruiz et al. 2012 Asperity 2	(Ruiz, et al. 2012)	34.90 S	72.50 W	25.0 km
Delouis 2010 Asperities	(Delouis, Nocquet and Vallée 2010)	See Figure 4-2		

4.3 Fault Rupture Models

Multiple fault rupture models have been proposed for the Maule Chile 2010 earthquake. Most of the authors agree that there was little to no slip along the Atacama trench and that the slip stopped around a depth of 50km. Small slip along the Atacama trench is consistent with the low severity of the tsunamis following the Maule Chile 2010 earthquake compared to the magnitude of the earthquake. The fault rupture models have similar differences to the ones found by Goda and Atkinson 2012 for Japanese earthquakes. The durations of rupture used in the models were 90 seconds (Ruiz, et al. 2012), 110 seconds (Delouis, Nocquet and Vallée 2010), 130-150 seconds (Lay, et al. 2010), and 150 seconds (Sladen n.d.). The duration varied between authors because a majority of the energy was released in the first 90 seconds and only small accelerations were recorded during the last minute. Table 4-2 shows the strike, dip, and rake calculated for different fault rupture models. There was a lack of measurements such as strong

motion measurements and GPS measurement south of the rupture model to help define the south end of the model.

Table 4-2: Strike, Dip, and Rake for Fault Rupture

Source	Reference	Strike	Dip	Rake
USGS-CMT	(U.S. Geological Survey 2010)	14	19	104
Global-CMT	(Ekstrom and Nettles 2010)	18	18	112
Delious et. al.	(Delouis, Nocquet and Vallée 2010)	15	18	110
Lay et. al.	(Lay, et al. 2010)	18	18	112
Ruiz et. al.	(Ruiz, et al. 2012)	Elliptical Parameterization		
Sladen	(Sladen n.d.)	18	18	112

Delious, Nocquet and Vallée 2010 inverted a combination of GPS, teleseismic, and InSAR data to create their fault rupture model. A combination of data types was used to include accurate location and time data sets to better characterize the slip spatially and temporally. The data was inverted at low frequency using both the epicenter from the University of Chile and the original USGS epicenter. The first epicenter fit better so that epicenter was used for the model. The model showed bilateral movement to the north and south creating two slip zones. Areas of large slip were found north and south of the hypocenter indicating two asperities as shown in Figure 4-2. The model is an irregular shape. Ruiz et.al 2012 used elliptical parameterization and continuous GPS to create their model as shown in Figure 4-3. They used the more southern Vigny, et al. 2011 hypocenter to invert the data and found two asperities to the north. Lay, et al. 2010 inverted broadband teleseismic P, SH, and Rayleigh wave signals using the original USGS epicenter and the strike, slip, and dip calculated by the Global CMT solution. They also found bi-lateral movement away from the hypocenter similar to Delious et al.'s model. Anthony Sladen from Caltech used teleseismic P waves, the Global CMT solution, and an early released USGS hypocenter to create his fault rupture model. His fault rupture model is similar to the Lay, et al. 2010 model as shown in Figure 4-5.

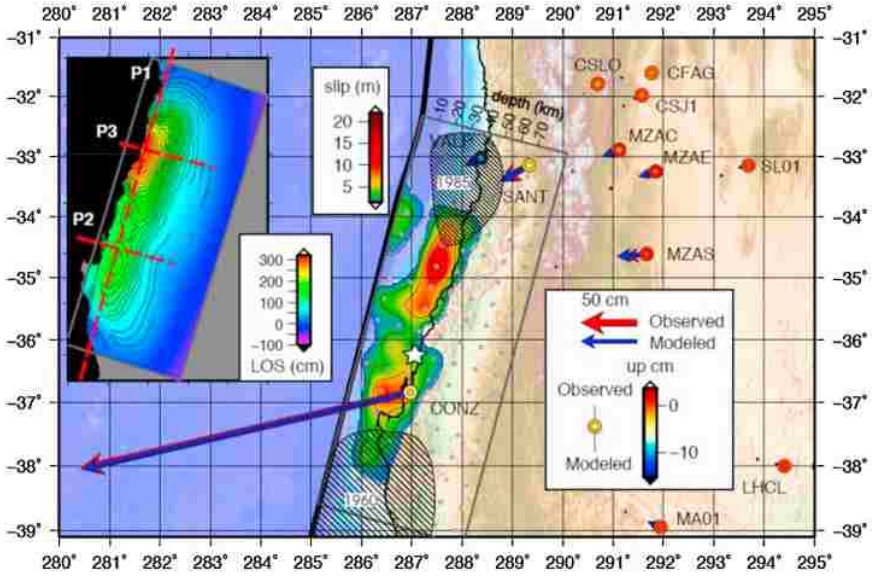

Figure 4-2: Delouis, Nocquet and Vallée 2010 Model

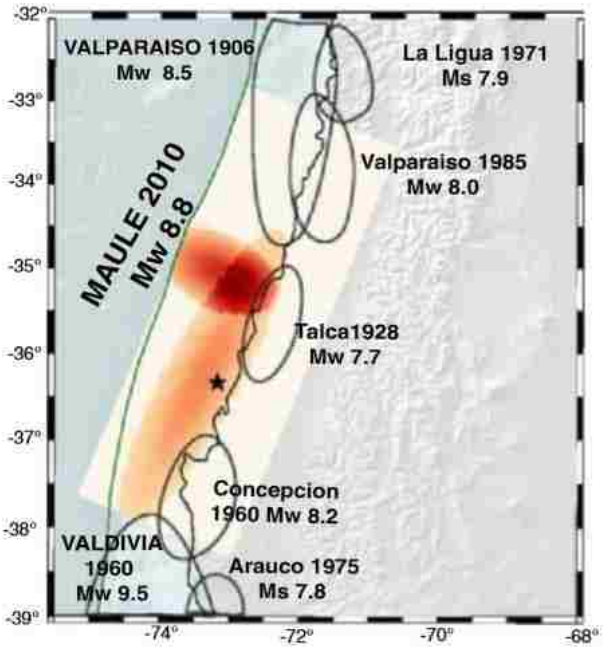

Figure 4-3: Fault Rupture Model (Ruiz, et al. 2012)

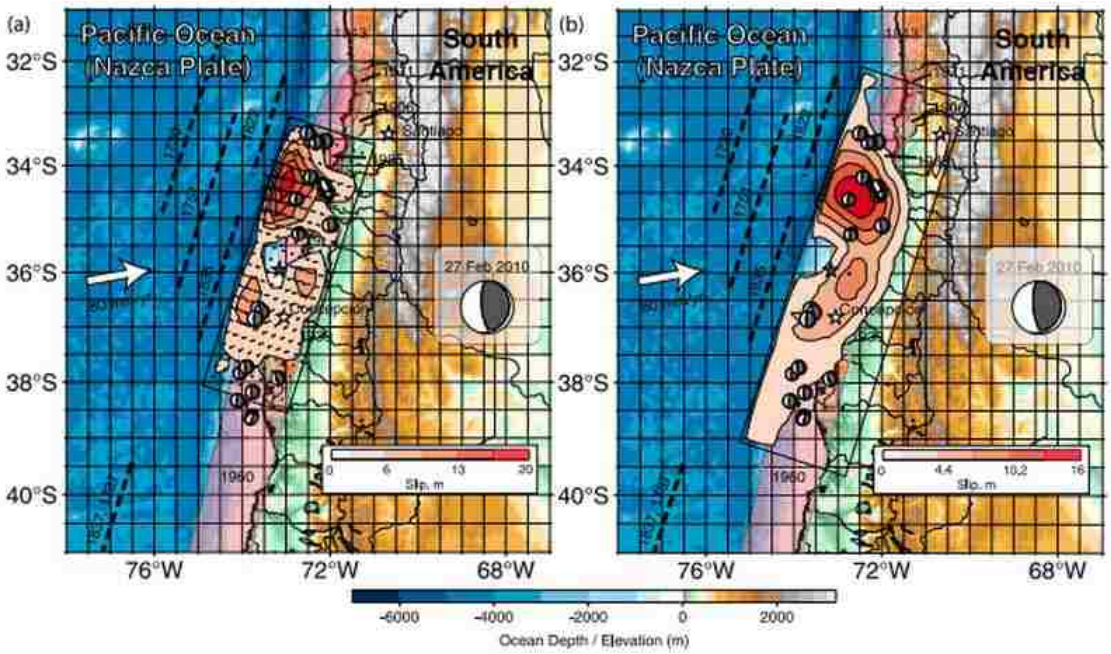

Figure 4-4: Slip with (b) and without (a) Rayleigh Waves (Lay, et al. 2010)

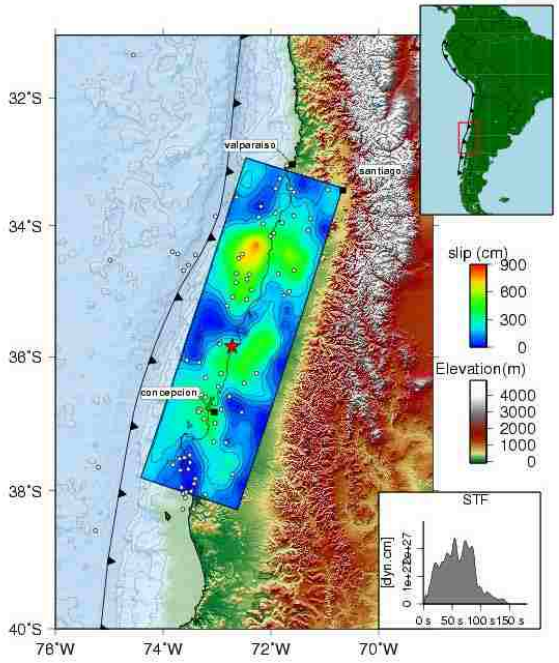

Figure 4-5: Fault Rupture Model (Sladen n.d.)

4.4 Local Chilean Attenuation Relationship

The subduction zone between the Nazaca and South American plate is one of the most active in the world but few local attenuation relationships exist for it. The first attenuation model for the Chilean region to include estimates of spectral accelerations was developed by Conteras and Boroschek 2012. Records from Chilean interplate earthquakes occuring between 1985 and 2010, including the Maule Chile 2010 earthquake, were used to develop the model. Below are the equations for both peak ground accelearation and the spectral acceleration at 0.5 seconds.

Peak Groun Acceleration:

$$\log(Y) = -1.8559 + 0.2549M_w + 0.0111H - 0.0013R \\ -glog(R) + 0.3061Z \quad (29)$$

Spectral Acceleration at 0.5 seconds:

$$\log(Y) = -2.1228 + 0.3208M_w + 0.0094H - 0.0008R \\ -glog(R) + 0.2834Z \quad (30)$$

In the equations, Y is the peak ground acceleration or spectral acceleration with five percent damping, M_w is the moment magnitude, H is the focal depth in kilometers, R is given by:

$$R = \sqrt{R_{rup}^2 + \Delta^2} \quad (31)$$

where R_{rup} is the closest distance to the rupture surface in kilometers, Δ is the near Source Saturation Term given by:

$$\Delta = 0.0734 * 10^{0.3552M_w}, \quad (32)$$

g is the geometrical spreading coefficient:

$$g = 1.5149 - 0.103M_w, \quad (33)$$

and Z is zero for rock sites and one for soil sites.

Ground motions prediction equations for subduction zones around the world had underpredicted accelerations for Chile in the past. Contreas and Borochek 2012 compared their attentuation with two recent interface subduction zone attenuations; Atkinson and Boore 2003 and Zhao, et al. 2006. Figure 4-6 shows the measured and predicted response spectras for sites from three earthquakes. The legend on the figure shows the site classes used for curves from Atksion and Boore 2003, abbreviated A&B 2003, and Zhao et al. 2006, abbreviated Z (2006). The attenuation shows good agreement between the predicted and observed accelearations at the six sites.

The bilateral movement of the Maule Chile 2010 earthquake caused different accelerations to be recorded in the north and the south. Accelerations in the south were smaller than the accelerations measured in the north at the same distance from the fault rupture surface. The case history sites in this study are located in the southern part of the rupture zone so it is likely that the predicted displacements will be slightly high. Figure 4-7shows the predicted verses measured accelerations for the Maule Chile 2010 earthquake with the Conteras and Boroschek 2012, Atkinson and Boore 2003 (AB03), and Zhao et. al 2006 (ZEA06) attenuations. The closest ground motion station to our site, in Concepcion, plotted below the curve for soil sites with recorded a peak ground acceleration of 0.4g. This attenuation was used for the case histories because it is the best attenuation relationship available for Chile and represents the uncertainty inherent in designing for futre earthquakes where no acceleration data will be available. However, where displacements were over predicted and accelerations are influential to the model a comparison is made to the displacements predicted with the peak ground acceleration of 0.4g.

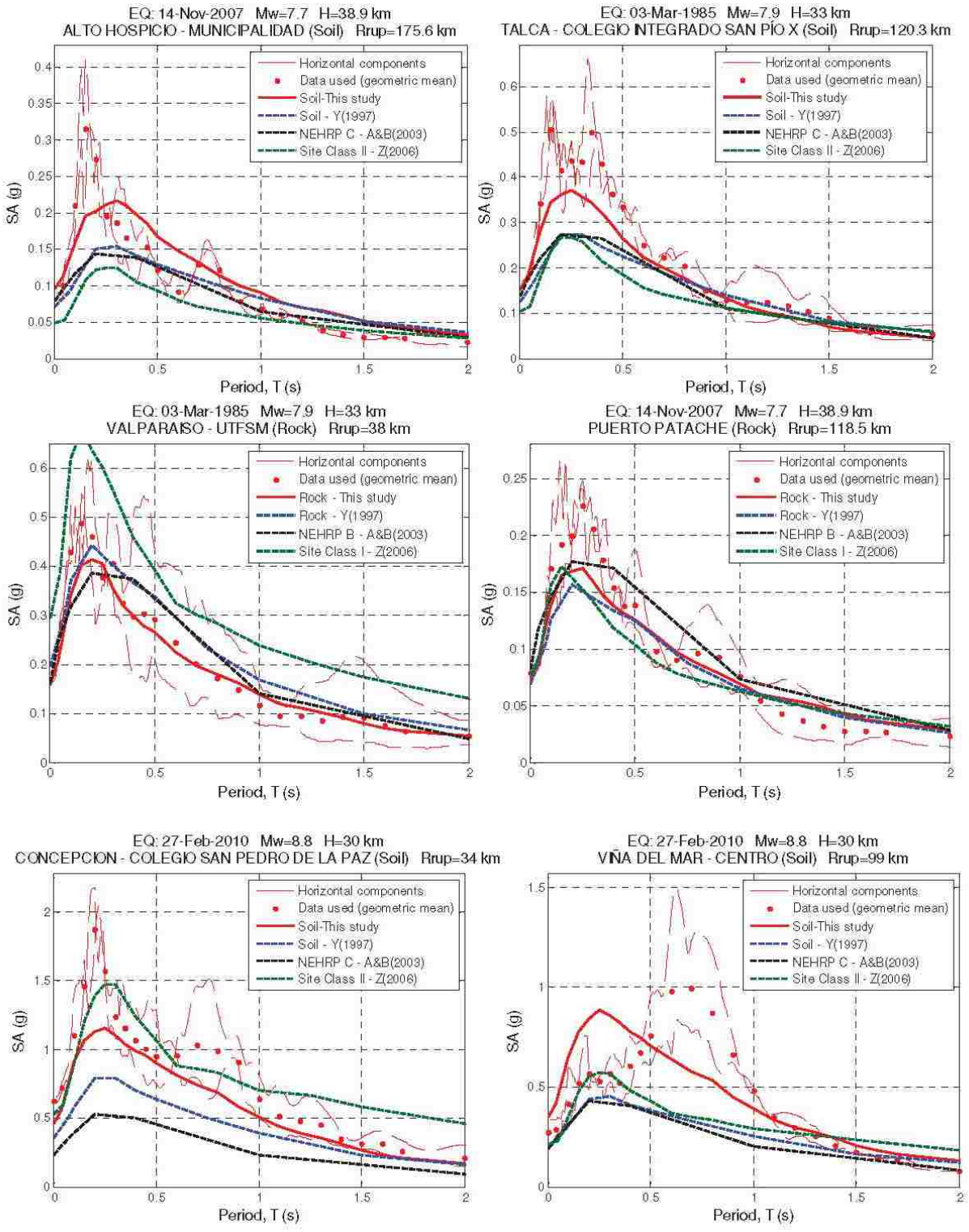

Figure 4-6: Measured Verses Predicted Response Spectra

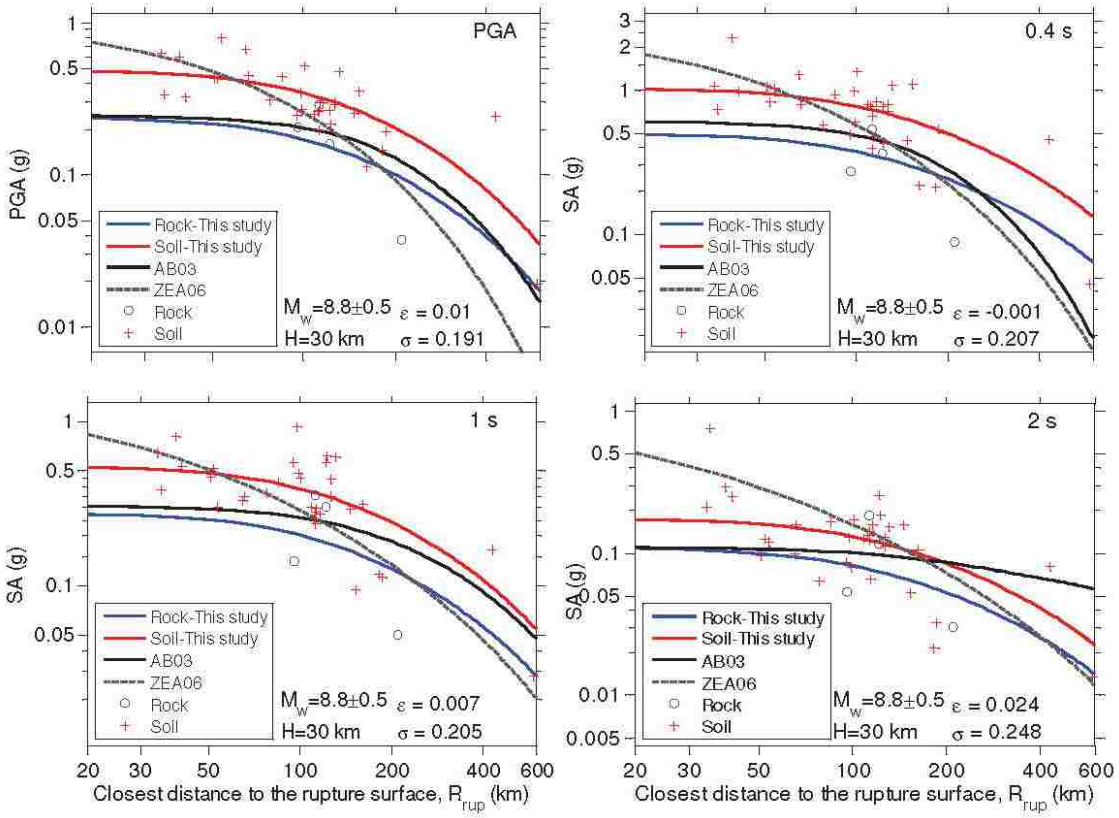

Figure 4-7: Measured Verses Predicted Accelerations for the Maule Chile 2010 Earthquake

5 PORT OF CORONEL

5.1 Lateral Spreading Case History Sites

Shortly after the Maule Chile 2010 Earthquake, the Geotechnical Extreme Events Reconnaissance team visited several sites affected by lateral spreading. Lateral spread displacements were observed and measured at several ports. Damage from lateral spreading was especially prevalent at the Port of Coronel located approximately 22 kilometers southwest of Concepcion as shown in Figure 5-1. Reports of the damage were published in the Earthquake Spectra as: "Effects of Ground Failure on Buildings, Ports, and Industrial Facilities" and "Performance of Port Facilities in Southern Chile during the 27 February 2010 Maule Earthquake" (Bray, et al. 2012) (Brunet, et al. 2012). In the Port of Coronel, signs of lateral spreading were observed at two piers and between the piers as shown in Figure 5-2. In the reports, the north pier was named the North Coronel Pier and the south pier was named the South Coronel Pier. Several horizontal displacements were measured along two survey lines labeled Line 1 and Line 2 as shown in Figure 5-3. Cracks in concrete and asphalt from lateral spreading were observed in the port and at a skate park and pier to the north of the port. This area experienced extensive damage with more damage in the north than the south.

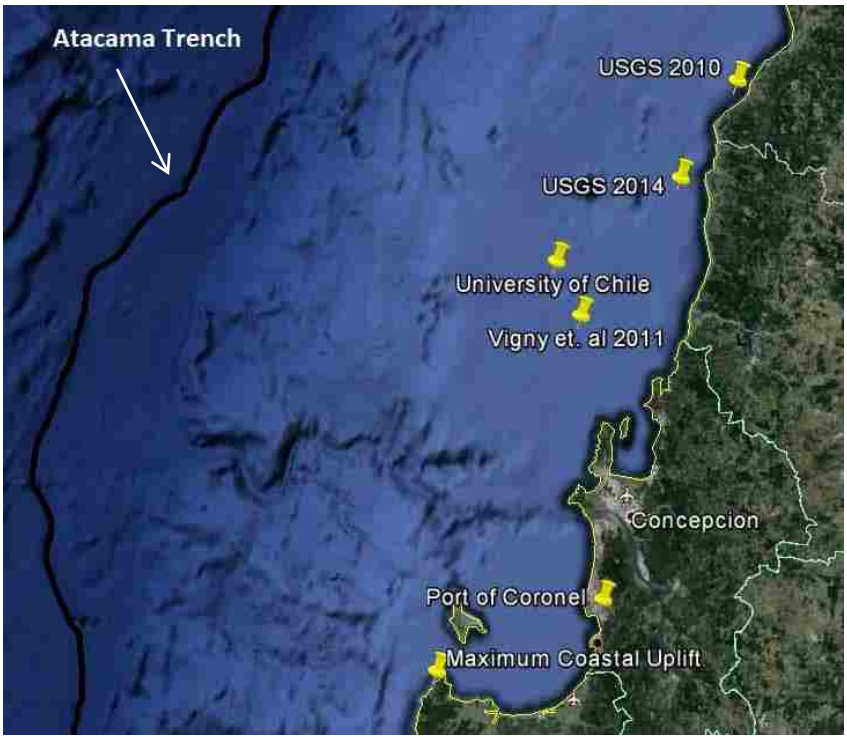

Figure 5-1: Map of Port of Coronel Relative to the Atacama Trench and Epicenters (Map from Google Earth)

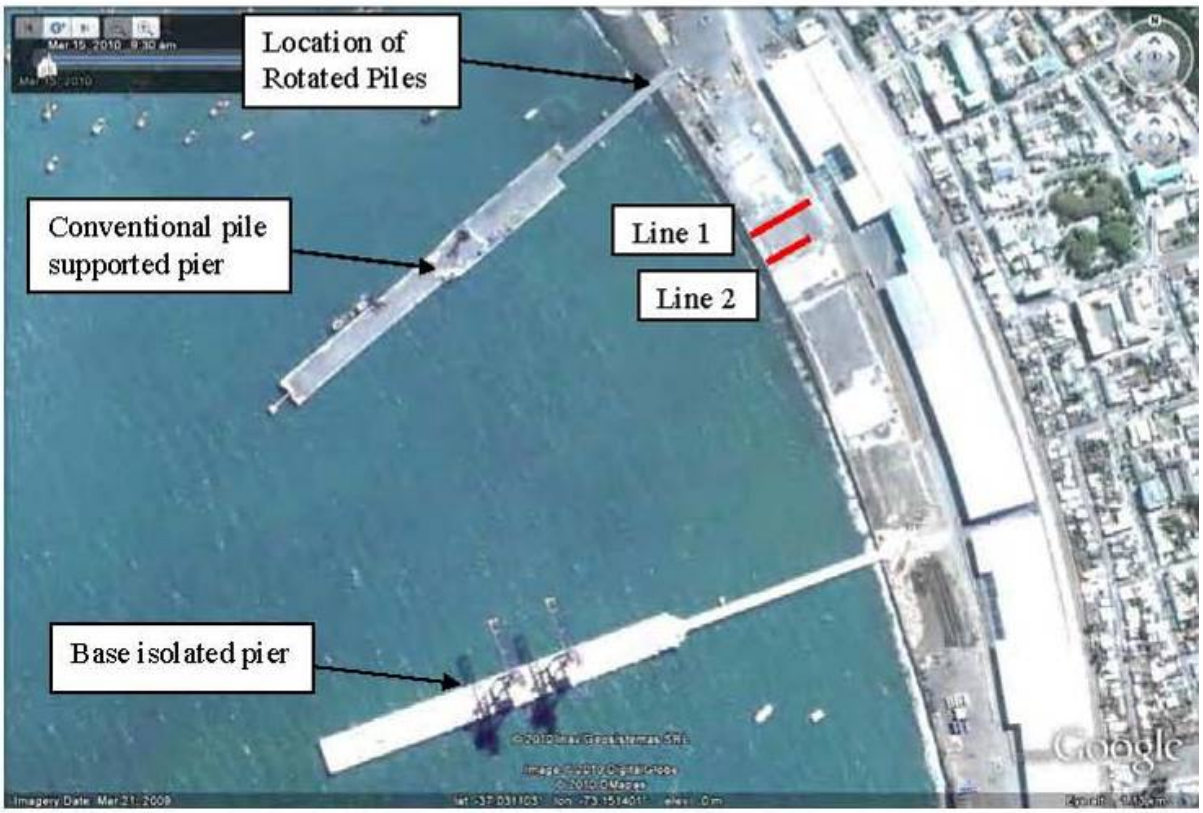

Figure 5-2: Location of North and South Piers. Photo from (GEER 2010)

Figure 5-3: Lateral Spreading Cracked the Asphalt Between the Coronel Piers (GEER 2010)

5.2 SPT and CPT Tests

Geovenor, a geotechnical company in Chile, performed several SPT tests and pile load tests for the construction of both the north and south pier in the Port of Coronel. At the north pier, several SPT tests were performed in 1995 before the original construction of the pier and some additional tests were made in 2003 prior to the second expansion of the pier. In 2006, several more SPT tests were performed for the construction of the south pier. These SPT tests characterized the seafloor well and established the location of bedrock along the length of the pier to ensure that the piles were driven deep enough. However, the majority of the liquefiable soils were located within the seventy meters of the shoreline and where only one SPT test was performed at the head of each pier. As part of this study, additional SPT and CPT tests were performed along the shore in 2014 to better characterize the soils above the seafloor that contributed to lateral spreading at these piers. Figure 5-4 shows the location of the tests conducted between 1995 and 2014.

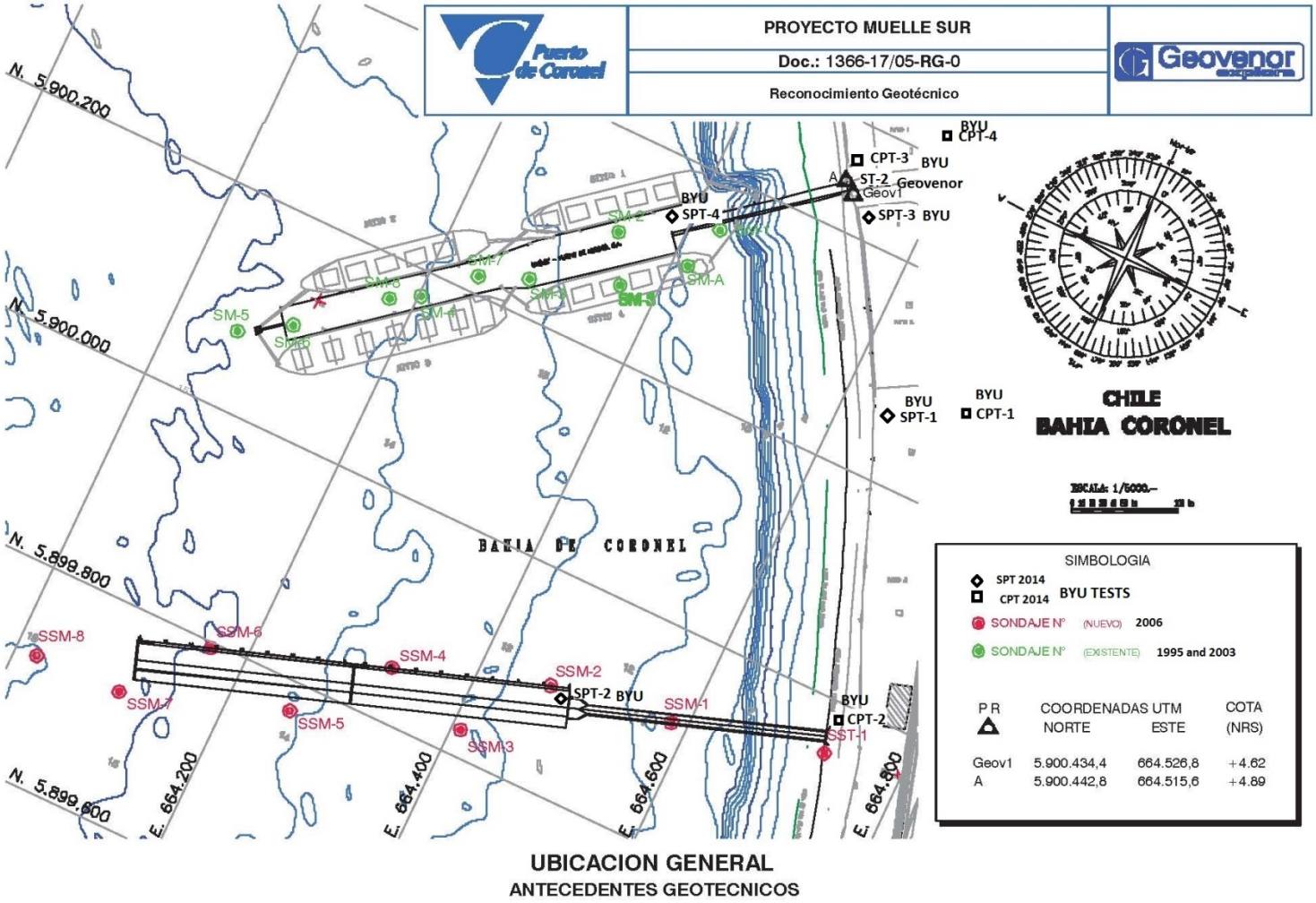

Figure 5-4: Locations of SPT and CPT Field Tests. Modified from (Geovenor 2006)

5.2.1 Soil Stratigraphy

Figure 5-9, Figure 5-16, and Figure 5-21, described subsequently in the chapter, show the cross-section of the sites with layering based on the results of the field tests. Five distinct layers were identified along the cross-section of each pier. The USCS classification and liquefaction susceptibility for each layer is described below.

Soil Layer S-1

Several meters of sands and silty sands that covers the seafloor along the shore. These sands were the major contributor to liquefaction and lateral spreading at all the sites. These soils generally had blow counts between 10 and 30. The majority of soils below the water table, depth of 4 meters, were liquefiable.

Soil Layer S-2

This two to four meter layer consists of a mixture of silts, clays, and sand. Having no consistent USCS soil classification, this very soft layer is called fango or sea mud by the local Chileans. SPT tests indicated an SPT blow count between 0 and 5 for this layer along the length of both piers.

Initially this layer was categorized as liquefiable because of lower plasticity indexes of 1 to 13 in the soil layer at the shore. The majority of the layer at the shore plotted within the Cetin, et al. 2004 liquefaction criteria based on plasticity index as shown in Figure 5-5. However, this layer was not included in the T_{15} layers for the lateral spreading models for several reasons. First, the layer is very inconsistent with frequent changes in plasticity index and USCS classification along the length of the piers. Portions of the layer were classified as elastic silt and fat clay with plasticity indexes in the low thirties. Second, this layer is too soft to cause damage to the piles but would flow around the piles if the layer was able to move. Lastly, including the

layer did not improve the prediction of any of the models and decreased the accuracy of predictions for at least three of the models. This was especially true for the Faris, et al. 2006 model where this layer added 2-2.5 meters of displacement to each site. Therefore, it was decided to not include this layer in the analyses.

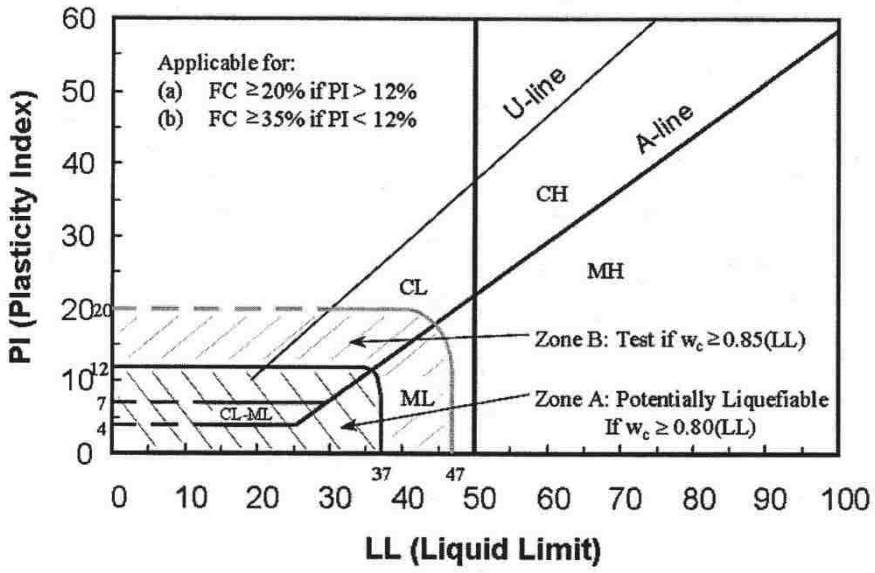

Figure 5-5: Seed et al 2001's Recommendations for Determining the Liquefaction Susceptibility of Fines (Faris 2004)

Soil Layer S-3

A well-compacted layer of silty sand with standard penetration rates greater than 50.

Soil Layer S-4

A layer of silts and clays from an eroded soft sedimentary rock layer with low cementation.

Soil Layer S-5

This bedrock layer consists of sedimentary rock with medium resistance.

5.3 Seismic Parameters

Due to the close proximity of the sites to each other, they all have the same seismic parameters. Table 5-1shows the seismic parameters used in the liquefaction and lateral spreading models that will be discussed subsequently. The peak ground acceleration and spectral acceleration at 0.5 seconds were both calculated using the local attenuation relationship developed by Conteras and Boroschek 2012. As discussed in Chapter 4, the duration of the earthquake used in equations varies by author because less energy was released the last minute of the earthquake. A duration value of 120 seconds was used because it falls in the middle of the duration range and the variability of the duration term is so small in the Rauch and Martin II model that the error bars on the prediction were the same width as the marker on the error plots. These values represent the best approximation of the seismic energy released at the sites.

Table 5-1: Seismic Parameters for the Maule Chile 2010 Case Histories

Parameter	Value	Source
Magnitude, M_w	8.8	Multiple
Peak Ground Acceleration	0.44g	(Conteras and Boroschek 2012)
Duration	120 s	Multiple
Spectral Acceleration (0.5s)	0.861 g	(Conteras and Boroschek 2012)

5.4 North Coronel Pier

The North Coronel Pier is a conventional pile supported pier built in 1996, which was expanded first in 2000 and again in 2004. At the North Coronel Pier, several piles supporting the pier were damaged by lateral spreading. The first three rows of piles rotated and two piles broke away from the deck and displaced over a meter. Piles located farther along the deck were not subject to lateral spreading forces and were supported by the stronger non-liquefiable S-3 and S-5 layers. While lateral spreading caused the piles closers to shore to move out to sea, these

seaward piles stayed in place causing compression forces in the deck. This caused the deck to stay in place while several piles moved seaward. Figure 5-6 shows the structure of the North Coronel Pier and the locations of the damaged piles.

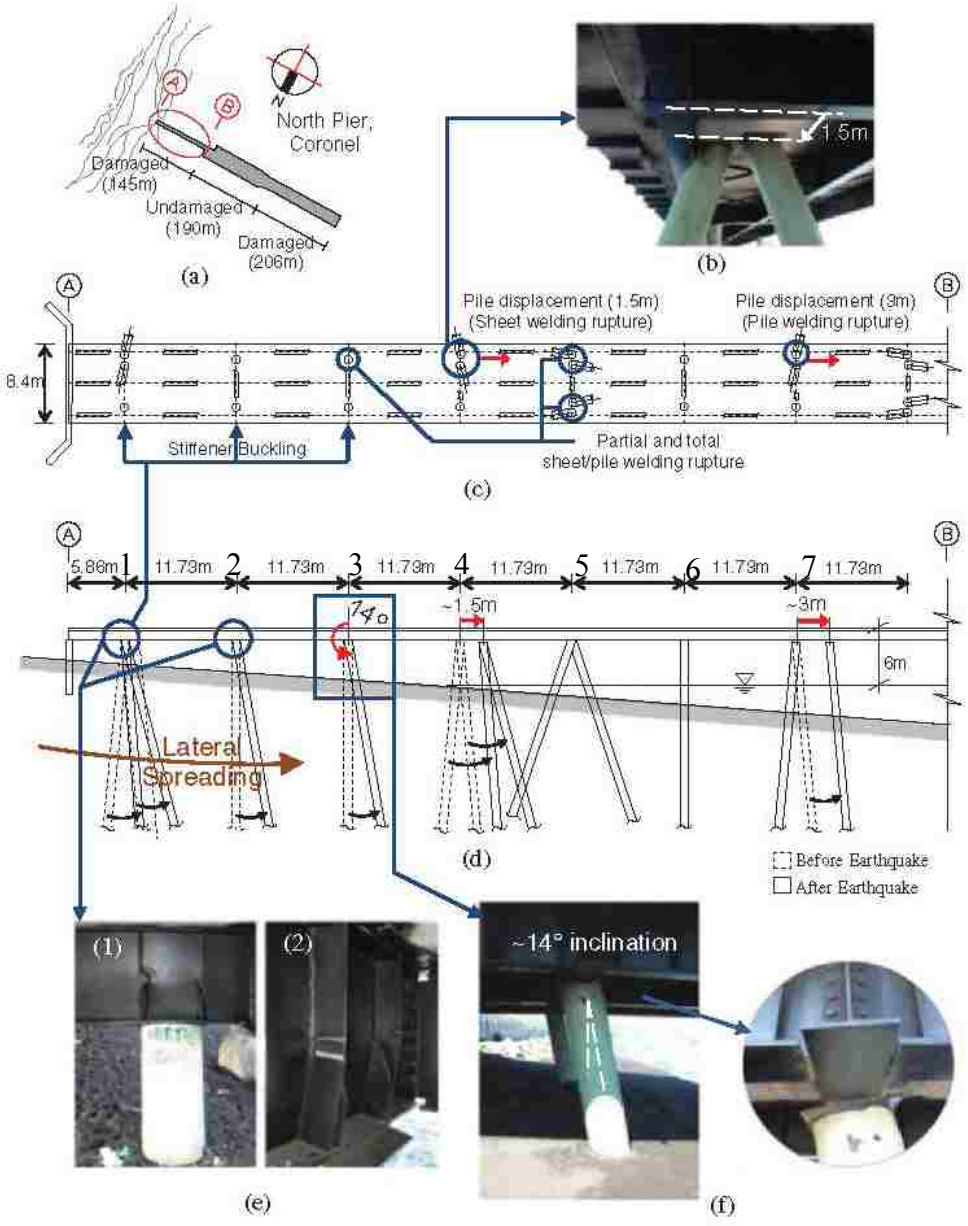

Figure 5-6: Damage at North Coronel Pier. Modified from (Brunet, et al. 2012)

Values for the rotations of pile row 1 and pile row 2 were measured in 2014. The ground displacement and angle measured in 2014 at the third row of piles was 0.48 meters and 12.2 degrees, somewhat lower than the 0.55 meters and 14 degrees measured in 2010. The measured rotations are considered a minimum value for ground displacement so it was decided to only use the largest lateral displacement which was measured in 2010 by Bray, et al. 2012 and Brunet, et al. 2012. Figure 5-7 depicts the rotation and properties of the piles in the third row. The pile displacements in Figure 5-6 are measured along the bottom of the pier instead of the ground surface. The pile that displaced 3 meters was battered with an angle of 20 degrees, a diameter of 560 cm, thickness of 14mm, and a moment of inertia of 46494.641 cm^4. An analysis in L-pile indicated that the pile would bend under the ground deformations at the transition between liquefiable and non-liquefiable soils making the displacement at the pier higher than the displacement at the ground surface. Without resistance at the pile head, the pile would freely rotate seaward under the ground deformations. Based on the angle of the bent pile, the displacement at the ground surface is about two-thirds to three quarters of the displacement at the top of the pier. The portion of pile above ground was smaller for the pile in row 4 and both of the battered piles moved together suggesting that the piles bent less as they moved. Figure 5-9 shows the soil layering along the cross-section of the north pier based on the results of several field tests.

Table 5-2: North Coronel Pier Lateral Spreading Displacements

Pile Row	1	2	3	4	5	6	7
Evidence of Lateral Spread	Pile Rotation	Pile Rotation	Pile Rotation	Pile Displacement	Ruptured Welds	None	Pile Displacement
Pile Rotation (°)	11.7	15.3	12.2/14	---	---	---	---
Ground Displacement (m)	0.27	0.3	0.48/0.55	1.5	---	---	2-2.25
Flange Rotation (°)	10.4	12.8	10	---	---	---	---

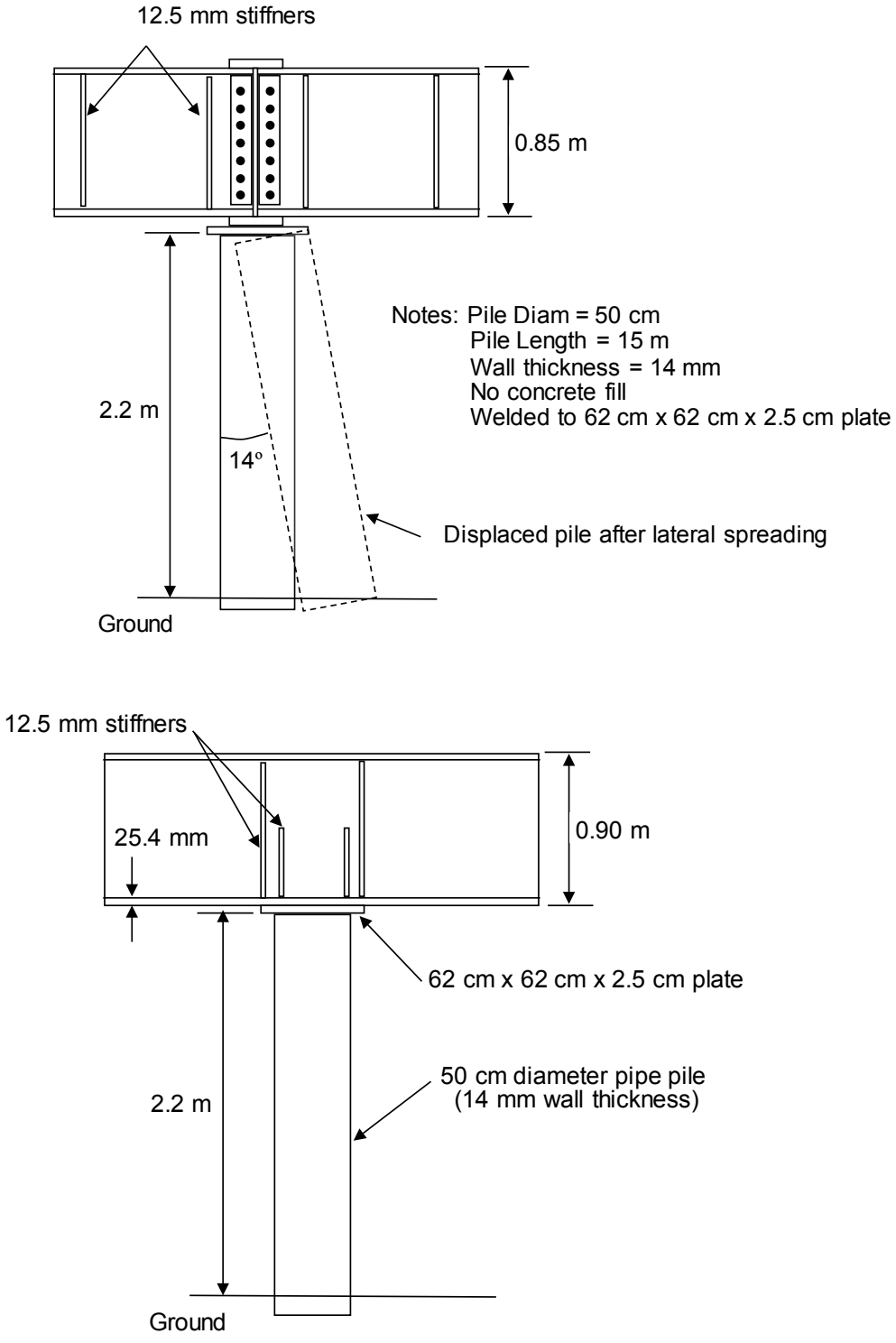

Figure 5-7: Longitudinal and Transverse View of the 14 Degree Pile Rotation (Bray, et al. 2012)

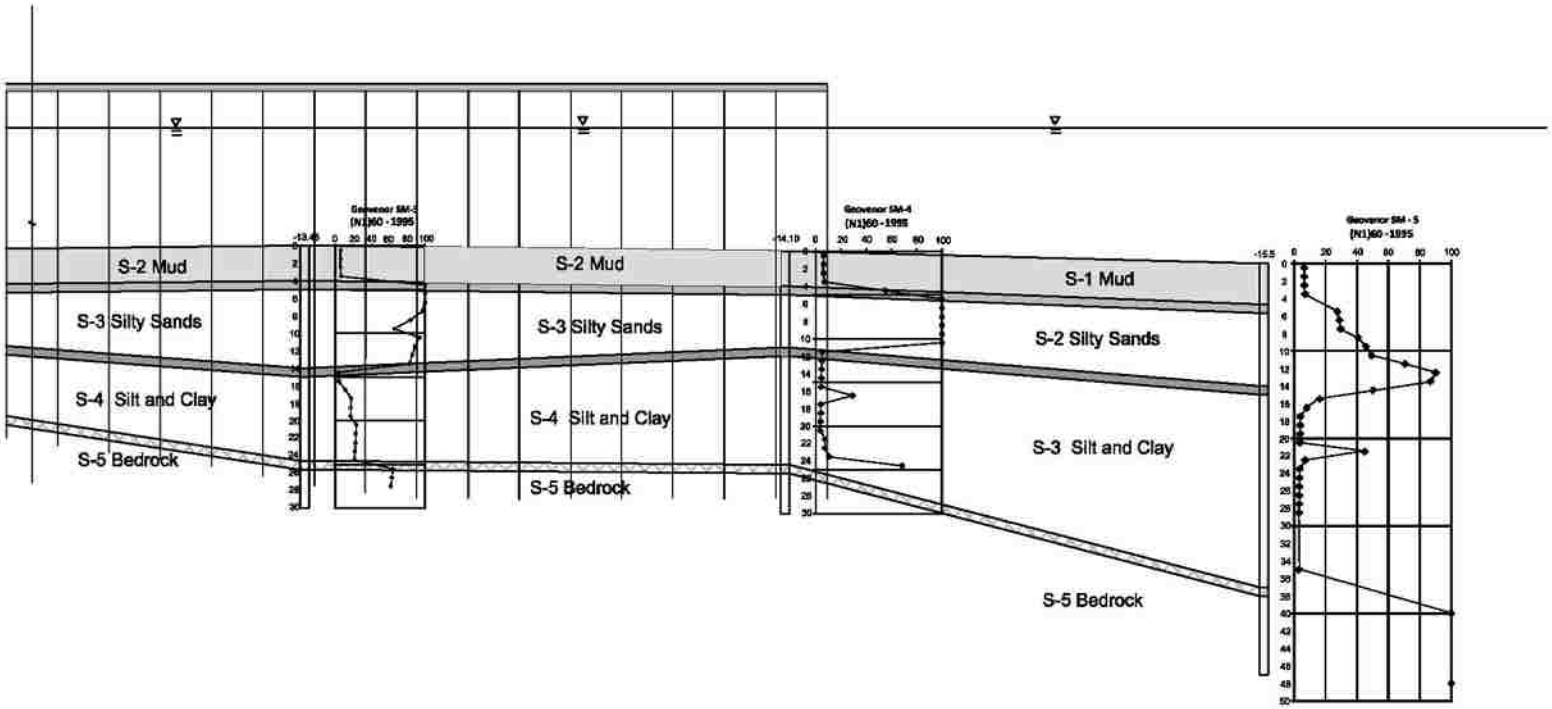

Figure 5-8: Cross-Section of Soil Conditions Based on Borings Along the Length of the North Pier at the Port of Coronel

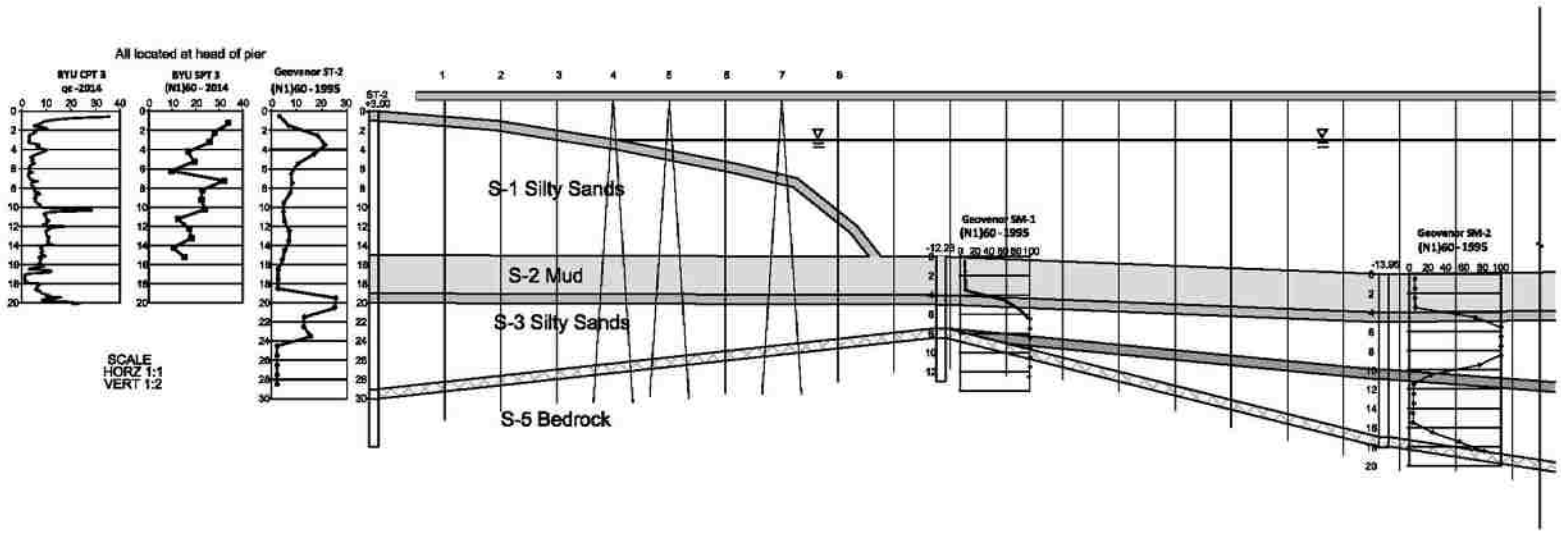

Figure 5-9: Cross-Section of Soil Conditions Based on Borings Along the Length of the North Pier at the Port of Coronel

5.4.1 Parameters for the North Pier

Several parameters are tied to the liquefaction analysis, including the T_{15} layer, F_{15}, and $D50_{15}$. Figure 5-10 shows the corrected values the three field tests conducted at the head of the north pier and the corresponding susceptibility of the layers to liquefaction and lateral spreading. Layers with corrected blow counts less than 30 and corrected cone resistance less than 200 are liquefiable, while layers with blow counts less than 15 are most susceptible to lateral spreading. The T_{15} layer is four meters thick at the north pier. Differences between the BYU SPT 3 test taken in 2014 and the test, ST-1, taken by Geovenor in 1995 may be due to changes that occurred to the soil during the construction of the north pier. For this reason, the BYU SPT 3 test took precedence in calculation of soil properties. The average fines content for the T_{15} layer ranged from 10-12% based on the test used to calculate the value.

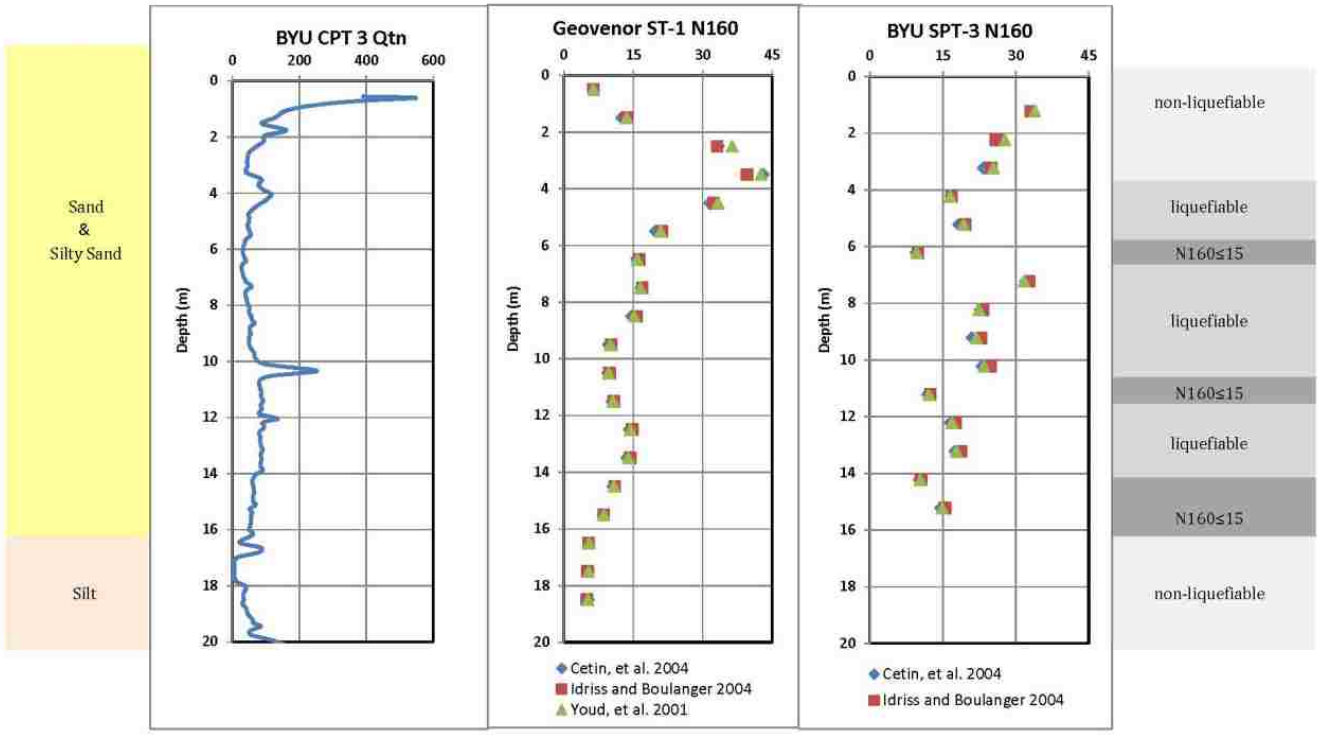

Figure 5-10: Liquefiable Soils at the North Pier

The $D50_{15}$ parameter was more challenging to calculate because only the SPT tests taken by Geovenor in 2006 along the south pier included a sieve analysis for the soil samples taken during the SPT tests. This data is not yet available for the SPT tests taken by Brigham Young University (BYU) in 2014 and was not included in the reports for earlier tests taken by Geovenor at the north pier in 1995. Future publications will include the lab data from the soil samples taken during the 2014 testing completed by BYU. The D_{50} values were calculated for each sample collected between the depths of 4-16 meters, the layers most susceptible to liquefaction at the sites, at the head of the South Pier. The D_{50} values for these layers ranged from 0.1 mm for soils with a high silt concentration to 0.6 mm for sands with very little silt with an average of 0.5 mm for layers with low fines. The geometry of the North Coronel Pier is best represented by a free-face ratio, W. For models where each lateral spread feature is independent, the free ratio is equal to 15% but it varies for models that include all displacements measured on a lateral spread feature.

Table 5-3: Parameters for the Liquefiable Layers at the North Coronel Pier

Parameter	Range	Best Value
T_{15}	4m	4m
F_{15}	10-12%	11%
$D50_{15}$	0.1-0.6mm	0.5mm
W	Varies	15%

5.5 South Coronel Pier

Although the North and South Coronel Piers are close together, smaller displacements were observed at the South Coronel Pier. An offset of 47 cm was measured at the head of the pier between the sheet pile wall and the pier abutment, as shown in Figure 5-12, but no parallel crack patterns were observed as was the case closer to the north pier. The only damage seen at

the south pier were signs of pounding at the joint between the abutment and the pier (Bray, et al. 2012). Another displacement of 24 cm was measured between the approach zone and the berthing zone due to excessive deformations in the base isolators of the South Coronel Pier. This pier performed better than the other piers and had less signs of both geotechnical and structural damage even though there were liquefiable soils at the head of the pier. Two theories exist for the lack of damage at the south pier.

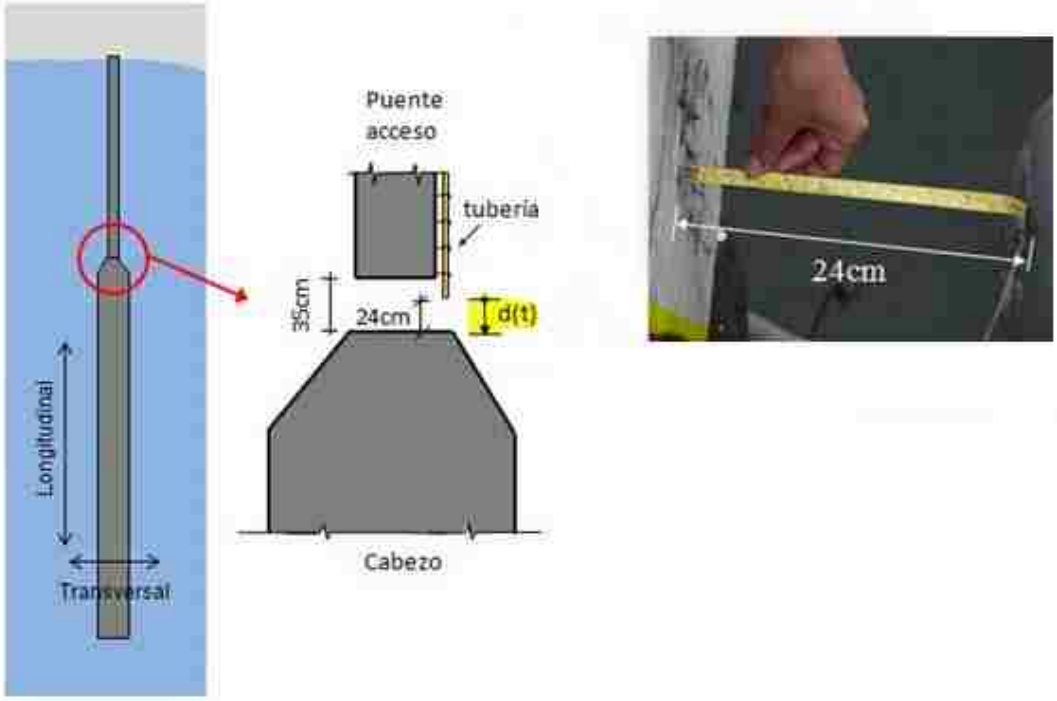

Figure 5-11: Separation of the Approach Zone and Berthing Zone at the South Pier (Photo from Eduardo Miranda)

One theory for the lack of damage to the South Coronel Pier was that the base-isolated system used in the design of the pier minimized distortion in the piles as shown in Figure 5-13. When the South Coronel Pier was built in 2006, groups of based isolated piles were used with flexible vertical piles to reduce the number of required piles and to increase the earthquake resistance of the pier. The second theory is that the soils at the South Coronel Pier were less

susceptible to lateral spreading decreasing the damage seen at the pier. At the North Coronel Pier, lateral spreading caused the piles near the shore to move seaward while the piles further from shore prevented this movement causing compression forces to build in the deck. Without lateral displacements there would not be the same forces in the piles at the south pier that caused pile rotations and displacements at the north pier. CPT soundings clearly showed significantly higher cone tip resistance at the South Coronel Pier as shown in Figure 5-14. Also shown in Figure 5-14 is a CPT profile for the Los Rojas pier that is located about 640 meters north of the North Coronel Pier and experienced the greatest lateral spreading displacement and greatest structural damage. The CPT profile at the Los Rojas pier shows the lowest tip resistance of the three. As the soils became denser, the damage observed at the pier decreased significantly indicating that the decrease in structural damage has some if not all geotechnical roots.

Figure 5-12: Displacement of Ground Relative to the South Coronel Pier

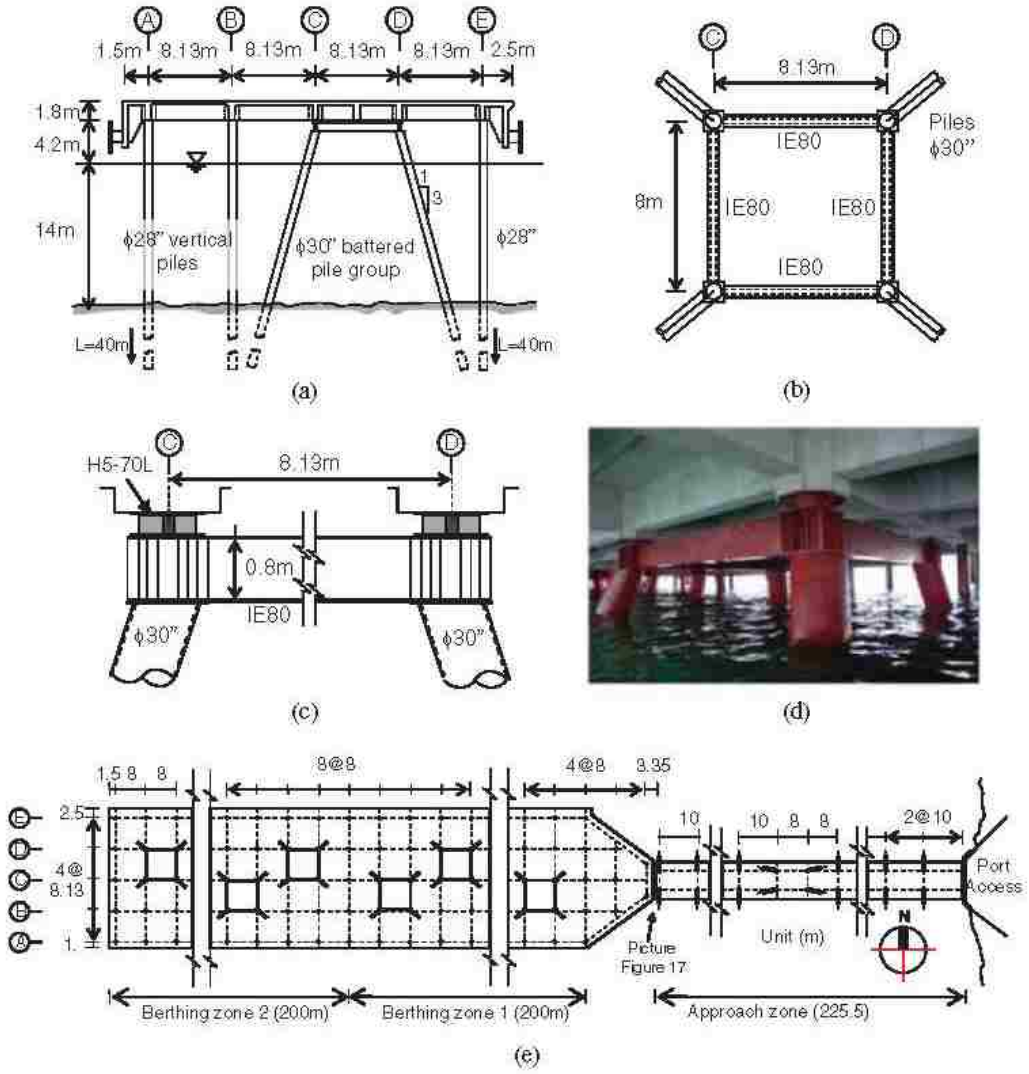

Figure 12. (a) Typical cross section of South Pier, Coronel. (b) Plan view of four battered-pile group. (c) LRB location on battered pile group. (d) Typical battered pile group. (e) Plan view of South Pier, Coronel.

Figure 5-13: Diagram of the Base-Isolation System for the South Coronel Pier (Brunet, et al. 2012)

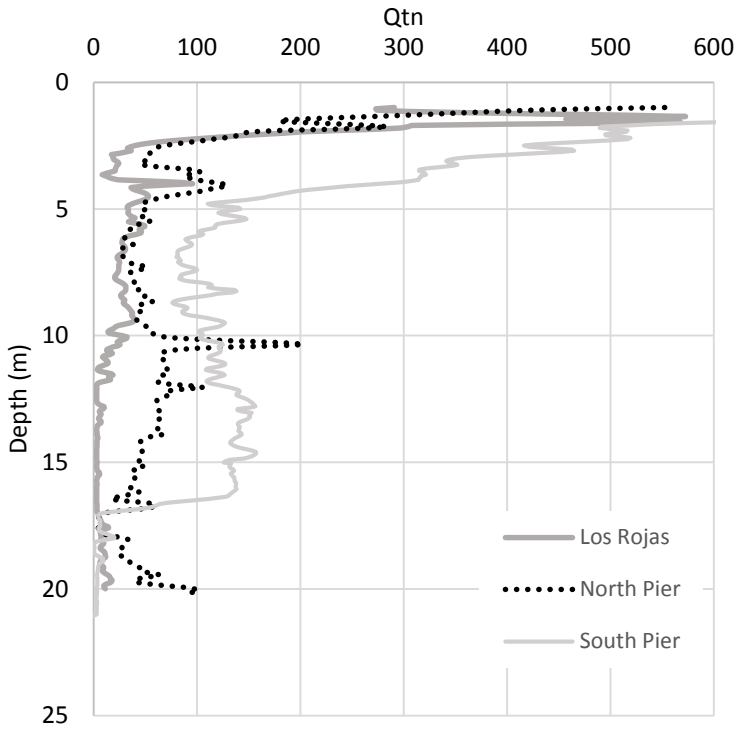

Figure 5-14: Comparison of Corrected Cone Tip Resistance for Three Piers

Originally the South Coronel Pier case history was not going to be included because no T_{15} layer was found in the SPT data for the South Pier as shown in Figure 5-15. However, a second review of the test data showed that the energy measurement had been assumed as sixty percent because no energy measurements were available for the SPT tests conducted by Geovenor. It was found that if the energy measurement was decreased to 55% that there would be a 1.4 meter thick T_{15} layer. This is consistent with the BYU SPT tests that had an energy measurement of 55% and a standard deviation of 5%. The lack of a T_{15} could be attributed to using the wrong energy measurement or the variability between blow counts that can occur when using a manual operation instead of an automatic hammer.

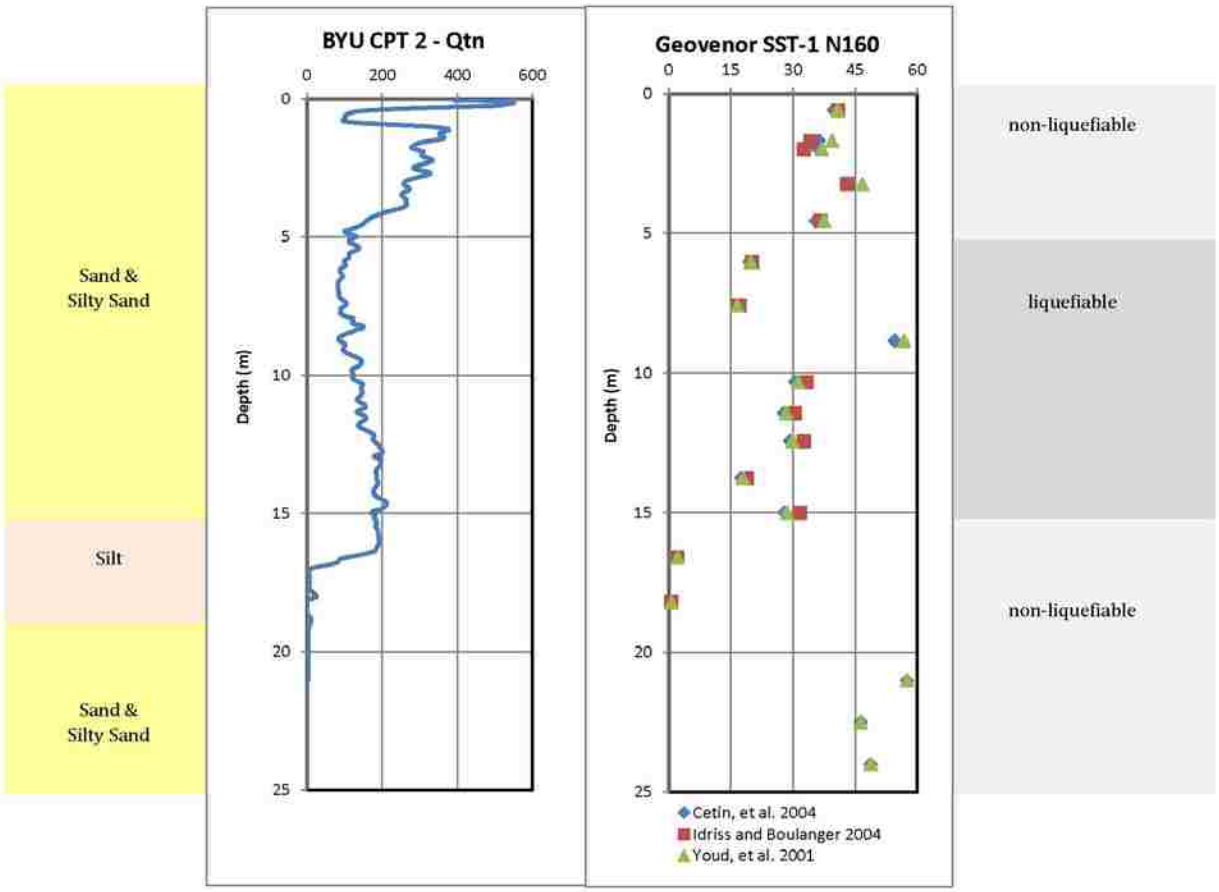

Figure 5-15: Soil Layers Susceptible to Liquefaction and Lateral Spreading at the South Pier

Figure 5-16 shows a cross-section of the South Coronel Pier based with soil layering based on field tests. The fines content and mean diameter size for the T_{15} layer are 43% and 0.1mm as shown in Table 5-4. These are the parameters used subsequently in models with a T_{15} layer. W_1 is the free-face ration calculated to the bottom of the T_{15} layer and W_2 is the free-face ratio for the entire feature. W_1 is used any model that uses a T_{15} layer.

Table 5-4: Parameters for the T_{15} Layer at the South Coronel Pier

Parameter	Range
T_{15}	0-1.4m
F_{15}	43%
$D50_{15}$	0.1mm
W_1	12.5
W_2	13.7

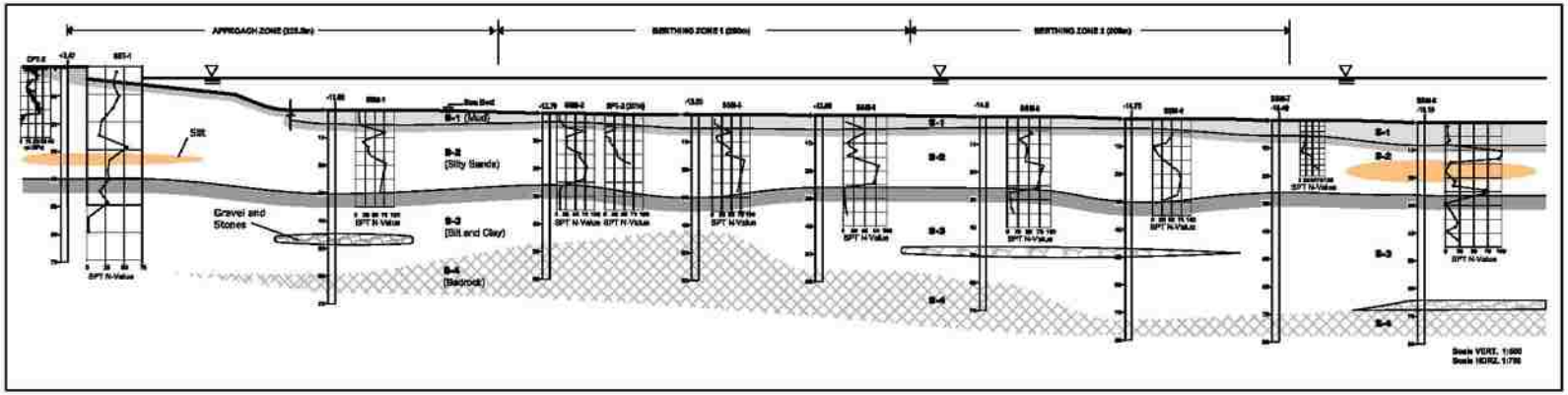

Figure 5-16: Cross-Section of Soil Conditions Based on Borings Along the Length of the South Pier at the Port of Coronel

5.6 Lateral Spread Displacements Between the Piers

Lateral spreading caused several cracks to form between the north and south piers. The cracks ran parallel to a 9 meter deep sheet pile wall between the two piers as shown in Figure 5-3. Measurements were taken along two survey lines that ran parallel to each other. Figure 5-19 shows the cumulative ground displacement obtained by summing the crack widths with distance from the sheet pile wall along each survey line. Additional damage included toppled containers and sink holes above cracks in the underlying drainage pipes as shown in Figure 5-17 and Figure 5-18, respectively. The ground sloped gently with an average slope of 3.5 percent where the survey lines were taken.

Figure 5-17: Toppled Containers at the Port of Coronel (GEER 2010)

Figure 5-18: Sink Holes at the Port of Coronel (GEER 2010)

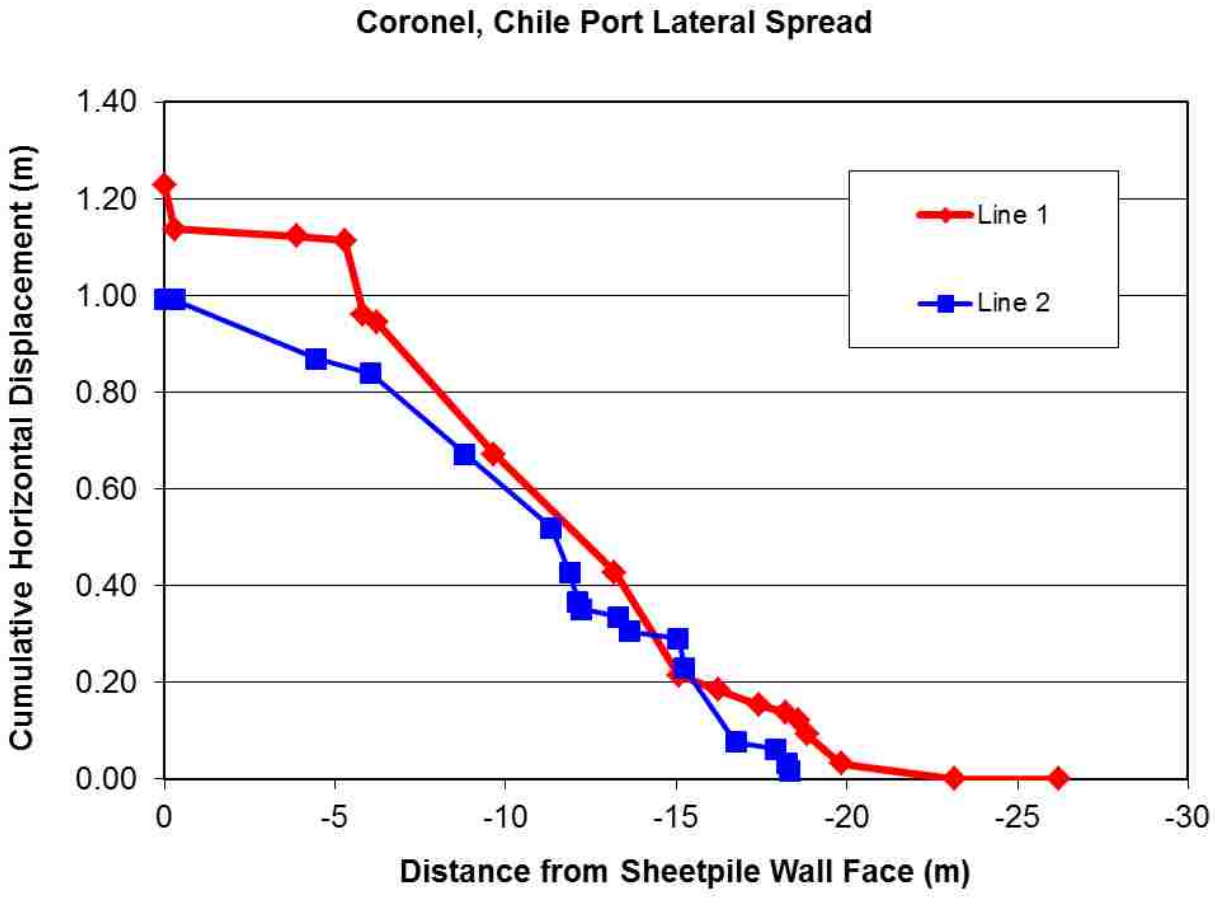

Figure 5-19: Line 1 and 2 Survey Measurements (Bray, et al. 2012)

The T_{15} layer was ten meters thick at this site suggesting that the soils at the north and south pier were denser, presumably because of soil compaction during construction of the piers. Figure 5-20 shows the layers susceptible to lateral spreading based on the SPT and CPT tests and Figure 5-21 shows a cross-section of the soil profile for this area of the port based on the SPT and CPT data. The fines contents of 10% for this site came from CPT correlations based on soil type because lab data is unable for the BYU SPT tests at this time. The average D_{50} value of 0.5mm from the South Coronel Pier lab data was also used at this pier.

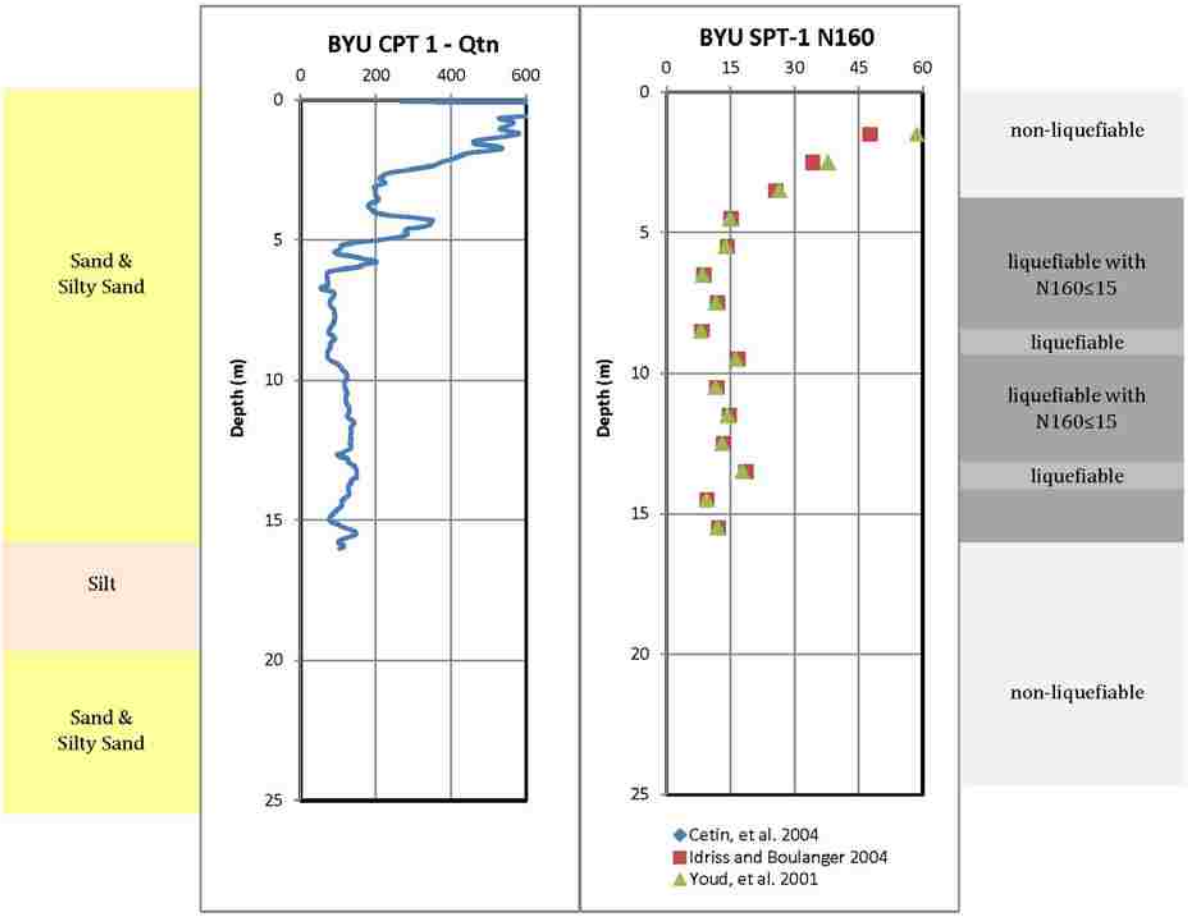

Figure 5-20: Soil Layers Susceptible to Liquefaction and Lateral Spreading at the Sea Wall Site

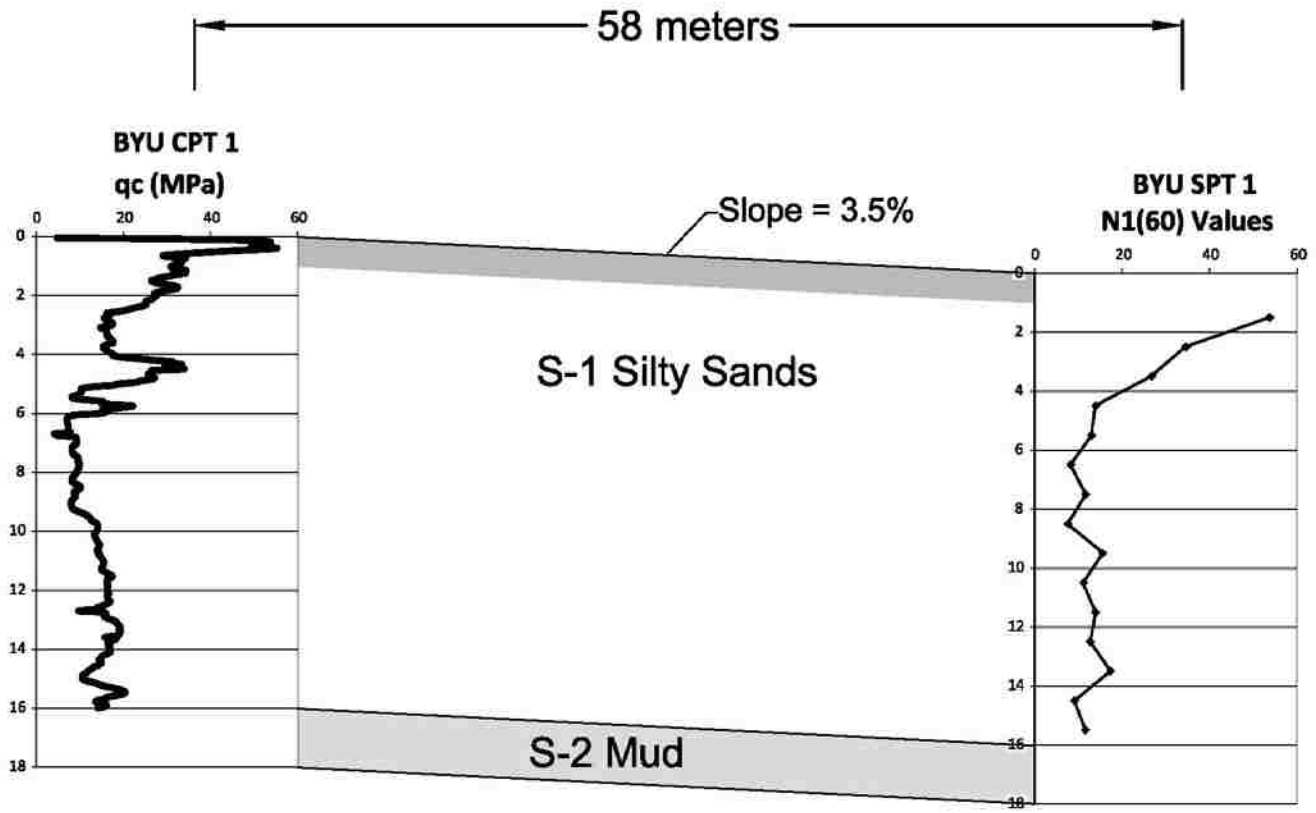

Figure 5-21: Cross-Section of Soil Conditions from Borings Between Line 1 and Line 2

5.7 Summary

These three case histories will be used in subsequent chapters to better understand the prediction of lateral spread displacements in subduction zones. Analysis of these sites indicated two unique prediction trends based on the type of empirical models used. Based on these trends, it was decided to separate the results of the strain-based empirical models into one chapter and the rest of the empirical models into another chapter. The results of the empirical models created by Bardet, et al. 2002, Rauch and Martin II 2000, Youd, Hansen and Bartlett 2002, and Zhang, et al. 2012 are presented in Chapter 6, while the results for the strained-based models, Faris, et al. 2006 and Zhang, Robertson and Brachman 2004, will be presented in Chapter 7. Chapter 4 describes in more detail the seismic characteristics of subduction zones and provides necessary background for Chapter 6.

6 FULLY EMPIRICAL LATERAL SPREADING MODELS

These lateral spreading models implicitly or explicitly rely on attenuation relationships between magnitude and source-to-site distances to predict the amount of energy available to drive lateral spreading. The Zhang, et al. 2012 model allows users to use any local attenuation relationship to estimate the spectral acceleration at a period of 0.5s that will occur at a site. Bardet, et al. 2002, Rauch and Martin II 2000, and Youd, Hansen and Bartlett 2002 models use magnitude and site-to-source distances to create an attenuation relationship within their equations. This chapter discusses the sensitivity of the models to seismic variables, differences in the way site-to-source distances are calculated for each model, and how well each model preformed.

6.1 Sensitivity of Variables in Empirical Equations

Chapter 4 discussed the variation found in the seismic variables reported for mega-thrust subduction earthquakes like the Maule Chile 2010 earthquake. To better understand the effect of this variation on the models, a sensitivity analysis was conducted. A sensitivity analysis shows how much the accuracy of each value affects the outcome of the overall equation. This sensitivity analysis was conducted by obtaining the best estimate for each variable and then changing a variable while the other variables are held constant to show how uncertainty in that variable affects the overall result. Figure 6-1, Figure 6-2, Figure 6-3, and Figure 6-4 are

"tornado" charts showing the sensitivity of variables in Bardet, et al. 2002, Rauch and Martin II 2000, Youd, Hansen and Bartlett 2002, and Zhang, et al. 2012 models, respectively. Highly sensitive variables are located at the top and less sensitive variables are at the bottom.

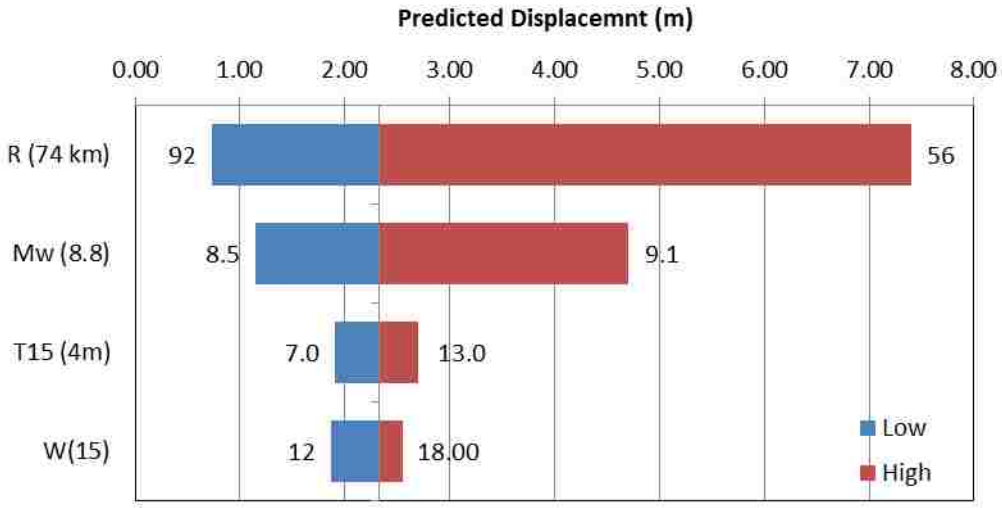

Figure 6-1: Bardet, et al. 2002 Tornado Chart

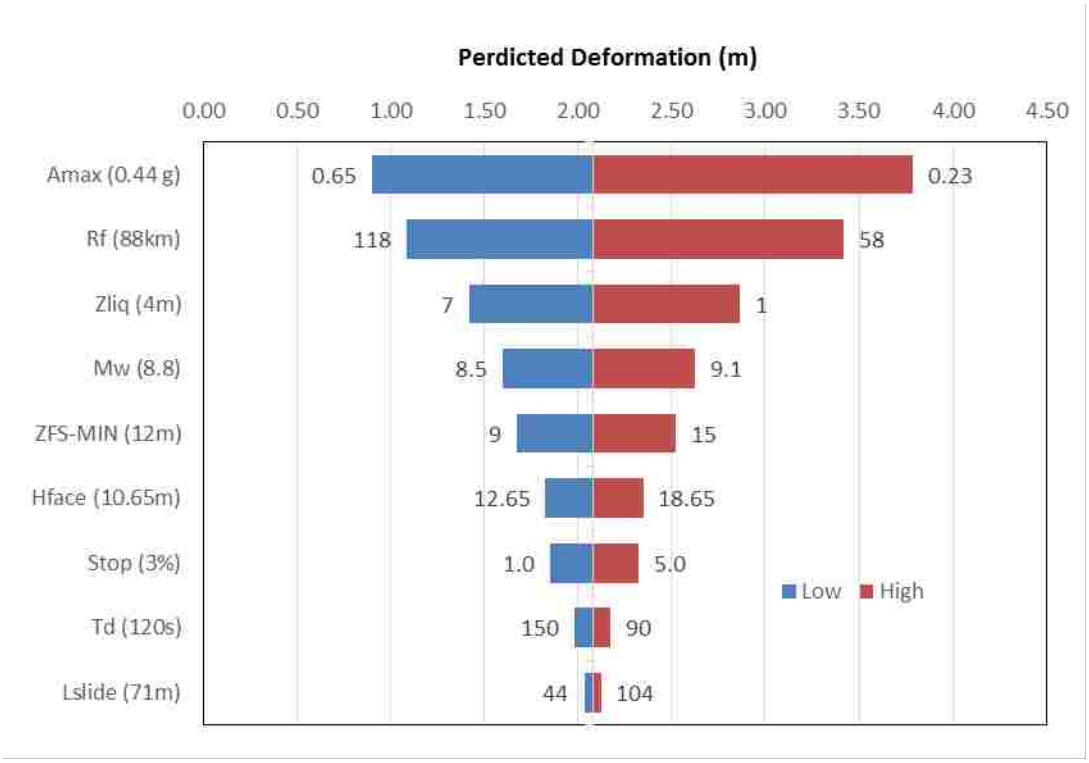

Figure 6-2: Rauch and Martin II 2000 Tornado Chart

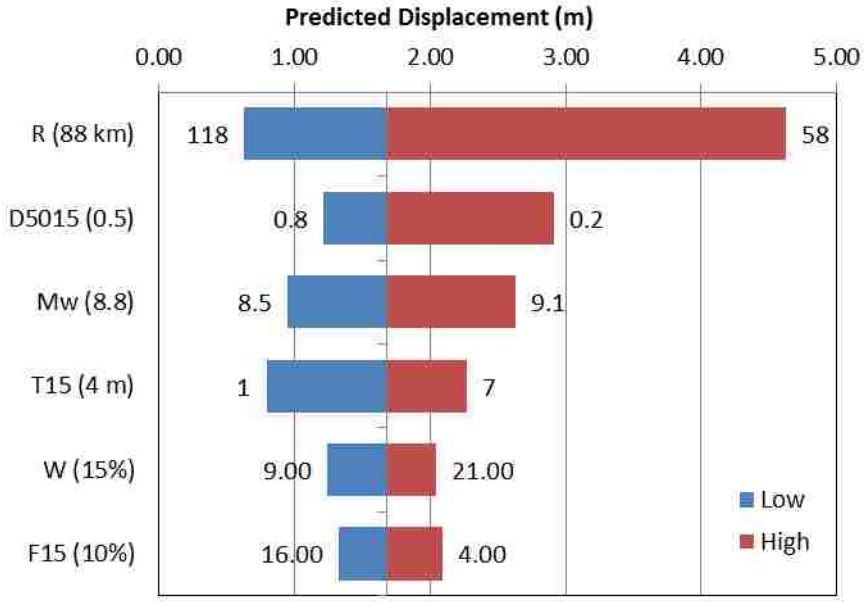

Figure 6-3: Youd, Hansen, and Bartlett 2002 Tornado Chart

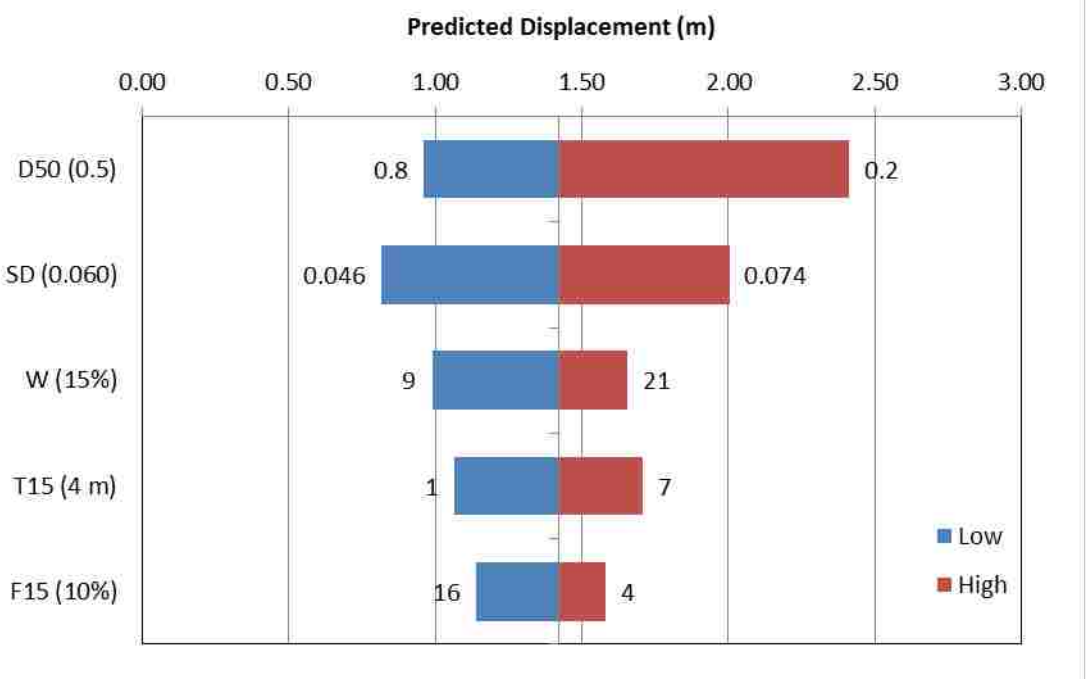

Figure 6-4: Zhang, et al. 2012 Tornado Chart

The overall trend of the graphs is that the seismic parameters, especially R, A_{max}, and SD, are at the top of the tornado chart. The moment magnitude, M_w, is slightly less sensitive than

other seismic parameters because it is known with the greatest certainty, although this parameter also has a strong influence on the computed displacement. $D50_{15}$ is also relatively influential for the Youd, Hansen and Bartlett 2002 and Zhang, et al. 2012 models. The value of $D50_{15}$ is most influential when the soil is fine sand with values close to 0.1 mm but as the soil becomes coarser this value becomes less sensitive. This is why D50 appears lopsided towards smaller values in some of the tornado charts. Since the seismic parameters R, A_{max}, and SD change the displacements calculated by the models more significantly than any other parameter, these parameters were carefully chosen. Several site-to-source distances were compared to better understand the relationship between distance and predicted displacements.

6.2 Site-to-Source Distances

Since site-to-source distances are very influential to the accuracy of these empirical models, it is important to understand the definitions of distances used in each model. Rauch and Martin II 2000 and Youd, Hansen and Bartlett 2002 define R similarly as the "shortest horizontal distance from site to surface projection of fault rupture or zone of seismic energy release" (Rauch and Martin II 2000) or "the horizontal or mapped distance from the site in question to the nearest bound of seismic energy source (Youd, Hansen and Bartlett 2002). Some confusion has existed over what the nearest bound of seismic energy source means. For strike-slip earthquakes this distance is measured to the fault because the energy is released beneath the fault as two almost vertical faults slide past each other. However, in subduction zone earthquakes the energy can be released several kilometers away from the fault surface or trench especially as the rupture surface between plates approaches horizontal. Youd, Hansen and Bartlett 2002 measured the distance to the seismic energy source for the Alaska 1964 earthquake by measuring the closest

distance to the line between the zone of uplift (red line) and zone of subsidence (blue line) as shown in Figure 6-5. This distance is significantly shorter than the distance to the Aleutian Trench causing the site-to-source distance for the Alaska case history sites to be only fifteen to thirty percent of the distance to the trench. This distance is most similar to the Boore-Joyner distance or the closest distance to the surface projection of the fault surface. Bardet, et al. 2002 defines R as the distance from the site to the epicenter. For the Alaska 1964 earthquake the epicentral distances presented in the Bardet, et al. 2002 model are 35-100 km (Bardet, et al. 2002) which agrees with the seismic energy distances reported by Bartlett and Youd but not the reported epicentral distances of 84-138 km (Bartlett and Youd 1990) as shown in Table 6-1. The cause of this discrepancy is unknown, but perhaps Bardet, et al. 2002 simply assumed the distance from Youd and Bartlett as the epicentral distance. For the Chilean attenuation used in connection with the Zhang, et al. 2012 model, the distance was derived using the closest distance to the fault rupture. These distances best represent the distances used to develop the models.

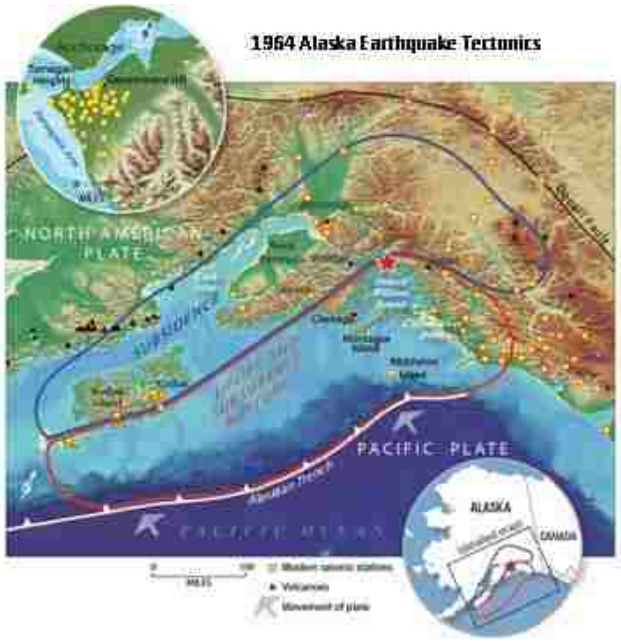

Figure 6-5: 1964 Alaska Earthquake Zone of Uplift and Subsidence (U.S. Geological Survey 2014)

Table 6-1: Distances for the Alaska 1964 Case Histories

Site	Seismic Energy Distance	Epicentral Distance	Source
Knik River	100 km	95 km	Bartlett and Youd 1990
20 mile River	60 km	84 km	Bartlett and Youd 1990
Snow River	35 km	138 km	Bartlett and Youd 1990

6.3 Results

Several distances were used in these models to represent distances likely to be used by engineers for comparison. Table 6-2 shows the three best estimates of epicenter location that were used in the Bardet, et al. 2002 equation. Asperities were not used because they were either farther away from the site than the epicenter or did not have a well-defined location. Luckily the distance to the zone of seismic energy release was easier to define. The fault rupture surface extended below the sites in all four fault rupture models giving a distance to the seismic energy source of zero. This caused large displacements to be calculated so possible alternatives were considered. The distance to maximum coastal uplift (47km) was used because it closely resembles the approach that Youd, Hansen and Bartlett 2002 used for the Alaska 1964 earthquake. The distance to the trench (160km) was used because the distance to the fault is used for strike-slip faults and occasionally in practice this distance is accidentally used for subduction zones due to confusion over the definition of the distance to the release of seismic energy. In addition, a best fit distance was found for the Youd, Hansen and Bartlett 2002 and the Rauch and Martin II 2000 models to see what values for R worked best for the sites. These distances were used to establish a clear standard for determining the site-to-source distance.

Table 6-2: Epicentral Distances used in the Bardet, et al. 2002 Equation

Source	Latitude	Longitude	Depth	Epicentral Distance
USGS-Updated	36.122 S	72.898 W	22.9 km	104 km
SSN-Updated	36.29 S	73.24 W	30.1 km	83 km
Vigny et al. 2011	36.41 S	73.18 W	26.0 km	70 km

6.3.1 Bardet, et al. 2002 Model

Figure 6-6 shows the error in the model with different epicentral distances. The distance to the epicenter from the University of Chile fit the model the better than the other epicenters with no measurements outside the 50% to 200% of the measured range. The ratios of predicted to measured displacements are shown in Table 6-3.

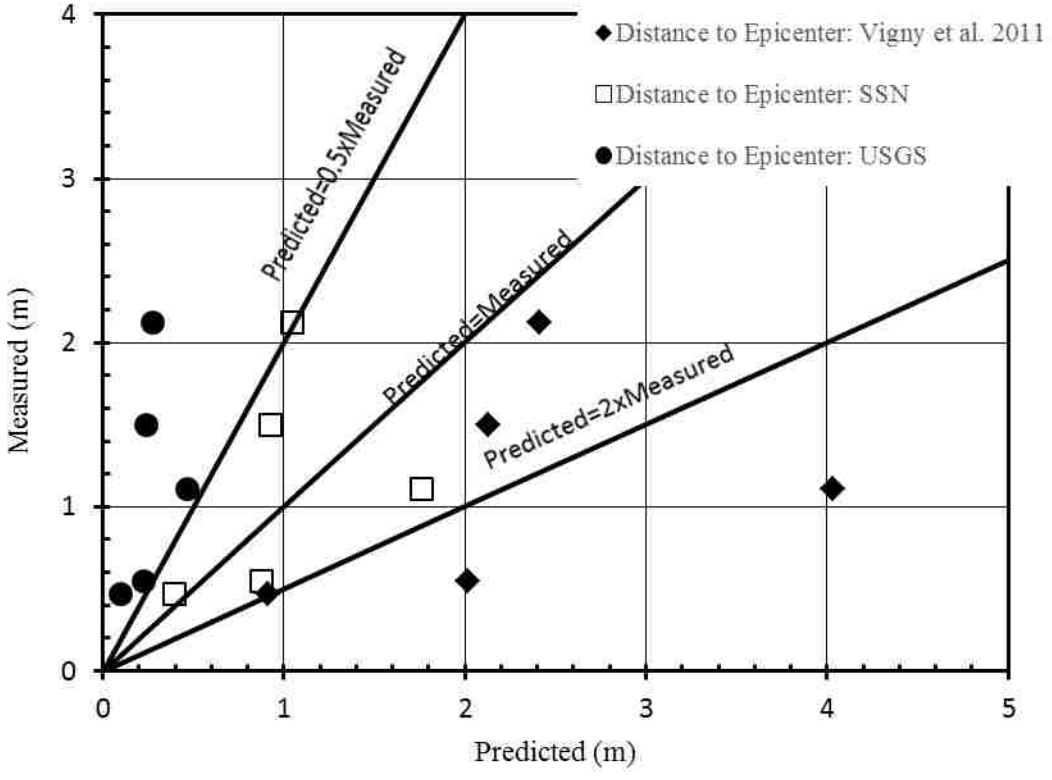

Figure 6-6: Bardet, et al. 2002 Error with Different Epicenters

Table 6-3: Predicted Verses Measured Displacements for the Bardet, et al. 2002 Model

	R (km)	W (%)	S (%)	T_{15} (m)	Predicted (m)	Measured (m)	Pred./Meas. (%)
SCP	83	12.5	--	1.4	0.39	0.47	83%
NCP-Rotation	83	18.8	--	4	0.88	0.55	160%
NCP-Pile disp. 1	83	21	--	4	0.93	1.5	62%
NCP-Pile disp. 2	83	37.3	--	3	1.05	2-2.25	47-53%
Line 1&2	83	--	3.5	10	1.76	0.99-1.23	143-186%

With this data it would seem that epicentral distance would be the best option for the Bardet, et al. 2002 model, but there a couple concerns with this approach. One concern is that different epicenters or asperities will fit better for different site locations. If our sites had been located farther north the USGS epicenter would have done far better in the models. Prior to the Maule Chile 2010 earthquake, an attenuation developed by Sargoni, et al. 2004 was used frequently in practice in Chile. However, the accelerations predicted by the model, using hypocentral distances, did not fit the accelerations measured during the Maule Chile 2010 well. Following Maule Chile 2010 earthquake, the attenuation equation was changed to use the distance to the closest asperity or hypocenter (C. Ledezma, personal communication, December 14, 2011). This may work well to estimate accelerations that occurred at a site during a past earthquake but it is generally difficult to determine the location of an epicenter let alone multiple asperities for future earthquakes. While this approach may work theoretically, the difficulty of predicting the location of future asperities could keep engineers from using these models for large magnitude earthquakes.

The second concern preventing this method from being used in practice is that this distance may not work for other subduction zones. In the Alaska 1964 earthquake, the case history site on the Snow River was the closest to the fault rupture zone (35 km) but the farthest from the epicenter (138 km) when compared to the other case histories (Bartlett and Youd 1990).

The error for the Alaska 1964 case histories with the seismic energy distance (Figure 6-7) is smaller than the error with the epicentral distance (Figure 6-8). For these reasons, an epicentral distance is impractical for megathrust subduction zone earthquakes.

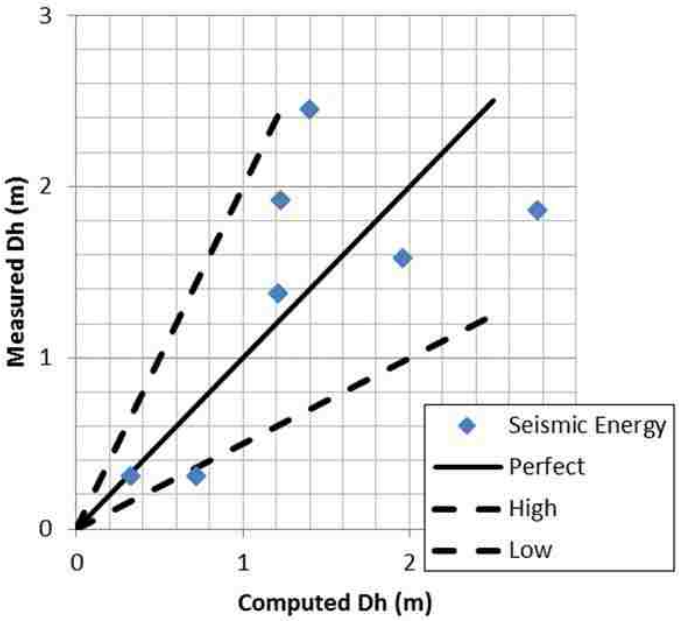

Figure 6-7: Alaska 1964 Case Histories with Boore-Joyner Distance

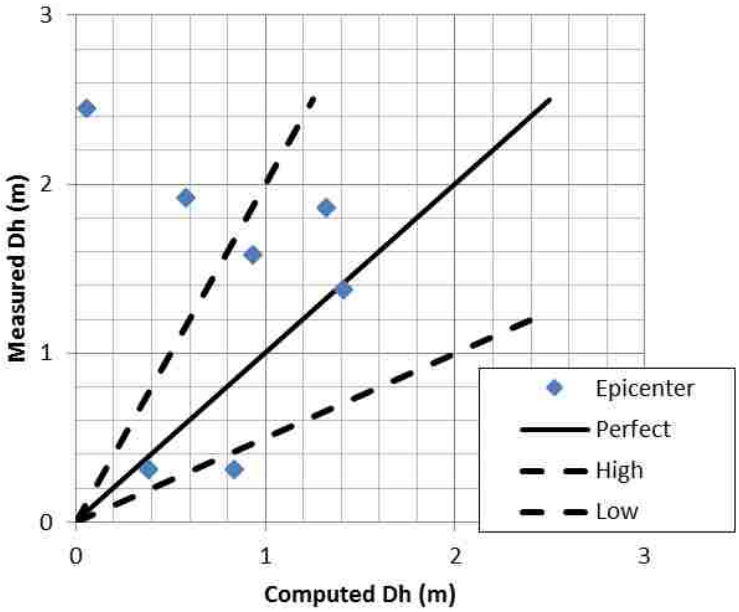

Figure 6-8: Alaska 1964 Case Histories with Epicentral Distance

6.3.2 Rauch and Martin II 2000 Model

Only three points representing the North Coronel Pier, South Coronel Pier, and lateral displacements between piers are used in the Rauch and Martin II 2000 model because it calculates one average displacement per lateral spread feature. The Rauch and Martin II 2000 paper does not describe in detail how displacements were averaged when creating the model. There were multiple ways to calculate the average displacement at the North Coronel Pier. An average of 1.40 meters was calculated for the North Coronel Pier by using the ground displacements from the largest pile rotation and the two displaced piles. The point for the North Coronel Pier has error bars showing the minimum and maximum displacement at the site as shown in Figure 6-9. The average displacements for the three sites fell within the prediction range when R was between 55 and 60% of the distance to the trench. However this percentage only applies to the Maule Chile 2010 case histories because this did not fit the Alaska 1964 case histories well as shown in Figure 6-10.

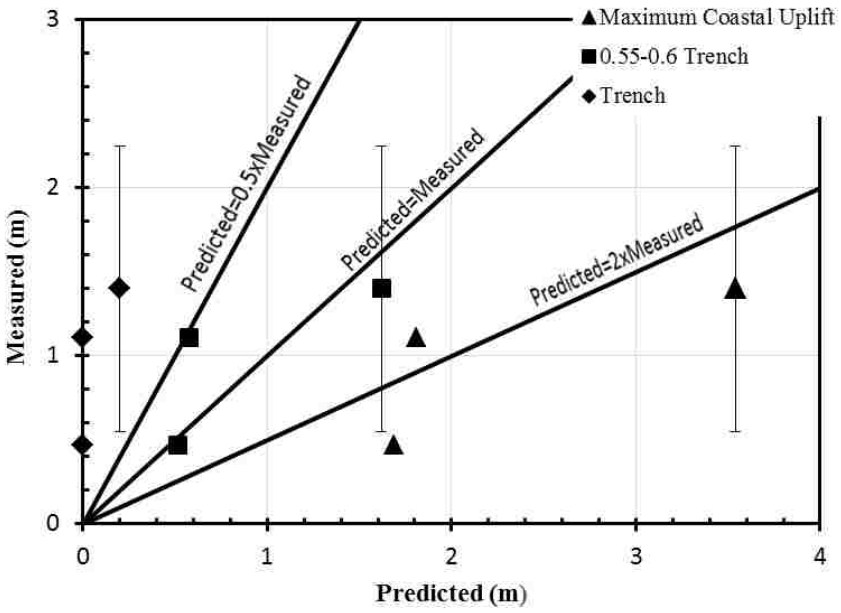

Figure 6-9: Rauch and Martin II 2000 Error with Different Distances

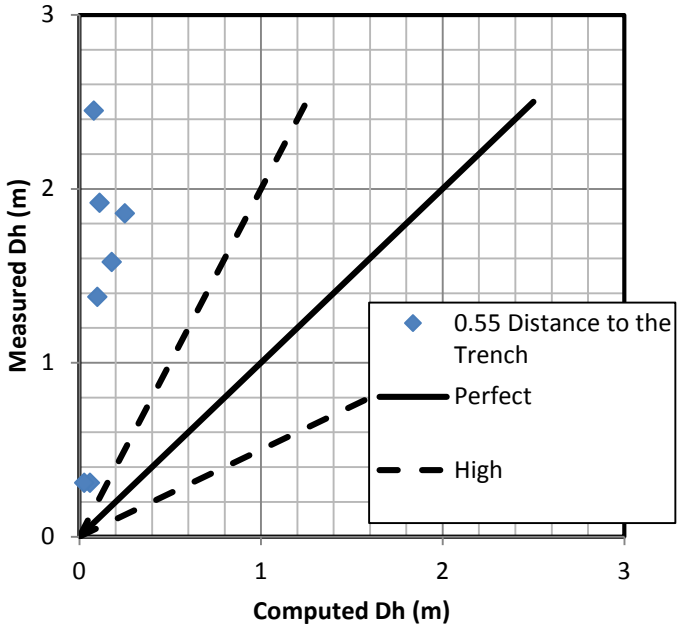

Figure 6-10: Alaska Data with 55 Percent of the Distance to the Trench

Another challenging part of the Rauch and Martin II 2000 model is the parameters Z_{liq} and Z_{FSmin}. These parameters replace the T_{15} layer by defining the depth to the top of the liquefied soil and the depth to the minimum factor of safety. For Line 1 & 2 the depth to the minimum factor of safety against liquefaction (Cetin, et al. 2004 = 0.16, Idriss and Boulanger 2004 = 0.25, and Youd, et al. 2001 = 0.22) was found at a depth of 8 meters as shown in Table 6-4. This is a shallow depth for a site with a 10 meter thick T_{15} layer that extends to a depth of 16 meters. The second smallest factor of safety against liquefaction (Cetin, et al. 2004 = 0.18, Idriss and Boulanger 2004 = 0.24, and Youd, et al. 2001 = 0.24) was located at a depth of 14 meters both matching the T_{15} layer more accurately and predicting a displacement of 1.10 meters which is almost exactly the average of the displacements at Line 1 and 2. Many different factors, such as fines content, can tip the scales between two similar layers for the lowest factor of safety.

In this example using the second smallest factor of safety changed the predicted displacement by 0.5 meters. This parameter has the potential to be variable.

Table 6-4: Predicted Verses Measured Displacements for the Rauch and Martin II 2000 Model

	H (m)	L (m)	S (%)	Z_{liq} (m)	Z_{FSmin} (m)	Predicted (m)	Measured (m)	Pred./Meas. (%)
SCP	8.45	67.5	--	5.5	7.75	0.64	0.47	137%
NCP-Rotation	13.25	70.4	--	4	14	1.66	1.4	119%
Line 1&2	--	--	3.5	4	8	0.59	1.11	53%

6.3.3 Youd, Hansen and Bartlett 2002 Model

Figure 6-11 shows the error in the Youd, Hansen and Bartlett 2002 model with different site-to-source distances. The distance equal to 65 to 70% of the distance to the trench best fit this model. Table 6-5 show the relationship between the measured and predicted displacements at the different sites.

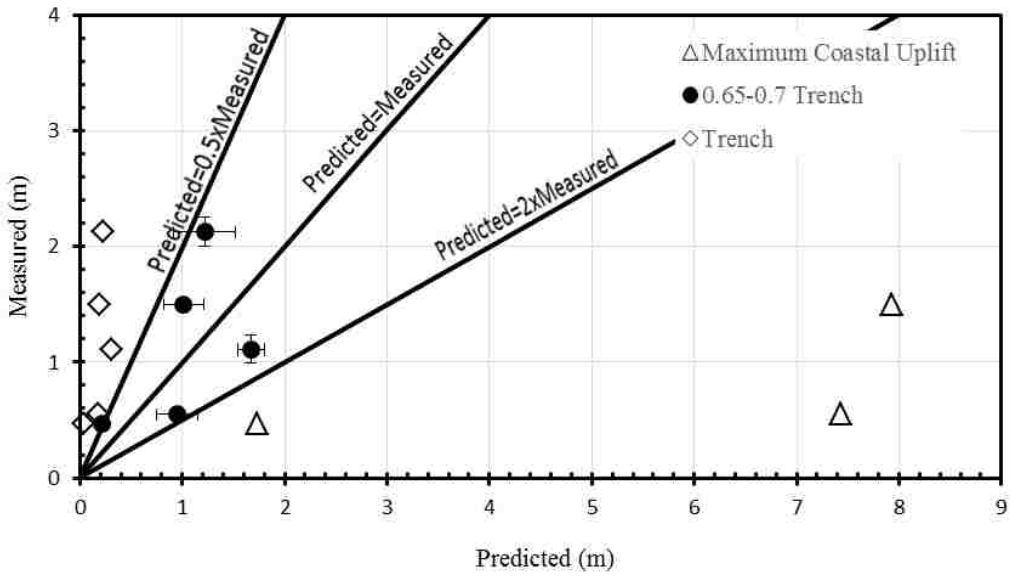

Figure 6-11: Youd, Hansen, and Bartlett 2002 Error with Different Distances

Table 6-5: Predicted Verses Measured Displacements for the Youd, Hansen and Bartlett 2002 Model

	R (km)	W (%)	S (%)	T_{15} (m)	F_{15} (m)	$D50_{15}$	Predicted (m)	Measured (m)	Pred./Meas.
SCP	92	12.5	--	1.4	43	0.1	0.22	0.47	47%
NCP-Rotation	92	18.8	--	4	11	0.5	0.95	0.55	173%
NCP-Pile disp. 1	92	21	--	4	11	0.5	1.01	1.5	68%
NCP-Pile disp. 2	92	37.3	--	3	11	0.5	1.22	2-2.25	54-61%
Line 1&2	92	--	3.5	10	4.8	0.5	1.67	0.99-1.23	136-169%

6.3.4 Zhang, et al. 2012

The Zhang, et al. 2012 model predicted the ground displacements at the North and South Coronel Pier site reasonably well with the Conteras and Boroschek 2012 local attenuation relationship but overpredicted the displacements for the survey lines as shown in Figure 6-12 and Table 6-6. Possible explanations for the over prediction is the use of an attenuation relationship and a lack of fines content data for the site where the survey lines were taken.

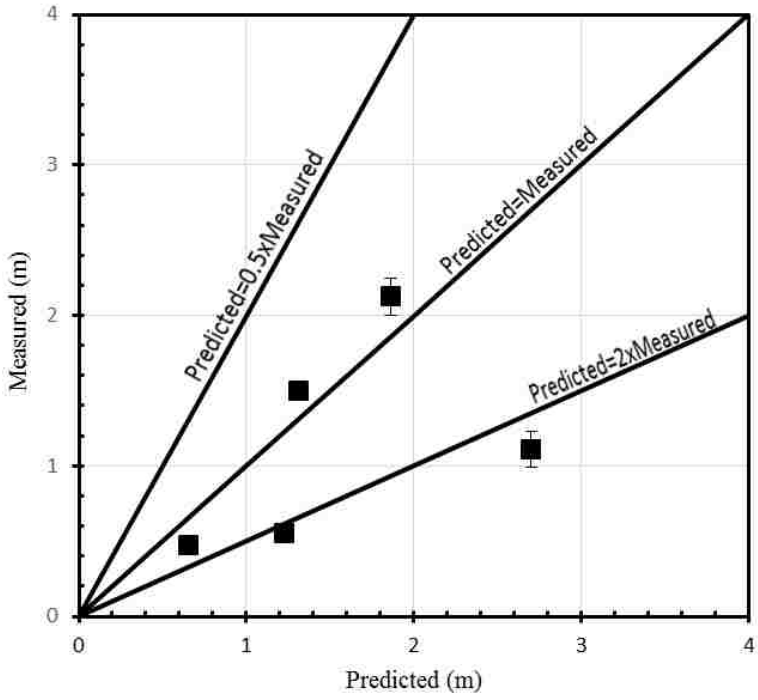

Figure 6-12: Zhang, et al. 2012 Error Chart with the Contreras and Boroschek 2012 Attenuation Model

Table 6-6: Predicted Verses Measured Displacements for the Zhang, et al. 2012 Model

	W (%)	S (%)	T_{15} (m)	F_{15} (m)	$D50_{15}$	Predicted (m)	Measured (m)	Pred./Meas. (%)
SCP	12.5	--	1.4	43	0.1	0.65	0.47	139%
NCP-Rotation	18.8	--	4	11	0.5	1.23	0.55	224%
NCP-Pile disp. 1	21	--	4	11	0.5	1.31	1.5	88%
NCP-Pile disp. 2	37.3	--	3	11	0.5	1.86	2-2.25	83-93%
Line 1&2	--	3.5	10	4.8	0.5	2.70	0.99-1.23	220-273%

As discussed previously in Chapter 4, the bilateral movement of the Maule Chile 2010 fault rupture zone caused different accelerations in the northern and southern portion of the rupture zone. Attenuation relationships predict an average acceleration based on the available case history strong motion data and the southern strong motion data was below average for the Maule Chile 2010 case history. Since these sites are in the southern portion of the rupture area, it is likely that the average spectral acceleration, at a period of 0.5s, predicted by the Conteras and Boroschek 2012 for these sites is high. A comparison between the predicted PGA for the sites of 0.44g and the measured PGA, at the closest ground motion station to the sites, of 0.4g support this hypothesis. The fines content for this site came from CPT correlations for fines content. Comparison between the SPT soil samples and the CPT predictions at the North Coronel Pier Site indicated that the CPT correlated fines contents were slightly low for that site. With a lower acceleration and higher fines content, the error would have been reduced and the site may have fit into the range.

The Conteras and Boroschek 2012 attenuation relationship was chosen as the primary attenuation model in the Zhang, et al. 2012 model for the Maule Chile 2010 earthquake for several reasons. The Conteras and Boroschek 2012 relationship was chosen because it was developed for the Chilean seismic region using accelerations from several Chilean earthquakes, the model contained data from a magnitude 8.8 earthquake (the Maule Chile 2010 earthquake),

the model was designed for interface earthquakes, and the model included an attenuation relationship for spectral accelerations at a period of 0.5 seconds. Other local Chilean attenuation relationships existed but many of them did not include relationships for determining spectral accelerations at a period of 0.5 seconds. Global attenuation relationships for subduction zones are also an option and will be discussed subsequently.

When Zhang, et al. 2012 model was developed, the Youngs, et al. 1997, a model developed for subduction zones throughout the world, was used for all subduction zone earthquakes located outside of Japan including the Alaska 1964 earthquake. The Youngs, et al. 1997 model was applied to the Maule Chile 2010 case histories to see how well the attenuation model worked for these case histories as shown in Figure 6-13. The accelearations were lower with the Youngs, et al. 1997 model with a peak ground acceleration of 0.33g. However, the majority of the sites fell within the prediction range with only the maximum displacement at the north pier falling out of the prediction bounds.

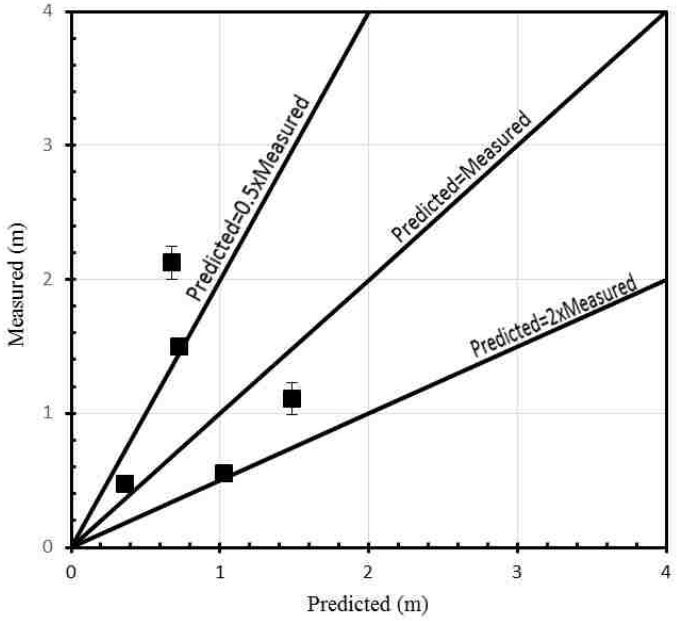

Figure 6-13: Chile Case Histories with the Youngs, et al. 1997 Attenuation Model

Zhang, et al. 2012 chose to use the 1.0 second period in the Youngs, et al. 1997 model for the Alaska 1964 earthquake because that period gave a more unbiased relationship between distance and magnitude. With a period of 1.0 second, the Youngs, et al. 1997 does not fit the Maule Chile case histories as well as shown in Figure 6-14. The Alaska 1964 case histories were not included in the dataset for the Zhang, et al. 2012 because the Youngs, et al. 1997 model did not fit well with pseudo spectral displacement calculated at a period of 0.5 or 1.0 seconds as shown in Figure 6-14 and Figure 6-15. The largest magnitude included in the development of the Youngs, et al. 1997 model was 8.2. The model was developed for subduction zone earthquakes but did not include case histories from large magnitudes so it is not surprising that the data did not fit well. However, it was one of the few models developed to predict accelerations for subduction zones on a global scale.

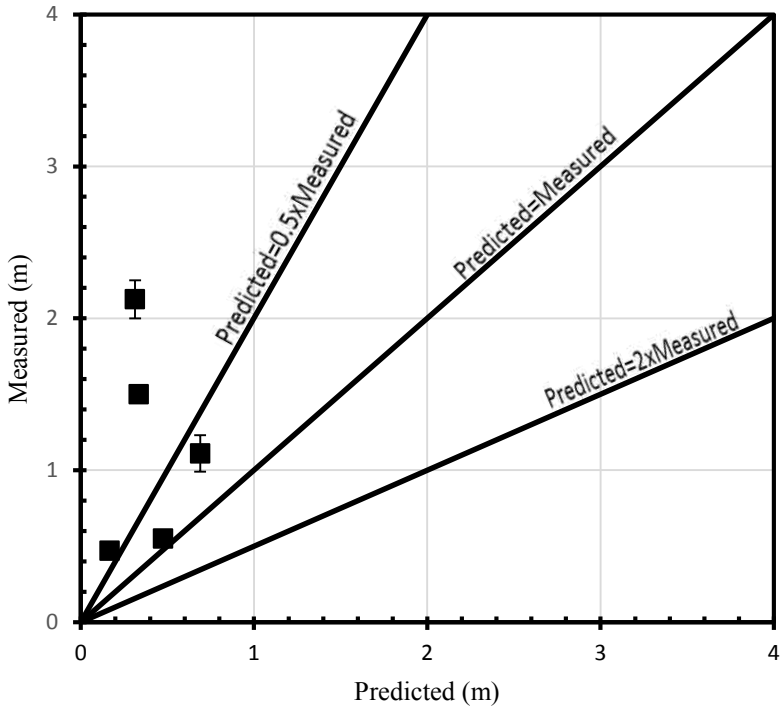

Figure 6-14: Maule Chile 2010 with Youngs, et al. 1997 at a Period of 1.0 seconds

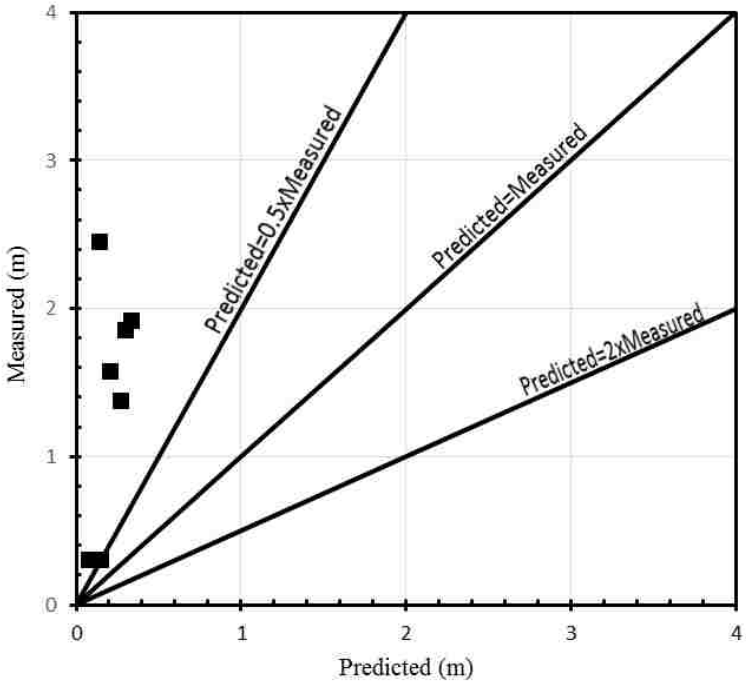

Figure 6-15: Alaska 1964 Earthquake with Youngs, et al. 1997 at a Period of 0.5s

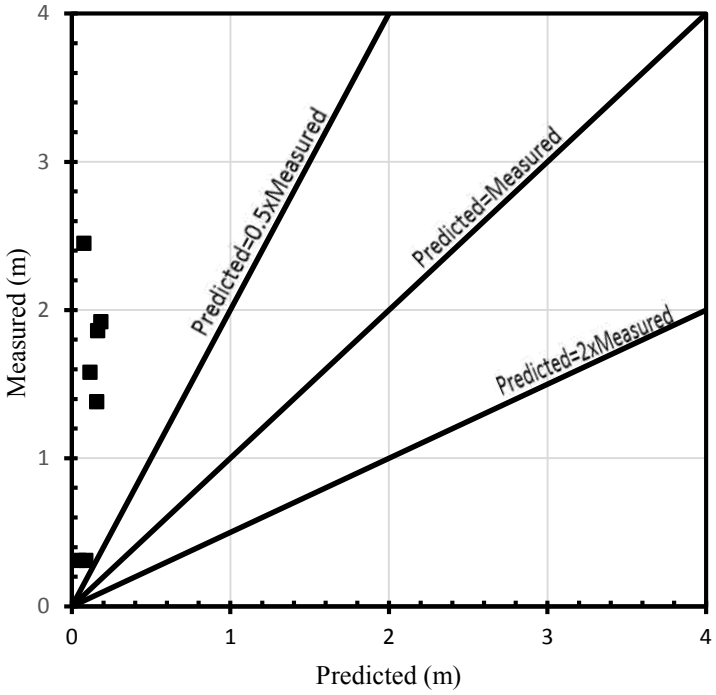

Figure 6-16: Alaska 1964 Earthquake with Youngs, et al. 1997 at a Period of 1.0s

Other attenuation relationships exist that are developed for interface subduction zone earthquakes but are tied to a specific region such as Zhao, et al. 2006 for Japan and Conteras and Boroschek 2012 for Chile. The Conteras and Boroschek 2012 equations fit the Alaska 1964 case histories better than the Youngs, et al. 1997, as shown in Figure 6-17, but still did not fit the data well. With the Conteras and Boroschek 2012 relationship, the three displacements measured on the Knik River fell withing the prediction range. However, the Twentymile River and Snow River sites, closer to the fault rupture, were underpredicted by the attenuation. By having an attenuation that included accelerations from a large magnitude earthquake, larger accelerations were predicted for the Alaska sites. However, the relationship between distance and acceleration is different for Chile than Alaska so the relationship fit some sites better than others.

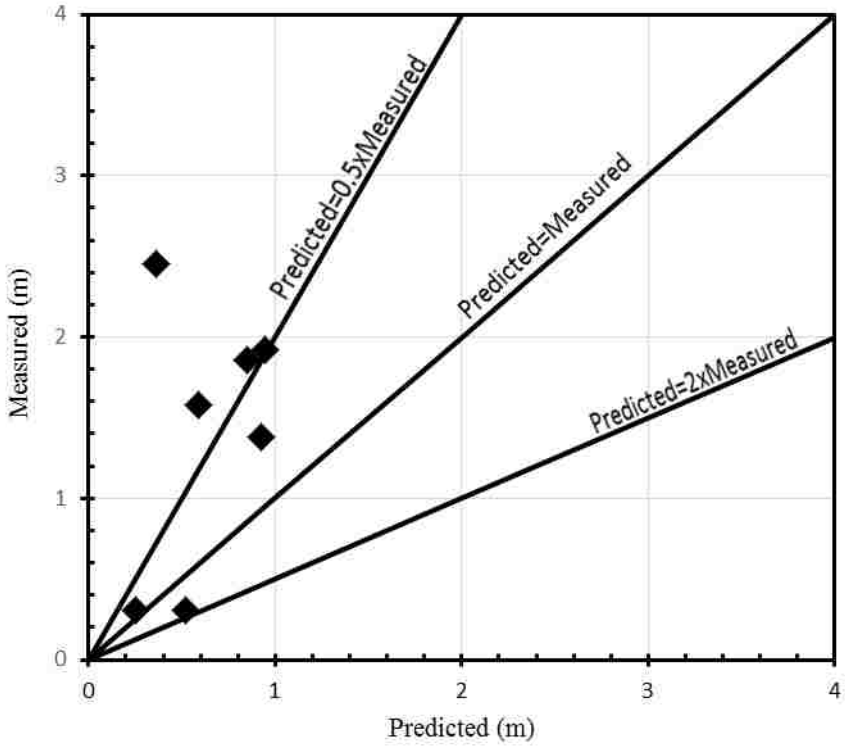

Figure 6-17: Alaska 1964 Case Histories with the Conteras and Boroschek 2012 Attenuation

The use of attenuation relationships has allowed this model to more easily be applied to countries outside of the Western United States and Japan. Moving away from an internal site-to-source distance opens up the possibility of a lateral spread model applicable to all seismic regions and faulting mechanisms. However, global attenuations for large magnitude interface subduction zone earthquakes are just starting to be developed as researchers come together to build a global probabilistic seismic hazard map. Without such a global attenuation, it was not possible to verify whether the Zhang, et al. 2012 model works with the Alaska 1964 case histories. It also creates a challenge for engineers in the field to confidently pick a relationship that will work for large magnitude earthquakes.

6.4 Summary

Even with the differences between the Bardet, et al. 2002, Rauch and Martin II 2000, and Youd, Hansen and Bartlett models, similar site-to-source distances were needed for all three models to fit in the prediction range of fifty percent of the measured value to twice the measured value. The Bardet, et al. 2002 model best fit the case histories with the epicentral distance of 83 kilometers, based on the epicentral location recommended by the University of Chile. The Rauch and Martin II 2000 and Youd, Hansen and Bartlett 2002 models best fit the case histories with distances between 88 and 112 kilometers or fifty-five to seventy percent of the distance to the trench. The Conteras and Boroschek 2012 attenuation seemed to fit the Zhang, et al. 2012 model very well for the Chile sites with only the displacements between the piers being overpredicted.

Several important lessons can be learned from the distances used in the Youd, Hansen and Bartlett 2002 and Rauch and Martin II 2000 models. First, using the distance from the site to the day-lighting of the fault can greatly underpredict lateral spread displacements for a

subduction type source. For the Maule Chile 2010 case histories, the best-fit distance was between fifty-five and seventy percent of the fault rupture distance. However, this distance underpredicted the displacements for the Alaska 1964 earthquake where the ratio was between fifteen and thirty percent for the site. There are significant differences between the Alaska and Chile seismic zone. The trench and fault rupture zone was at least twice as far away from the sites in Alaska than Chile. This caused the epicentral distance to be too large in Alaska and the fault rupture distance to be too small in Chile for accurate predictions with the respective site-to-source distance. There are several barriers to finding a site-to-source distance that can work for multiple countries and faulting mechanisms that keep these models from being accurate for all megathrust subduction earthquakes.

Models that rely on one source-to-site distance to characterize earthquakes are difficult to extend to countries and subduction zones not included in the case histories. Finding a way to measure R that will work for a variety of subduction zones and with the R's already in the models from strike-slip faults is a major challenge. The Bardet, et al. 2002, Rauch and Martin II 2000, and Youd, et al. 2002 models have made a significant contribution to our understanding of lateral spreading but they will be most accurate when used in the same seismic areas as the case histories used to develop them. There are significant barriers to their use for large magnitude earthquakes outside of the Alaska subduction zone, and perhaps there as well. By using local attenuation relationships, the Zhang, et al. 2012 model attempts to overcome these barriers of different regions and faulting mechanisms. However, limitations in current attenuation relationships can make it difficult to find an attenuation that will work both in the region and with large magnitude interface earthquakes.

7 STRAIN-BASED LATERAL SPREADING MODELS

7.1 Results

As discussed in Chapter 3, both the Faris, et al. 2006 and Zhang, Robertson and Brachman 2004 models used lab strain data to develop a relationship between SPT blow count and lateral displacement. Since these models do not have a cut-off for SPT blow counts, the South Pier case history could be used for these models without an energy measurement correction. Both models were developed using the maximum displacement measured on a lateral spread feature, so the computed displacements are compared with the maximum displacement measured at each site. The liquefaction analysis was performed for a magnitude 8.8 earthquake with a peak ground acceleration of 0.44g. Faris, et al. 2006 uses the liquefaction analysis developed by Cetin, et al. 2004, while Zhang, Robertson and Brachman 2004 uses the liquefaction analysis developed by Youd, et al. 2001. All calculations were stopped at a depth of 16 meters because the layers below this depth had high fines content and were not likely to contribute to lateral spreading. This was also done to prevent differences in the displacements calculated by the models due to including thin layers of soils with lower fines that were found in the CPT but not the SPT test results. The displacements for the Zhang, Robertson and Brachman 2004 model were calculated by the CPT analysis program within Cliq (Geologismiki, Gregg Drilling, and Robertson 2006) which uses this approach. Comparisons of the maximum measured lateral spread displacements

and the computed displacements using the Faris, et al. 2006 and Zhang, Robertson and Brachman 2004 models are shown in Figure 7-1 and Figure 7-2, respectively.

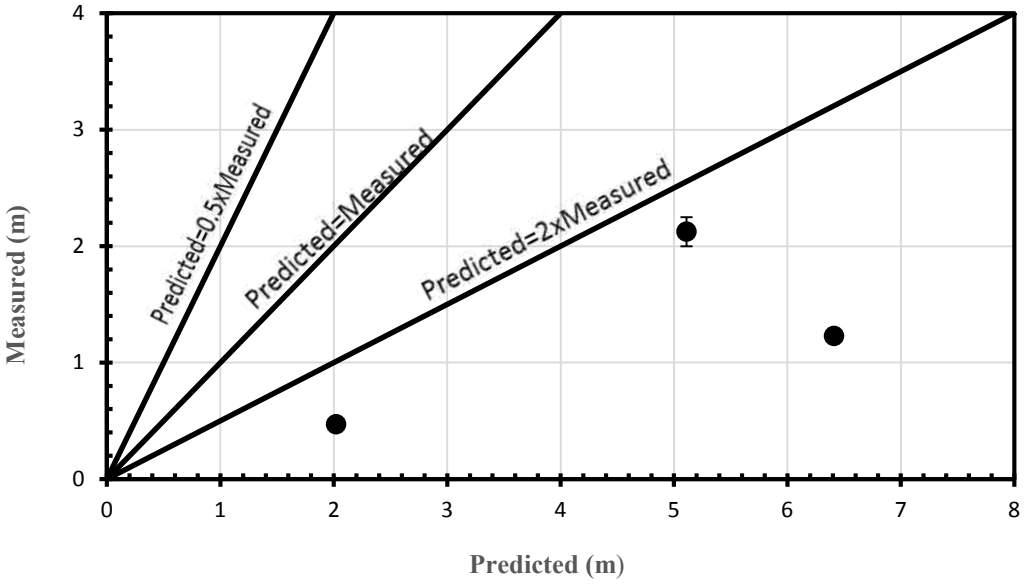

Figure 7-1: Zhang, Robertson and Brachman 2004 Error Chart with CPT data

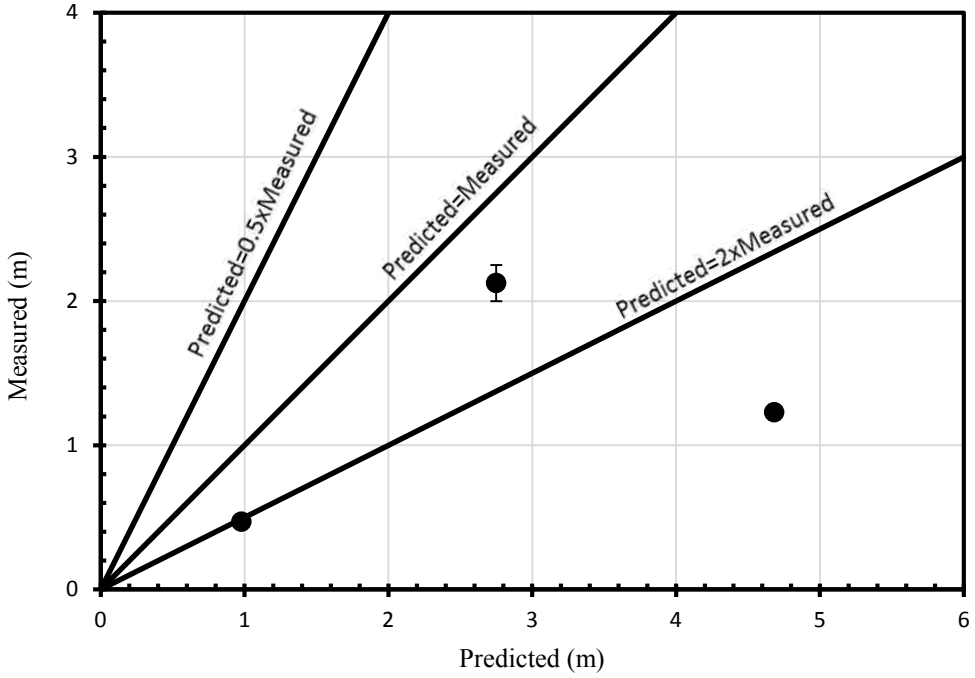

Figure 7-2: Faris, et al. 2006 Error Chart

The Zhang, Robertson and Brachman 2004 model overpredicted the maximum displacement measured at all three sites. The displacement at the sheet pile wall between the two piers is significantly out of the prediction range for both models. The Zhang, Robertson and Brachman 2004 model overpredicted the measured displacement by 732%, while the Faris model overpredicted by 380%. This site had a very thick layer of liquefiable soils with low blow counts which could have contributed to the overprediction. The combination of loose soil and high shear stresses is difficult to replicate in laboratory tests because of limitations in the equipment and test set up. However, the models also overpredicted the displacements for the north and south piers which had higher blow counts and were better represented in the laboratory results. As mentioned earlier in the paper, the attenuation may have slightly overpredicted the accelerations that were experienced at the site but even with a lower peak ground acceleration of 0.4 g the displacements did not significantly decrease as shown in Table 7-1.

Table 7-1: Effects of PGA on Predicted Displacements

	Faris et al (2006)				Zhang &Robertson (2004)				Measured
PGA	0.4g		0.44g		0.4g		0.44g		
Site	Disp. (m)	Predicted/ Measured (%)	Disp. (m)	Predicted/ Measured (%)	Disp. (m)	Predicted/ Measured (%)	Disp. (m)	Predicted/ Measured (%)	
Wall	4.48	364	4.68	380	6.35	516	6.41	521	1.23m
North	2.57	114-129	2.73	121-137	5.10	227-255	5.11	227-256	2-2.25m
South	0.93	198	0.98	209	1.93	411	2.02	430	0.47m

7.2 Zhang, Robertson and Brachman 2004 Model with SPT Data

The displacements predicted by the Zhang, Robertson and Brachman 2004 model with CPT data were almost twice as large as the displacements predicted by Faris, et al. 2006 model with SPT data. This is especially significant because the Faris, et al. 2006 model overpredicted

the maximum displacement at two-thirds of sites by at least a factor of two. To account for differences between test data and possible error in the correlations between CPT and SPT tests used to develop the model, the displacements for the Zhang, Robertson and Brachman 2004 model were recalculated using the same SPT tests as the Faris, et al. 2006 model. The values were more similar between the Faris, et al. 2006 and Zhang, Robertson and Brachman 2004 model when SPT data was used as shown in Figure 7-3 and Table 7-2.

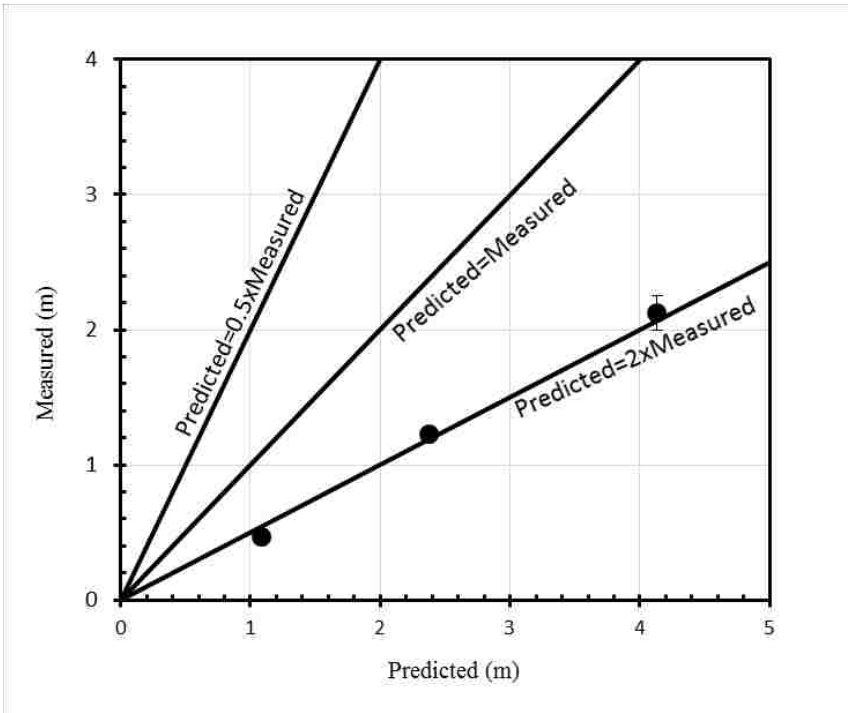

Figure 7-3: Error in Zhang, Brachman and Robertson 2004 model with SPT data

Table 7-2: Predicted Displacements with SPT Data

	Faris, et al. 2006		Zhang, Robertson and Brachman 2004 SPT Method		Measured
Site	Disp. (m)	Predicted/ Measured (%)	Disp. (m)	Predicted/ Measured (%)	
Line 1&2	4.68	380	2.38	193	1.93m
North	2.73	121-137	4.13	184-206	2-2.25m
South	0.98	209	1.09	232	0.47m

Multiple reasons exist for the differences between the displacements calculated by the Zhang, Robertson and Brachman 2004 model using CPT and SPT data. One contributor is the correlation between cone tip resistance and relative density of Tatsuoka, et al. 1990 used in the model for the CPT tests that "provides slightly smaller and more conservative estimates of relative density than the correlation by Jamiolkowski et al. when q_{c1n} is less than about 100" (Zhang, Robertson and Brachman 2004). When a conservative value is used in a calculation every 5 centimeters for 10 to 12 meters the extra displacement will add up. There are other CPT correlations for variables such as fines content that gave values lower than those observed in the SPT tests. With multiple variables it is difficult to know exactly why the tests are different. Currently, SPT tests have an advantage over CPT tests in the development of lateral spreading prediction models because more SPT tests than CPT tests exist for current lateral spreading case history sites.

7.3 The Overprediction of Displacements by Semi-Empirical Models

There are several sources of conservatism in the Faris, et al. 2006 and Zhang, Robertson and Brachman 2004 models that could have led the displacements to be overpredicted at the sites. Conservatism in the laboratory tests come from not fully representing the way soils strain in the field. Lateral spread displacements in the field are dependent on both the depth and thickness of the liquefiable layers. Another source of conservatism comes from researcher preferences used in the creation of the method. For example, Faris, et al. 2006 chose to use maximum displacements, only reduce strain potential for soils with high fines if the corresponding blow count was low, and calculate displacements for all liquefiable layers not just layers with SPT blow counts of fifteen or below. Zhang, Robertson & Brachman 2004 use a

similarly conservative approach except the fines are accounted for by correcting test results to an equivalent clean sand value and assuming "the effect of grain characteristics or fines on lateral spreading is similar to its effect on liquefaction triggering" (Zhang, Robertson and Brachman 2004). The effect of depth and the dilative behavior of denser liquefiable soils on strain and displacements will be discussed further in this chapter.

7.3.1 Modeling the Effects of Depth

The cyclic simple shear tests used in these models simulated the effect of earthquake forces on soil samples but were not set up to show the effects of depth or thickness. For example, the Faris, et al 2006 and Zhang, Robertson and Brachman 2004 models currently have a one to one relationship between displacement and thickness. For a very uniform profile in SPT blow count, fines content, and cyclic shear stress, each layer will contribute to the displacement equally. However, in completely empirical equations like Youd, Hansen and Bartlett 2002, Rauch and Martin II 2000, Bardet, et al. 2002, or Zhang, et al. 2012 changing the T15 layer from 1 meter to 4 meters does not increase the displacement by a factor of four. The relationship between the T_{15} layer and displacement is logarithmic in current empirical models with a steeper slope for thinner layers and shallower slopes for thicker layers. Figure 7-4 compares the relationship between displacement and the thickness of liquefiable layers for Faris, et al. 2006 and Youd, Hansen and Bartlett 2002 using data from the lateral displacements measured between the in north and south pier in the port of Coronel. The differences in the relationship between thickness and displacement in laboratory tests and the field may come back to the mechanics of lateral spreading. Lateral spreading is defined as blocks of mostly intact soil sliding across a layer of liquefied soil. As long as there is a layer weak enough for the soil to slide on without

significant dilation, the soil on top will displace. Thicker layers of liquefiable soil indicate a more uniform weak layer and contribute to larger displacements but there may be an optimum thickness beyond which the bottom layers start to play a less significant role. Additionally, the bottom layers of a thick liquefiable soil layer will be deeper in the profile, so it will take more energy for the soil layers on top to move.

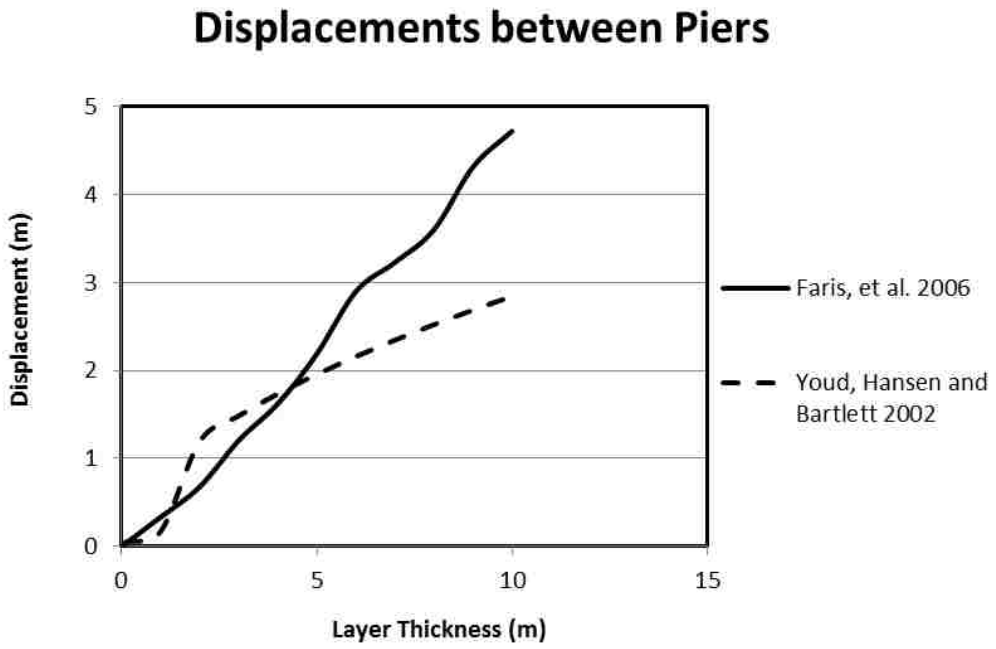

Figure 7-4: Layer Thickness Verses Displacement for Faris, et al. 2006 and Youd, Hansen and Bartlett 2002

Cliq (Geologismiki, Gregg Drilling, and Robertson 2006) has a built-in strain reduction factor that can be used with the Zhang, Robertson and Brachman 2004 model for gently sloping cases to account for the effect of depth on strain. This factor is based on Cetin, et al. 2004's strain weighting factor for volumetric strains, e_v, designed for use in estimating the settlement that will be caused by post-liquefaction pore pressure dissipation as shown in Figure 7-5. The online user manual for Cliq (Geologismiki, Gregg Drilling, and Robertson 2006) suggests using the weighting factor "if liquefaction is calculated at large depth" to prevent an excessively high

lateral displacement prediction because “the program sums up all shear strains regardless of depth” (Geologismiki 2014). This strain reduction factor significantly improved the prediction of the displacements measured between the piers, so the factor was applied to all the case histories for both models and both CPT and SPT test values. The results with strain reduction factor are shown in Figure 7-6, Figure 7-7, and Figure 7-8.

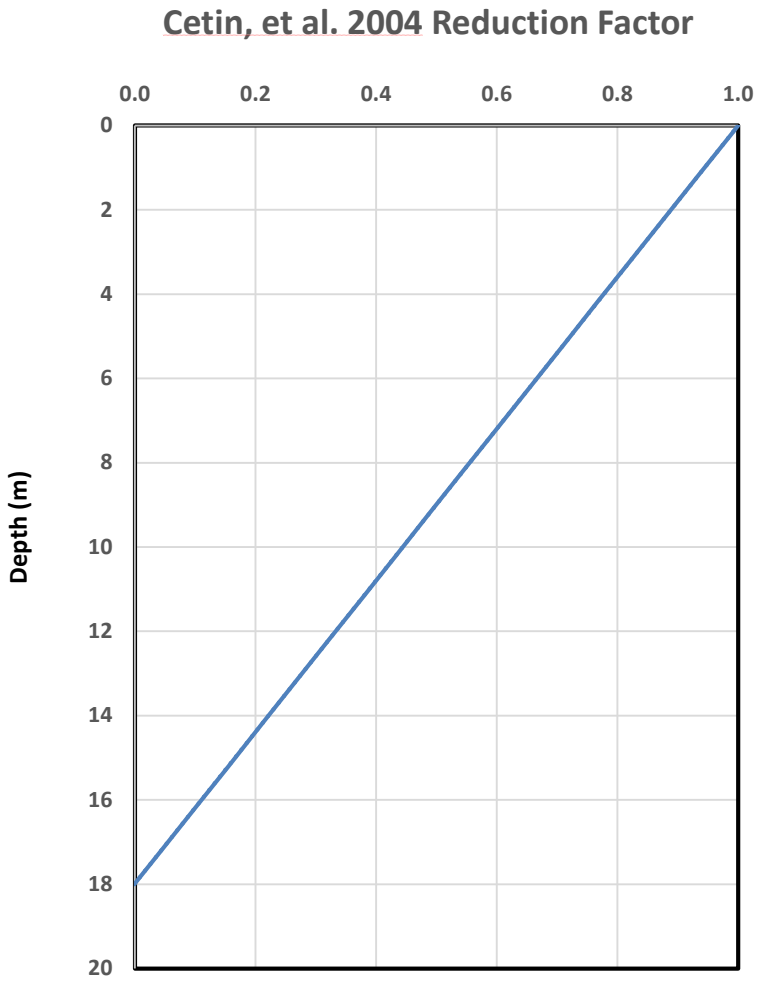

Figure 7-5: Cetin, et al. 2004 Reduction Factor

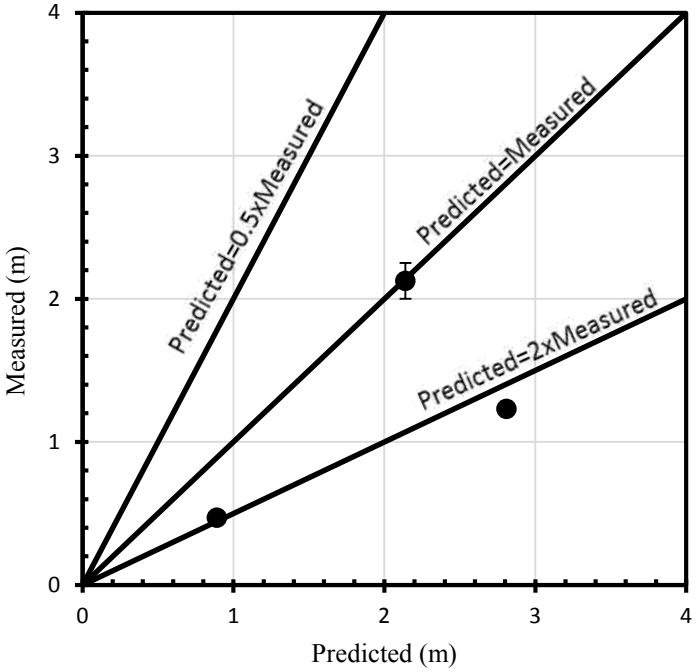

Figure 7-6: Zhang, Robertson and Brachman 2004 with CPT Data and Strain Reduction Factor

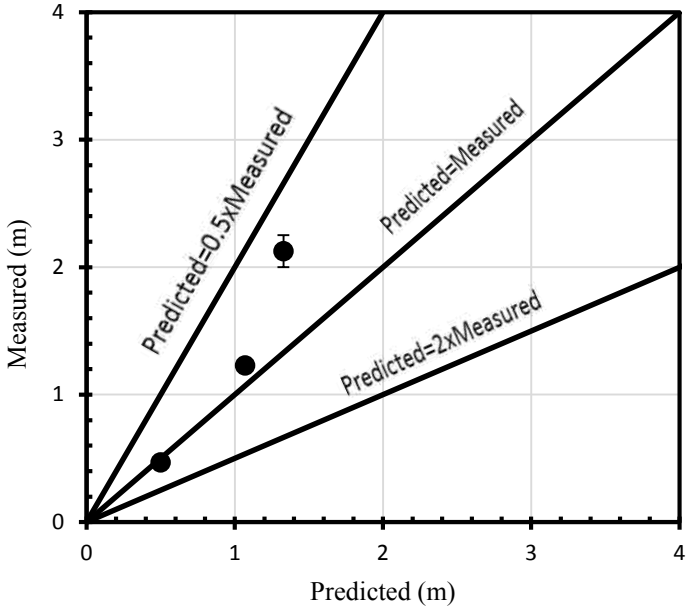

Figure 7-7: Zhang, Robertson and Brachman 2004 with SPT Data and Strain Reduction Factor

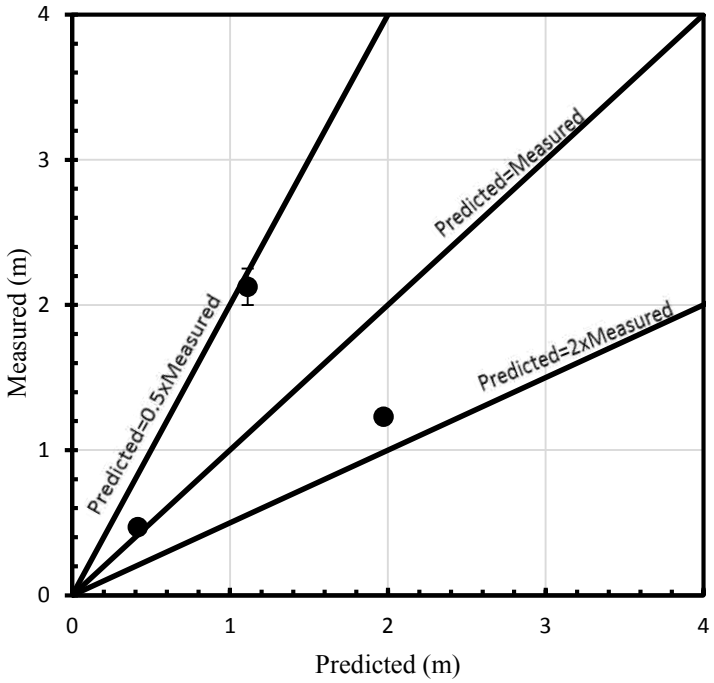

Figure 7-8: Faris, et al. 2006 with Strain Reduction Factor

7.3.2 Dilative Behavior of Soil on Strain

When Bartlett and Youd originally developed their lateral spreading model in 1995, they compared T_{10}, T_{15}, and T_{20} as variables corresponding to thickness of layers with $(N1)_{60}$ values less than or equal to 10, 15, and 20 respectively. Bartlett and Youd 1995 suggested a cut-off for lateral spreading at an SPT blow count of 15 and ultimately chose the T_{15} variable because "the compiled case-history data suggest that lateral spread is generally restricted to soil deposits having $(N1)_{60}$ values ≤ 15 for $M \geq 8$ earthquakes" (Bartlett and Youd, Empirical Prediction of Liquefaction-Induced Lateral Spread 1995). Researchers have observed that dense liquefiable layers will contract, loosing strength, and then dilate under earthquake loads until the soil returns to full strength. This behavior has been labeled as limited liquefaction and is defined separately

from liquefiable soil behavior where the soil only loses strength under earthquake loads by some researchers.

The Faris, et al. 2006 and Zhang, Robertson and Brachman 2004 models calculate strains for all liquefiable layers without a cut-off to separate out layers that display limited liquefaction behavior. Increasing the limits on SPT blow counts from 15 to 30, when there are sufficient accelerations to cause liquefaction, could cause displacements to be predicted where lateral spreading will not occur due to dilation or limited liquefaction behavior. The effect of including all liquefiable layers may have been less noticeable when these models were used for magnitude 6.0-8.0 earthquakes, but the combination of large magnitudes and peak ground accelerations inherent in the Maule Chile case histories led to liquefaction being predicted for any soil layer with a blow count less than 30. This allows a significant amount of strain to accumulate in the model especially for large magnitude earthquakes.

A cut-off based on a blow count was used to account for dilative behavior in the Faris, et al. 2006 and Zhang, Robertson, and Brachman 2004 models. Figure 7-9 and Figure 7-10 show the error in the models after the layers with blow counts greater than 15 were removed. An energy measurement of 55% was used for the SPT test at the south pier for these calculations. The previous calculations in this chapter used an assumed value of 60% to avoid introducing bias into equations that already overpredicted displacements without an energy correction. The Zhang, Robertson, and Brachman 2004 model fit within the accuracy range of the original model but the fit did not work as well for the Faris, et al. 2006 model. Little improvement was seen in the predicted displacements for Line 1 and Line 2 between the piers because the majority of $N1_{60}$ values were below 16. The use of a strain weighting factor seems better suited for reducing displacements where there are thick layers of $N1_{60}$ values less than 16. However, for the North

and South Coronel Piers removing these denser and more dilative layers caused an immediate improvement in displacement.

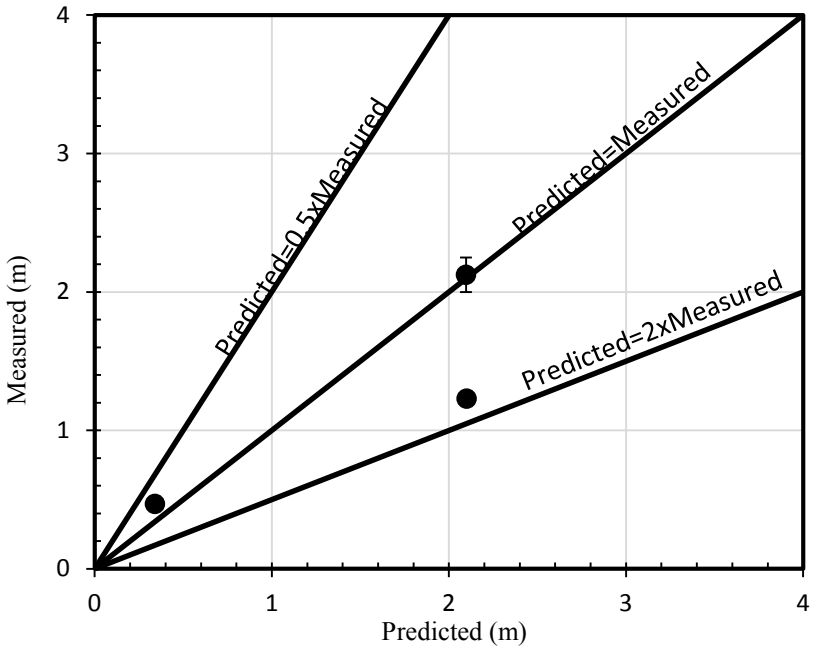

Figure 7-9: Error of Zhang, Robertson and Brachman 2004 model with $N1_{60}$<16

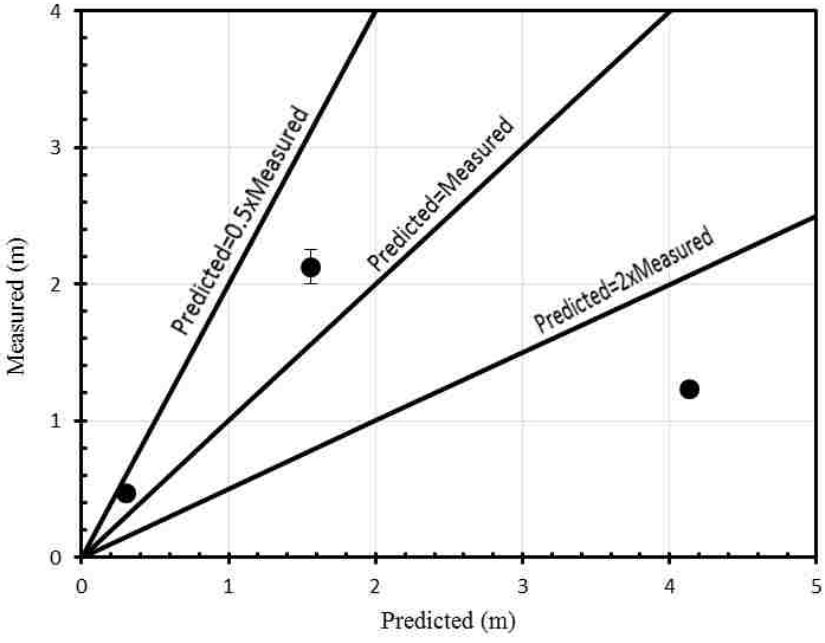

Figure 7-10: Error of Faris et al. 2006 with $N1_{60}$<16

While a cut-off of $N1_{60}$ less than or equal to 15 did not significantly improve the predicted lateral displacement at all sites, the Maule Chile 2010 case histories support the argument that compaction (or higher blow counts) makes a substantial difference in the size of lateral spread displacements. Each site experienced the essentially the same seismic forces, had a similar soil profile in terms of soil classifications and layering, and included several meters of liquefiable soils but the soil at each site was compacted to a different density. Based on geometry, the south pier experienced large gravity forces but moved the less than the other two sites because the soils were denser. Dilative behavior is an important principle to consider when evaluating the potential for lateral spreading.

7.3.3 Using Multiple Reduction Factors

Although these reduction factors work individually, they should not be combined into one calculation. The measured displacement will be underpredicted if both reduction factors are used as shown in Figure 7-11 and Figure 7-12. The best reduction factor to use is the Cetin, et al. 2004 depth reduction factor because it applies the same reduction to each site. This reduction factor is also used by the program Cliq (Geologismiki, Gregg Drilling, and Robertson 2006) to compute lateral displacements. Not calculating displacements for layers with corrected blow counts greater than 15 improved the predicted displacements for sites with several layers of liquefiable soils with blow counts greater than 15. However, the calculation is more variable between sites and does not have the same amount of verification of successful use with the Faris, et al. 2006 or Zhang, Brachman and Robertson 2004 models. Since only one reduction factor can be applied to calculations, it is recommended to use the reduction factor developed by Cetin, et al. 2004.

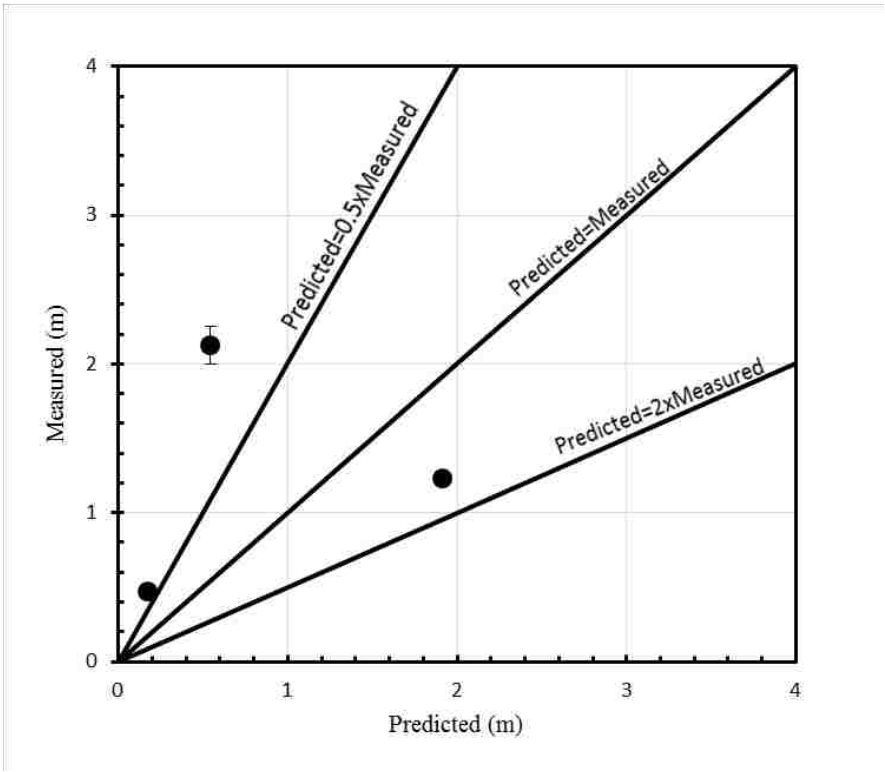

Figure 7-11: Faris, et al. 2006 with Both Reduction Factors

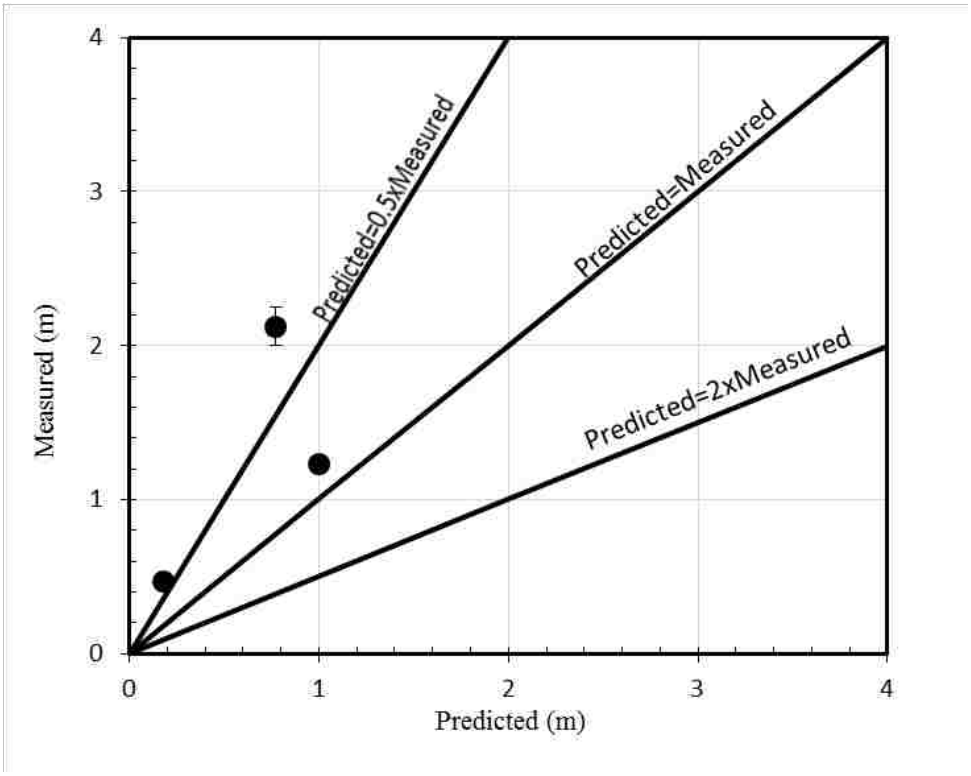

Figure 7-12: Zhang, Robertson and Brachman 2004 with Both Reduction Factors

7.4 Summary

The Faris, et al. 2006 and Zhang, Robertson and Brachman 2004 models gave conservatively large estimates of the maximum displacement measured at all three sites, especially the displacements measured between the piers. This was especially true for the Zhang, Robertson and Brachman 2004 model which over predicted one of the maximum displacements by more than a factor of four when using CPT test data. Even though the calculation of lateral displacements was limited to a depth of sixteen meters, the presence of deep liquefiable layers contributed to large predicted displacements. Significant improvement was seen in all the models, regardless of the type of field test, when the Cetin, et al. 2004 strain reduction factor was used to decrease the displacements with depth. The Cetin, et al. 2004 strain reduction factor improves the prediction of lateral spread displacements with these models by accounting for the decrease in displacements that occurs with depth. These models can be used for large magnitude earthquakes but should be used in conjunction with a strain weighting factor.

For sites with several dense liquefiable layers, like the North Coronel Pier and South Coronel Pier, not including layers with corrected blow counts greater than 15 improved the accuracy of the prediction. While using the Cetin, et al. 2004 strain reduction factor seems the best option for improving the prediction at all sites, dilative soil behavior is an important concern when using these models. Sites with dilative soils will have lower displacements and displacements calculated at sites that do not have a soil layer with $N1_{60}$ blow counts less than 16 should be viewed with some skepticism because the case histories do not contain a similar profile. An important lesson from these case histories is that increasing SPT blow count will significantly decrease lateral spreading displacements even if the soils are still susceptible to liquefaction.

8 CONCLUSIONS

1. The maximum displacement at the north pier was 2-2.25 meters, while the maximum displacement at the south pier was 0.47m. Both sites had several meters of liquefiable soil but the soils at the north pier were less dense leading to more displacement. The majority of the liquefiable layers at the south pier had correct blow counts greater than 15.
2. These case histories support the recommendation of Youd and Bartlett 1995 that only layers with $(N1)60 \leq 15$ contribute to lateral spreading. This is especially true for earthquakes with magnitudes ≤ 8.0 from which Bartlett and Youd based the recommendation (Bartlett and Youd, Empirical Prediction of Liquefaction-Induced Lateral Spread 1995).
3. Site-to-source distances are difficult to define accurately for large subduction zone earthquakes and can vary greatly between seismic regions making it difficult to recommend a method for calculating R that will preserve the model accuracy of predicting distances within 50-200% of the measured value.
4. The use of epicentral distance worked well in the Bardet, et al 2002 model for the Maule Chile 2010 case histories but not the Alaska 1964 case histories where the rupture zone is farther from the case history sites. Epicentral distance is

impractical for subduction zones because multiple epicenters and asperities exist for each event and epicenters are difficult to predict in design.

5. The Zhang, et al. 2012 model fit the Maule Chile 2010 case histories well with the Conteras and Boroschek 2012 model. Attenuation relationships that include accelerations from large magnitude earthquakes and are created for the desired seismic region can be challenging to find. This made it difficult to verify how well the Zhang, et al. 2012 model worked for the Alaska 1964 case histories. Attenuations that do not include accelerations from large magnitude earthquakes are likely to underpredict accelerations.
6. Using the distance to the trench will tend to underpredict displacements because the optimum distance for the Chile 2010 and Alaska 1964 case histories fell within 15-70% of the distance to the trench. However, using the distance to the zone of uplift as Youd suggested is too conservative for some seismic regions.
7. The Faris, et al. 2006 and Zhang, Robertson and Brachman 2004 models generally over predicted displacements by a factor of 2 without modification
8. Strain-based models overpredict because they include liquefiable layers the effect of depth on strain is not account for in the models.
9. Using the Cetin, et al. 2004 strain reduction factor with depth greatly reduced the overprediction of displacements for both the Faris, et al. 2006 and the Zhang, Robertson and Brachman 2004 models.

REFERENCES

Bardet, J., T. Tobita, N. Mace, and J. Hu. "Regional Modeling of Liquefaction Induced Ground Deformation." *Earthquake Spectra*, 2002: 19-46.

Bartlett, S. F., and L. T. Youd. "Case Histories of Lateral Spreads Caused the 1964 Alaska Earthquake." *University of Utah.* 1990. www.civil.utah.edu/~bartlett/misc /Case%20Histories%20of%20Lateral%20Spreads%20Caused%20by%20the %201964%20Alaska%20Earthquake.pdf (accessed October 20, 2014).

Bartlett, S. F., and L. T. Youd. "Empirical Prediction of Liquefaction-Induced Lateral Spread." *Journal of Geotechnical Engineering*, 1995: 316-329.

Bray, J., et al. "Effects of Ground Failure on Buildings, Ports, and Industrial Facilities." *Earthquake Spectra*, 2012: S97-S118.

Brunet, S., J. Carlos de la Llera, A. Jacobsen, E. Miranda, and C. Meza. "Performance of Port Facilities in Southern Chile during the 27 February 2010 Maule Earthquake." *Earthquake Spectra*, 2012: 553-579.

Cetin, O. K., et al. "Standard Penetration Test-Based Probabilistic and Deterministic Assesment of Seismic Soil Liquefaction Potential." *Journal of Geotechnical and Geoenvironmental Engineering*, 2004: 1314-1340.

Conteras, V., and R. Boroschek. *Strong Ground Motion Attenuation Relations for Chilean Subduction Zone Interface Earthquakes.* Santiago: 15 WCEE, 2012.

Delouis, B., J. Nocquet, and M. Vallée. "Slip distribution of the February 27,2010 Mw=8.8 Maule Earthquake, central Chile, from static and high-rate GPS, InSAR, and broadbend teleseismic data." *Geophysical Research Letters*, 2010: L17305.

Ekstrom, G., and M. Nettles. *Global CMT Project Moment Tensor Solution.* February 27, 2010. http://earthquake.usgs.gov/earthquakes/2010/us2010tfan/neic_tfan_gcmt.php (accessed October 14, 2014).

Faris, A. T. *Probabilistic Models for Engineering Assesment of Liquefaction-Induced Lateral Spreading Displacements.* PhD Dissertation, Berkeley: ProQuest Dissertations & Theses, 2004.

Faris, A. T., R. B. Seed, R. E. Kayen, and J. Wu. "A Semi-Empirical Model for the Estimation of Maximum Horizontal Displacement Due to Liquefaction-Induced Lateral Spreading." *Procceedings of the 8th U.S. National Conference on Earthquake Engineering.* San Francisco: EERI, 2006.

GEER. "Geo-Engineering Reconnaissance of the February 27, 2010 Maule Chile Earthquake." *GEER Association.* May 25, 2010. http://www.geerassociation.org/GEER_Post %20EQ%20Reports/Maule_Chile_2010/Ver2_Maule_Chile_2010_index.html (accessed January 23, 2014).

Geologismiki. *Cliq User's Manual.* 2014. www.geologismiki.gr/Documents/Cliq/HTML /index.html (accessed October 27, 2014).

Geologismiki, Gregg Drilling Inc., and P. Robertson. (2006) Cliq (Version 1.7) [Software] Available from geologismiki.gr/Products/Cliq.htmal

Geovenor. *Proyecto 2 Ampliacion Muelle Coronel Informe Geotecnico para el Diseño de Pilotes Hincados.* Geotechnical Report, Santiago: Geovenor, 2003.

Geovenor. *Proyecto Construccion Puerto Coronel Compañia Peurto De Coronel S.A.* Geotechnical Report, Santiago: Geovenor, 1995.

Geovenor. *Puerto de Coronel Proyecto Muelle Sur Investigation Geotècnica.* Geotechnical Report, Santiago: Geovenor, 2006.

Goda, K., and G. M. Atkinson. "Variation of Source-to-Site Distance for Megathrust Subduction Earthquakes: Effects on Ground Motion Prediction Equations." *Earthquake Spectra*, 2014: 845-866.

Hayes, G. "Subduction Zone Geometry Analysis." *USGS.* February 27, 2010. http://earthquake.usgs.gov/earthquakes/eqarchives/subduction_zone/us2010tfan/ (accessed January 24, 2014).

Idaho Geological Survey. *Landslides.* n.d. ww.idahogeology.org/DrawOnePage.asp?PageID=83 (accessed November 11, 2014).

Idriss, I. M., and R. W. Boulanger. "Semi-Empirical Procedures for Evaluating Liquefaction Potential During Earthquakes." *Proceedings of the 11th ICSDEE and 3rd ICEGE.* Berkley, 2004. 32-56.

Lay, T., C. J. Ammon, H. Kanamori, K. D. Koper, O. Sufri, and A. R. Hutko. ""Teleseismic inversion for rupture process of the 27 Februaty 2010 Chile (Mw 8.8) earthquake." *Geophysical Research Lettters*, 2010: L13301.

Ramsey, F. L., and D. W. Schafer. *The Statistical Sleuth.* Pacific Grove: Duxbury, 2002.

Rauch, A. F., and J. R. Martin II. "EPOLLS Model for Predicting Average Displacements on Lateral Spreads." *Journal of Geotechnical and Geoenvironmental Engineering*, 2000: 360-371.

Ruiz, S., et al. "Short-Period Rupture Process of the 2010 Mw 8.8 Maule Earthquake in Chile." *Earthquake Spectra*, 2012: S1-S18.

Seed, R. B., and L. F. Harder. "SPT-Based Analysis of Cyclic Pore Pressure Generation and Undrained Residual Strength." n.d.: 351-376.

Seed, R. B., et al. *Recent Advances in Soil Liquefaction Engineering: A Unified and Consistent Framework.* ASCE Seminar Report, Berkley: Earthquake Engineering Research Center, 2003.

Sladen, A. *Preliminary Result 02/27/2010 (Mw 8.8), Chile.* n.d. www.tectonics. caltech.edu/slip_history/2010_chile/index.html (accessed October 14, 2014).

U.S. Geological Survey. *Magnitude 8.8 - Offshore Bio-Bio, Chile.* May 8, 2013. http://earthquake.usgs.gov/earthquakes/eqinthenews/2010/us2010tfan/us2010tfan.php (accessed January 30, 2014).

—. "The Great Alaska Earthquake and Tsunami of March 27, 1964." *USGS.* May 28, 2014. earthquake.usgs.gov/earthquakes/events/alaska1964 (accessed December 6, 2014).

—. *USGS Centriod Moment Solution.* March 2, 2010. http://earthquake.usgs.gov/earthquakes /eqinthenews/2010/us2010tfan/neic_tfan_cmt.php (accessed October 14, 2014).

—. *USGS Earthquake Map.* October 13, 2014. earthquake.usgs.gov/earthquakes/map/ (accessed October 13, 2014).

Youd, T. L., interview by K. M. Rollins. (August 21, 2014).

Youd, T. L., C. M. Hansen, and S. F. Bartlett. "Revised Multilinear Regression Equations for Prediction of Lateral Spread Displacement." *Journal of Geotechnical and Geoenvironmental Engineering*, 2002: 1007-1017.

Youd, T. L., et al. ""Liquefaction Resistance of Soils: Summary Report from the 1996 NCEER and 1998 NCEER/NSF Workshops on Evaluation of Liquefaction Resistance of Soils." *Journal of Geotechnical and Geoenvironmental Engineering*, 2001: 817-833.

Youngs, R. R., S. -J. Chiou, W. J. Silva, and J. R. Humphrey. "Strong Ground Motion Attenuation Relationships for Subduction Zone Earthquakes." *Seismological Research Letters*, 1997: 59-73.

Zhang, G., P.K. Robertson, and R.W.I. Brachman. "Estimating Liquefaction-Induced Lateral Displacements Using the Standard Penetration Test or Cone Penetration Test." *Journal of Geotechnical and Geoenvironmental Engineering*, 2004: 861-871.

Zhang, J., Y. Chagwei, J. X. Zhao, and G. H. McVerry. "Empirical Models for Predicting Lateral Spreading Considering The Effect of Regional Seismicity." *Earthquake Engineering and Engineering Vibration*, 2012: 121-131.

Zhao, J. X., et al. "Attenuation of Strong Ground Motion in Japan Using SIte Classification Based on Predominant Period." *Bulletin of the Seismological Society of America*, 2006: 898-913.

APPENDIX

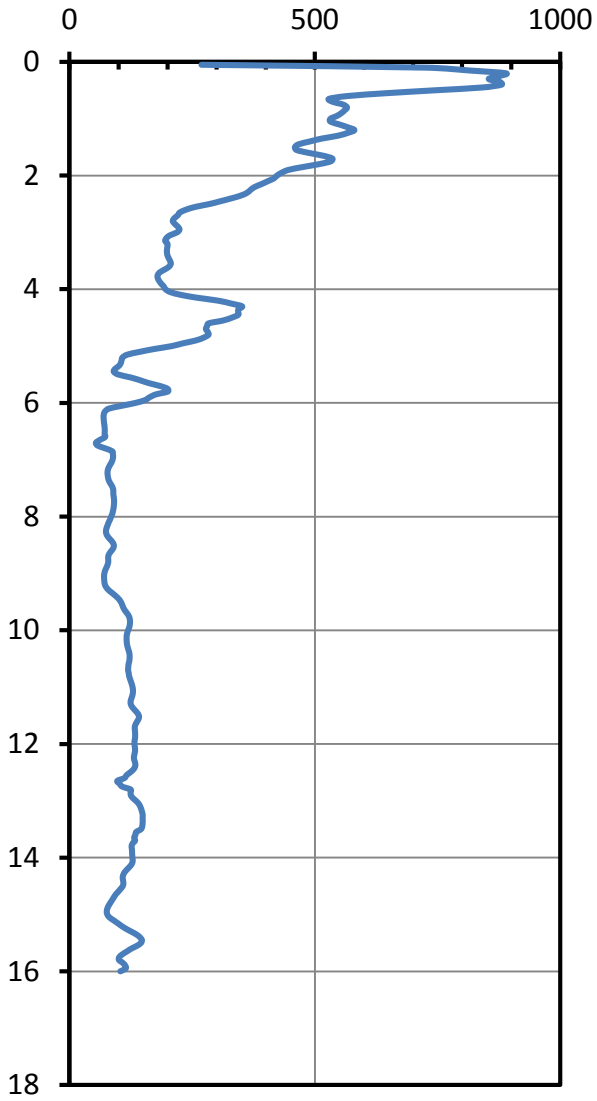

Figure A - 1: Normalized cone resistance, Qtn, for BYU CPT 1

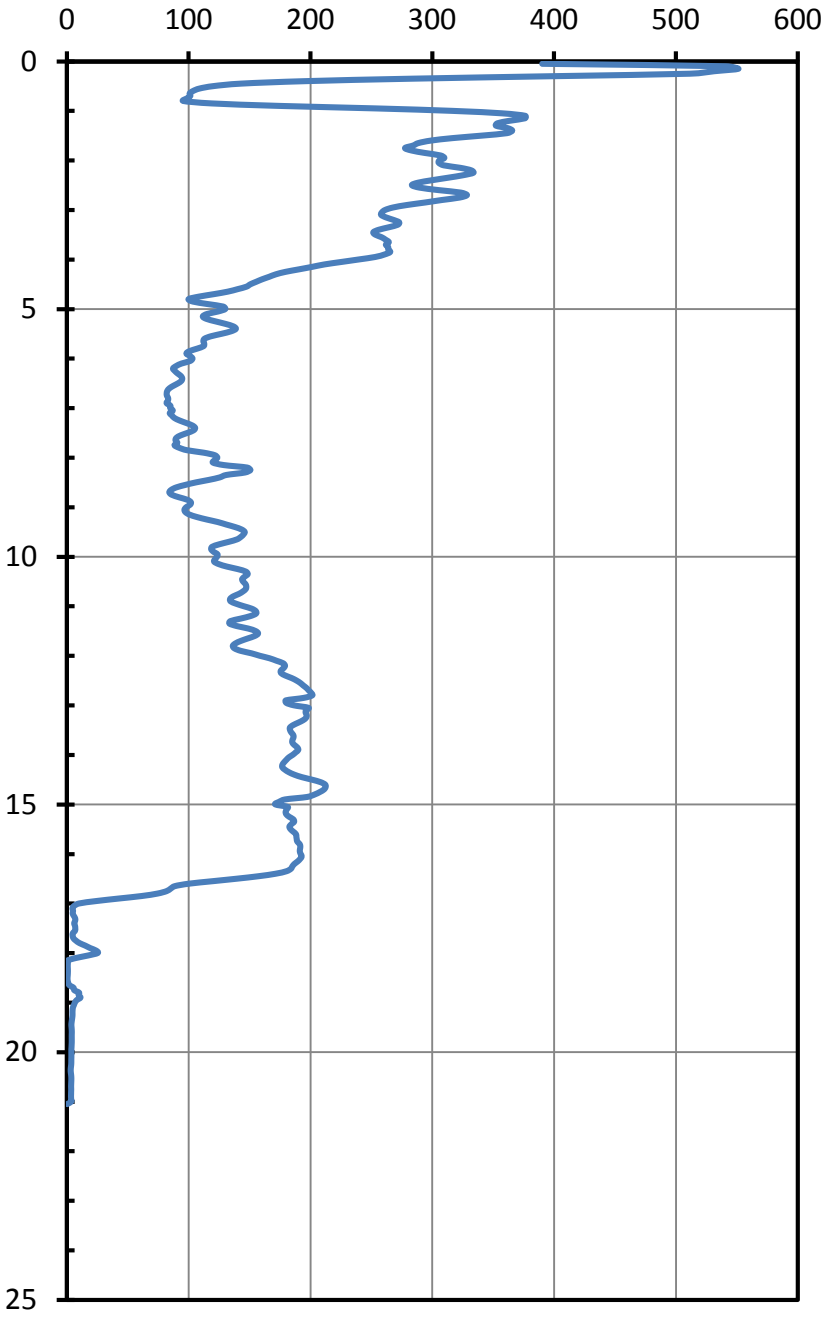

Figure A - 2: Normalized Cone resistance, Qtn, for CPT 2

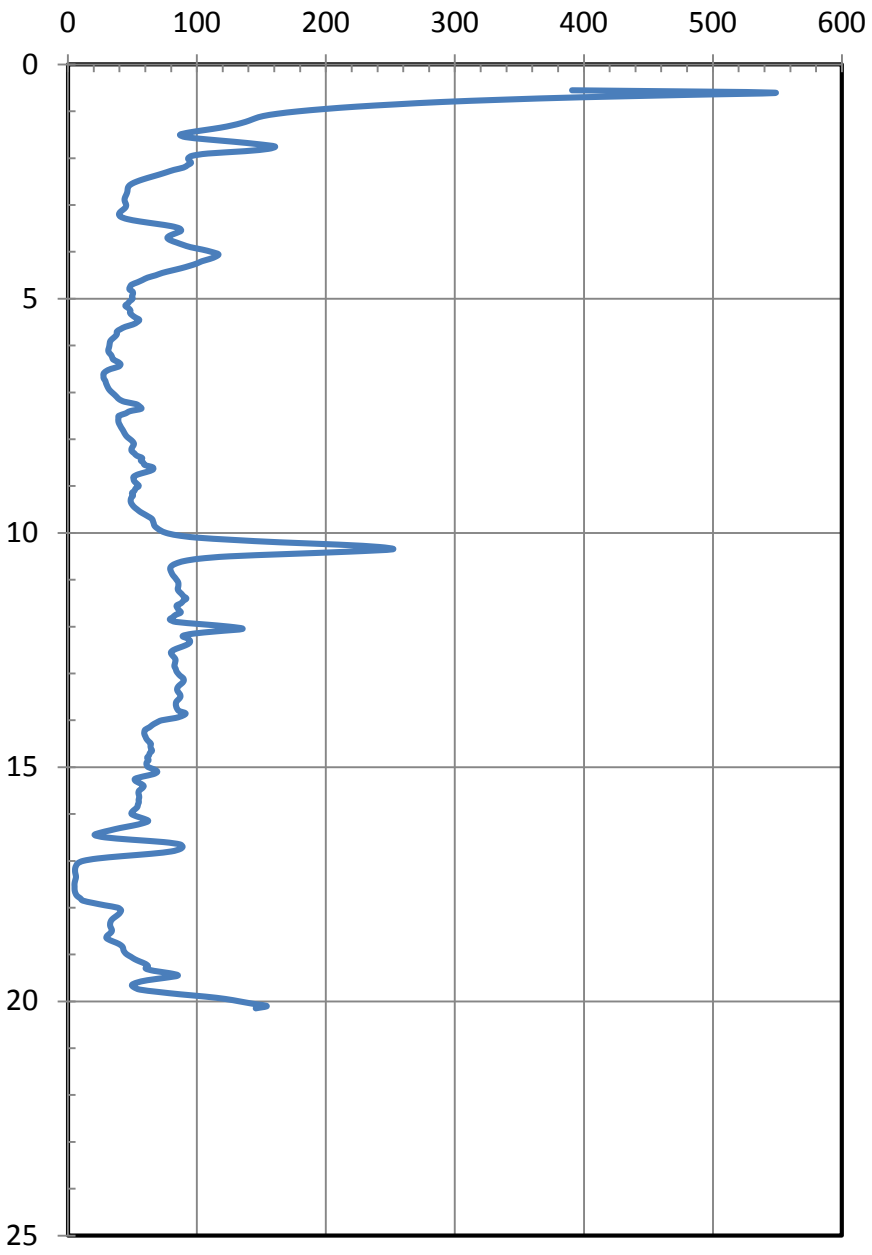

Figure A - 3: Normal cone resistance, Qtn, for BYU CPT 3

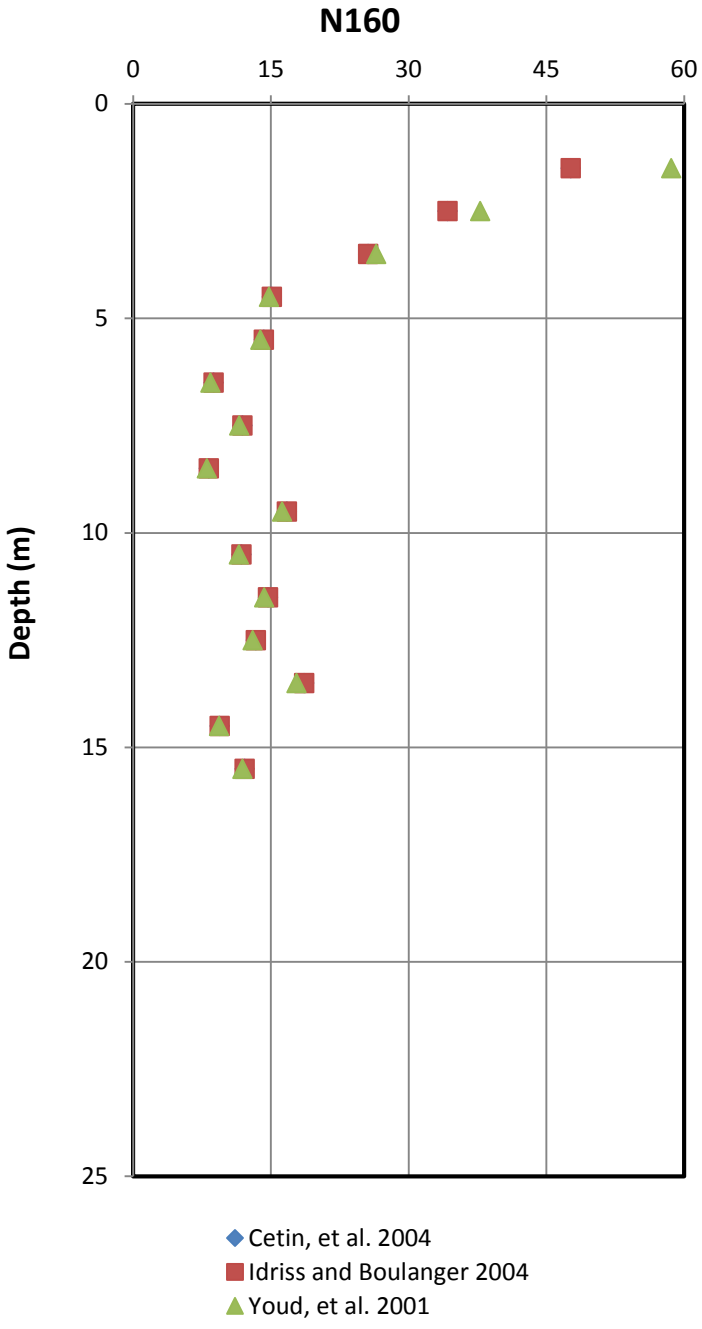

Figure A - 4: $N1_{60}$ values for BYU SPT 1

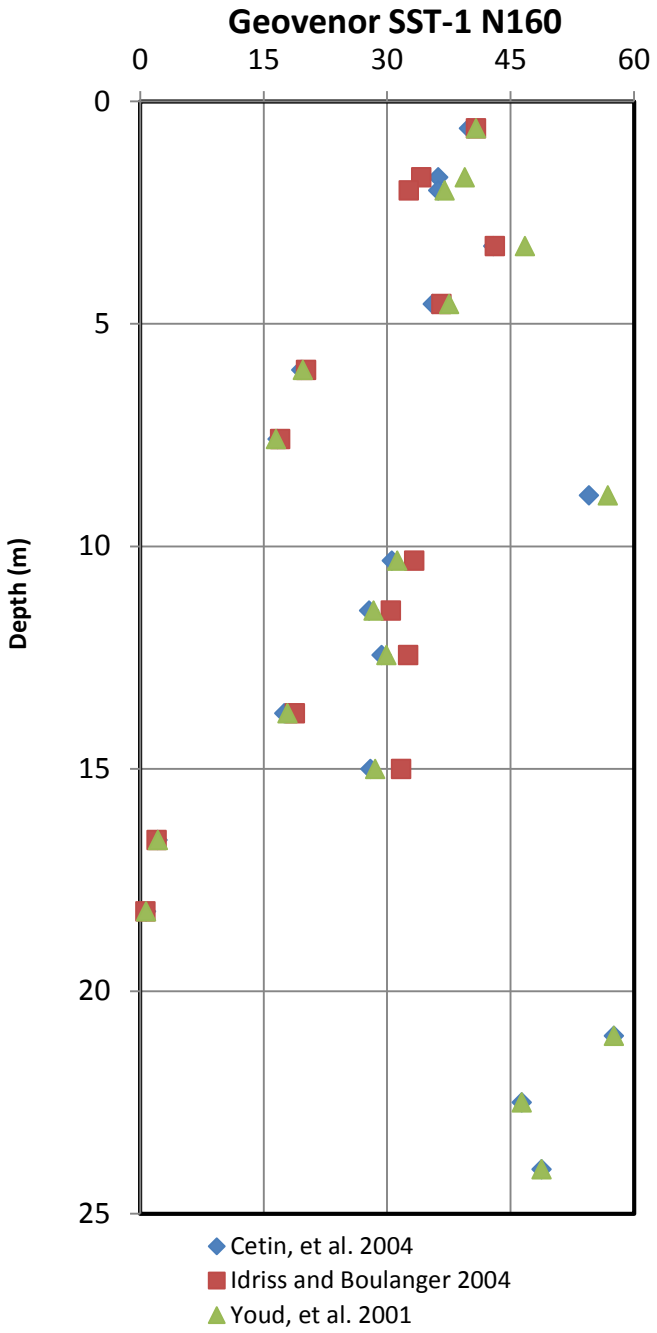

Figure A - 5: Geovenor SST-1 SPT test at head of South Pier

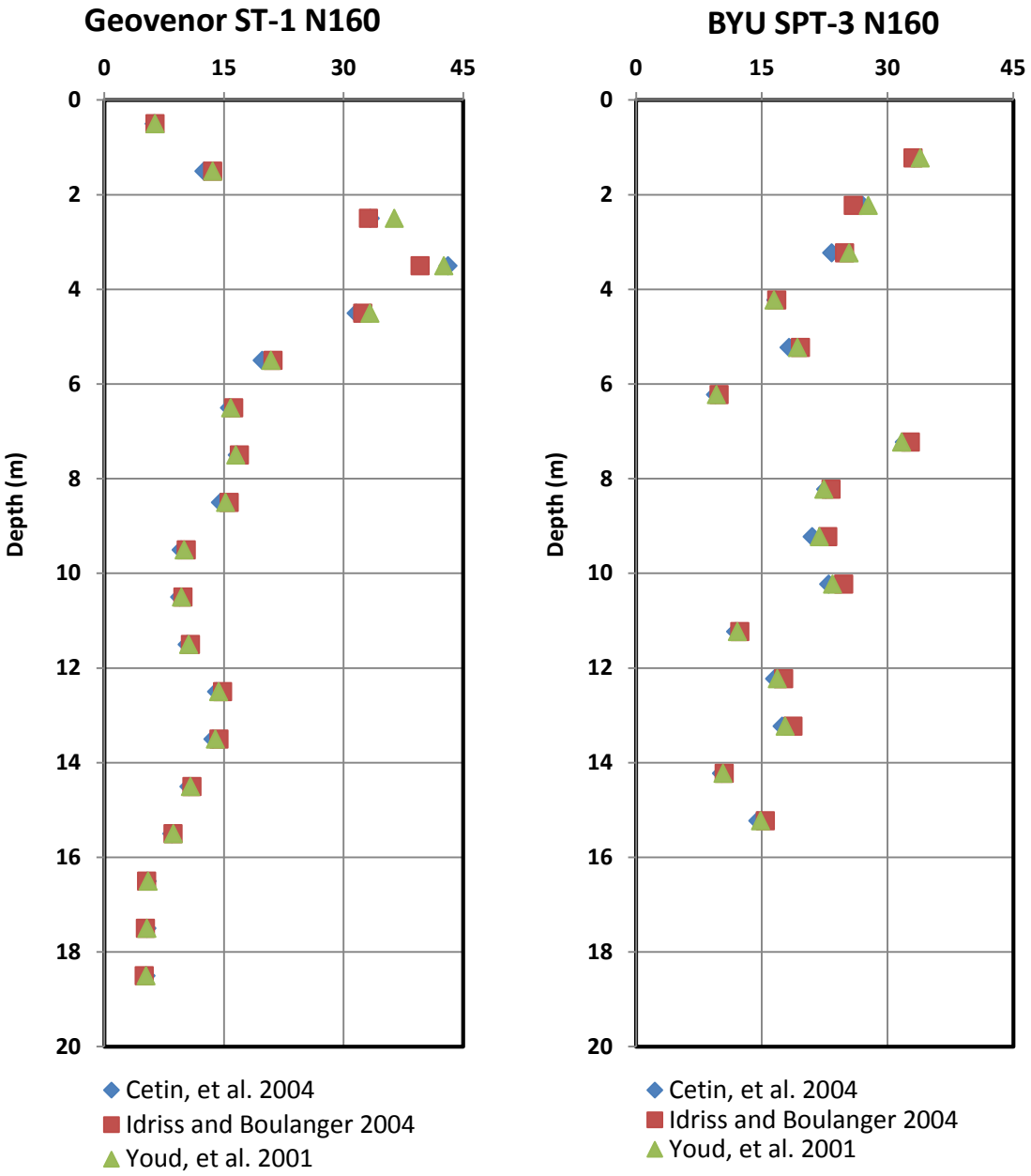

Figure A - 6: SPT tests at head of North Pier

PROYECTO MUELLE SUR

Doc.: 1366-17/05-RG-0

Reconocimiento Geotécnico

RESULTADOS EXPLORACION DEL SUBSUELO SONDAJE SST-1

COORDENADAS UTM.: NORTE : 5 . 899 . 950 , 7 ESTE : 664 . 725 , 4 COTAS (m) Inicio: 3,47 m

FECHA EJECUCION: INICIO : 17 / 04 / 06 TERMINO : 24 / 04 / 06 Término: -46,40 m

PROFUNDIDAD DE	PROFUNDIDAD A	DESCRIPCION VISUAL DEL SUBSUELO	MUESTRA Nº	MUESTRA TIPO	ENSAYO DE PENETRACION ESTANDAR N1	N2	N3	N	L (cm)	PENETRACION DE	PENETRACION A
0,00	0,24	Asfalto más base estabilizada	1						6	0,00	0,24
0,24	1,20	Grava fina, con arena de grano medio. Cantos angulares. Limpia.	2*	CN1	14	18	14	32	35	0,24	0,70
1,20	4,00	Arena fina a media, limpia, mal graduada, con cantos angulares. Compacidad densa. Color gris oscuro.	3	CN2	8	13	16	29	27	1,55	1,85
			4*	CN1	10	15	14	29	34	1,84	2,29
			5*	CN1	6	17	27	44	35	3,05	3,55
4,00	9,85	Arenas medias y finas, muy limosas, con algo de grava angular. Compacidad media. Color gris. Lente de arena fina algo limosa entre 6.0 m y 6.5 m. Vetas de carboncillo a 8.4 m.	6*	CN1	11	16	19	35	32	4,55	5,00
			7*	CN1	10	10	10	20	35	6,03	6,48
			8*	CN1	5	8	10	18	32	7,59	8,04
			9*	CN1	16	33	29	62	12	8,85	9,30
9,85	14,80	Arena media, con algo de arena gruesa y fina, presenta conchilla, bajo contenido de carboncillo molido y granos de cuarzo. Compacidad densa. Color gris oscuro.	10*	CN1	13	16	20	36	32	10,32	10,77
			S/M*	CN1	16	15	19	34	0	11,44	12,44
			11	CN1	15	17	20	37	26	12,44	12,89
			12*	CN1	2	8	15	23	40	13,49	13,94

SIMBOLOGIA DE MUESTRA	MUESTREADOR TIPO	ENSAYO SPT	OTROS ENSAYOS
S/M : Sin Muestra recuperada	CN1 : Cuchara Normal 2.0"	N1 : Número de golpes para penetrar los primeros 15 cm	CG : Ensayo de Cono Geovenor
L : Longitud de la muestra.	CN2 : Cuchara Normal 2.5"	N2 : Número de golpes para penetrar los segundos 15 cm	* : Ensayo Medición de Torque
R : Recuperación en %	SH1 : Tubo Shelby 2.0"	N3 : Número de golpes para penetrar los últimos 15 cm	** : Martillo a Cable
	SH2 : Tubo Shelby 2.5"	N : N2 + N3	(Masa 72,6kg/Altura caida 75cm)

HOJA 1 DE 3

Anexo A

TABLA: A-9

Figure A - 7: SPT Test at head of South Pier Page 1 (Geovenor 2006)

RESULTADOS EXPLORACION DEL SUBSUELO SONDAJE SST-1

COORDENADAS UTM.: NORTE : 5 . 899 . 950 , 7 ESTE : 664 . 725 , 4 COTAS (m) Inicio: 3,47 m
FECHA EJECUCION: INICIO : 17 / 04 / 06 TERMINO : 24 / 04 / 06 Término: -46,40 m

PROFUNDIDAD DE	PROFUNDIDAD A	DESCRIPCION VISUAL DEL SUBSUELO	MUESTRA Nº	MUESTRA TIPO	ENSAYO DE PENETRACION ESTANDAR N1	N2	N3	N	L (cm)	PENETRACION DE	PENETRACION A
30,80	35,20	Limo muy arenoso. Plasticidad media a alta. Consistencia rígida. Presenta restos de conchuelas. Color gris oscuro	26*	CN1	2	5	5	10	45	33,23	33,68
			27*	CN1	0	6	7	13	45	34,46	34,91
35,20	39,85	Arena fina, limosa. Plasticidad nula. Compacidad densa a muy densa. Lente de arena fina muy limosa no plástica entre 38,90 m y 39,13 m. Color gris oscuro.	28	SH2					25	35,80	36,83
			CG2		18				0	36,19	36,39
			29*	CN1	8	16	22	38	20	37,49	37,94
			30*	CN1	29	52/13cm		100	28	38,93	39,21
			CG3		2	4	9				
39,85	49,87	Limo arenoso. Compresibilidad y plasticidad alta. Consistencia media a rígida hasta 46.5 m. Entre 46,5 m y 47,5 m existe un sub estrato de arena fina limosa de compacidad suelta. Bajo 47,5 m hasta el fin de la perforación el limo cambia a una consistencia blanda a muy blanda. Color gris.	31*	CN1	9	7	12	19	45	40,19	40,64
			32*	CN1	0	0	0	0	28	41,67	42,18
			33	SH1					52	42,18	42,70
			34*	CN1	7	8	8	16	45	44,02	44,47
			35	SH2					50	45,85	46,35
			36*	CN1	0	0	0	0	50	46,53	47,03
			37*	CN1	0	0	0	0	35	49,33	49,87

SIMBOLOGIA DE MUESTRA	MUESTREADOR TIPO	ENSAYO SPT	OTROS ENSAYOS
S/M : Sin Muestra recuperada	CN1 : Cuchara Normal 2.0"	N1 : Número de golpes para penetrar los primeros 15 cm	CG : Ensayo de Cono Geovenor
L : Longitud de la muestra,	CN2 : Cuchara Normal 2.5"	N2 : Número de golpes para penetrar los segundos 15 cm	* : Ensayo Medición de Torque
R : Recuperación en %	SH1 : Tubo Shelby 2.0"	N3 : Número de golpes para penetrar los últimos 15 cm	** : Martillo a Cable
	SH2 : Tubo Shelby 2.5"	N : N2 + N3	(Masa 72,6kg/Altura caida 75cm)

HOJA 3 DE 3

Anexo A

TABLA: A-9

Figure A - 8: SPT Test at head of South Pier Page 2 (Geovenor 2006)

PROYECTO MUELLE SUR

Doc.: 1366-17/05-RG-0

Reconocimiento Geotécnico

RESULTADOS EXPLORACION DEL SUBSUELO SONDAJE SST-1

COORDENADAS UTM.: NORTE : 5.899.950,7 ESTE : 664.725,4 COTAS (m) Inicio: 3,47 m

FECHA EJECUCION: INICIO : 17/04/06 TERMINO : 24/04/06 Término: -46,40 m

PROFUNDIDAD DE	PROFUNDIDAD A	DESCRIPCION VISUAL DEL SUBSUELO	MUESTRA Nº	MUESTRA TIPO	ENSAYO DE PENETRACION ESTANDAR N1	N2	N3	N	L (cm)	PENETRACION DE	PENETRACION A
30,80	35,20	Limo muy arenoso. Plasticidad media a alta. Consistencia rígida. Presenta restos de conchuelas. Color gris oscuro	26*	CN1	2	5	5	10	45	33,23	33,68
			27*	CN1	0	6	7	13	45	34,46	34,91
35,20	39,85	Arena fina, limosa. Plasticidad nula. Compacidad densa a muy densa. Lente de arena fina muy limosa no plástica entre 38,90 m y 39,13 m. Color gris oscuro.	28	SH2					25	35,80	36,83
			CG2		18				0	36,19	36,39
			29*	CN1	8	16	22	38	20	37,49	37,94
			30*	CN1	29	52/13cm		100	28	38,93	39,21
			CG3		2	4	9				
39,85	49,87	Limo arenoso. Compresibilidad y plasticidad alta. Consistencia media a rígida hasta 46,5 m. Entre 46,5 m y 47,5 m existe un sub estrato de arena fina limosa de compacidad suelta. Bajo 47,5 m hasta el fin de la perforación el limo cambia a una consistencia blanda a muy blanda. Color gris.	31*	CN1	9	7	12	19	45	40,19	40,64
			32*	CN1	0	0	0	0	28	41,67	42,18
			33	SH1					52	42,18	42,70
			34*	CN1	7	8	8	16	45	44,02	44,47
			35	SH2					50	45,85	46,35
			36*	CN1	0	0	0	0	50	46,53	47,03
			37*	CN1	0	0	0	0	35	49,33	49,87

SIMBOLOGIA DE MUESTRA	MUESTREADOR TIPO	ENSAYO SPT	OTROS ENSAYOS
S/M : Sin Muestra recuperada	CN1 : Cuchara Normal 2.0"	N1 : Número de golpes para penetrar los primeros 15 cm	CG : Ensayo de Cono Geovenor
L : Longitud de la muestra.	CN2 : Cuchara Normal 2.5"	N2 : Número de golpes para penetrar los segundos 15 cm	* : Ensayo Medición de Torque
R : Recuperación en %	SH1 : Tubo Shelby 2.0"	N3 : Número de golpes para penetrar los últimos 15 cm	** : Martillo a Cable
	SH2 : Tubo Shelby 2.5"	N : N2 + N3	(Masa 72,6kg/Altura caida 75cm)

HOJA 3 DE 3

Anexo A

TABLA: A-9

Figure A - 9: SST-2 SPT Test at head of South Pier Page 3 (Geovenor 2006)

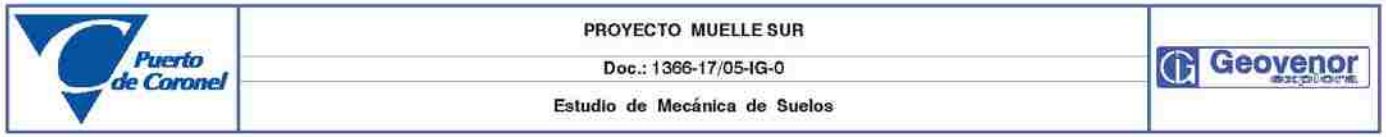

RESULTADOS ENSAYOS DE CLASIFICACION Y PROPIEDADES INDICE SONDAJE SST-1

MUESTRA N°		2	3	4	5	6	7	8	9	10	11	12	13	
Profundidad (m)	de	0,24	1,55	1,84	3,05	4,55	6,03	7,59	8,85	10,32	12,44	13,49	14,84	
	a	0,70	1,85	2,29	3,55	5,00	6,48	8,04	9,30	10,77	12,89	13,94	15,34	
Criba	3" (75,2mm)													
	1 1 / 2" (38,1mm)	100												
	3 / 4" (19,1 mm)	71				100		100						
	3 / 8" (9,52mm)	44				97		97	100	100	100	100		
Malla ASTM	4 (4,75mm)	40				87	100	82	70	99	99	99		
	10 (2,00mm)	39	100	100	100	83	99	80	58	94	98	98	100	
	20 (0,85mm)	37	99	97	88	72	97	79	56	77	81	82	89	
	40 (0,425mm)	17	66	48	30	43	85	78	55	34	24	15	19	
	60 (0,250mm)	6	17	15	10	34	67	72	43	17	8	4	6	
	100 (0,150mm)	3	3	6	6	30	26	61	39	7	6	3	4	
	200 (0,075mm)	2	2	4	3	29	6	43	37	3	4	2	3	
Límite Líquido														
Límite Plástico														
Indice Plasticidad		NP	NP	NP	NP	NP	NP	NP	NP	NP	NP	NP	NP	
Humedad	(%)	4,6	11,1	15,8	20,1	18,6	25,7	20,9	12,7	27,4	24,1	26,3	23,5	
Peso específico					2,62	2,76		2,61			2,72	2,7	2,7	
Clasificación USCS		**GP**	**SP**	**SP**	**SP**	**SM**	**SP-SM**	**SM**	**SM**	**SP**	**SP**	**SP**	**SP**	
Peso Unitario														
Peso Unitario Natural	(T/m³)													
Peso Unitario Seco	(T/m³)													

HOJA 1 DE 2

Anexo A

TABLA: A-20

Figure A - 10: Lab data from soil samples for SPT test at the head of the South Pier Page 1 (Geovenor 2006)

RESULTADOS ENSAYOS DE CLASIFICACION Y PROPIEDADES INDICE SONDAJE SST-1

MUESTRA N°		14A	14 B	15	16	17	18	19	20	21	22	23	24	25
Profundidad (m)	de	16,40	16,55	16,90	17,91	19,36	20,80	22,30	23,81	25,27	26,81	28,27	29,78	31,25
	a	16,55	16,85	17,45	18,36	19,93	21,25	22,75	24,26	25,62	27,26	28,72	30,42	31,88
Criba	3" (75,2mm)													
	1 1 / 2" (38,1mm)													
	3 / 4" (19,1 mm)													
	3 / 8" (9,52mm)	100				100	100							
Malla ASTM	4 (4,75mm)	99		100	100	96	99		100	100	100			
	10 (2,00mm)	94	100	99	99	94	98	100	99	99	99			100
	20 (0,85mm)	80	94	98	96	92	84	99	96	94	98	100	100	99
	40 (0,425mm)	62	85	96	94	84	50	89	72	67	93	98	99	98
	60 (0,250mm)	43	76	93	89	71	28	46	30	35	70	87	93	96
	100 (0,150mm)	30	62	89	76	59	22	19	10	15	25	50	55	94
	200 (0,075mm)	16	30	45	52	42	5	10	6	9	10	32	45	92
Límite Líquido		25	29	31	38	28	NP	NP	NP	NP	NP	33	36	62
Límite Plástico		24	28	27	25	26						30	33	32
Indice Plasticidad		1	1	4	13	2						3	3	30
Humedad	(%)	34,1	38,7	33,4	44,2	42,1	28,1	2,7	32,0	30,3	28,8	46,1	50,2	66,0
Peso específico								2,67			2,58	2,57		
Clasificación USCS		**SM**	**SM**	**SM**	**ML**	**SM**	**SP-SM**	**SP-SM**	**SP-SM**	**SP-SM**	**SP-SM**	**SM**	**SM**	**MH**
Peso Unitario														
Peso Unitario Natural	(T/m³)			1,84		1,75								1,58
Peso Unitario Seco	(T/m³)			1,38		1,23								0,95

Figure A - 11: Lab data from soil samples for SPT test at the head of the South Pier Page 1 (Geovenor 2006)

RESULTADOS ENSAYOS DE CLASIFICACION Y PROPIEDADES INDICE SONDAJE SST-1

MUESTRA N°		26	27	28	29	30	30A	31	32	33	34	35	36	37
Profundidad (m)	de	33,23	34,46	35,80	37,49	38,93	39,13	40,19	41,67	42,18	44,02	45,85	46,53	49,33
	a	33,68	34,91	36,83	37,94	39,13	39,21	40,64	42,18	42,70	44,47	46,35	47,03	48,87
Criba	3" (75,2mm)													
	1 1 / 2" (38,1mm)													
	3 / 4" (19,1 mm)													
	3 / 8" (9,52mm)					100						100		
Malla ASTM	4 (4,75mm)			100		97						99	100	
	10 (2,00mm)			93		94	100	100	100		100	98	99	
	20 (0,85mm)	100	100	91	100	91	99	99	99	100	99	97	96	100
	40 (0,425mm)	93	85	73	98	89	96	90	98	99	97	96	84	99
	60 (0,250mm)	82	72	48	81	71	71	86	95	96	92	94	81	96
	100 (0,150mm)	71	57	30	27	54	28	64	92	93	84	89	34	90
	200 (0,075mm)	68	51	20	18	44	15	54	83	84	69	81	20	78
Límite Líquido		63	48	NP	NP	NP	NP	52	79	79	72	76	63	49
Límite Plástico		33	28					30	42	37	36	35	42	33
Indice Plasticidad		30	20					22	37	42	36	41	21	16
Humedad	(%)	54,0	45,1	24,9	21,6	31,6	25,9	73,0	80,8	91,1	80,2	70,1	69,2	49,7
Peso específico												2,56	2,39	
Clasificación USCS		**MH**	**ML**	**SM**	**SM**	**SM**	**SM**	**MH**	**MH**	**MH**	**MH**	**MH**	**SM**	**ML**
Peso Unitario														
Peso Unitario Natural	(T/m³)											1,49		
Peso Unitario Seco	(T/m³)											0,87		

HOJA 3 DE 3

Anexo A

TABLA: A-20

Figure A - 12: Lab data from soil samples for SPT test at the head of the South Pier Page 1 (Geovenor 2006)